Spring 5-20-2022

Experimental and Numerical Investigation of 3D-Printed Viscoelastic Dampers

Mohammed Jaradat

Mohammed Jaradat

Candidate

Civil, Construction and Environmental Engineering

Department

This dissertation is approved, and it is acceptable in quality and form for publication:

Approved by the Dissertation Committee:

Mahmoud Reda Taha , Chairperson

Yu-Lin Shen

Fernando Moreu

Eslam Soliman

Experimental and Numerical Investigation of 3D-Printed Viscoelastic Dampers

by

Mohammed Jaradat

B.S. Civil Engineering, Jordan University of Science and Technology, Jordan, 2011.

MSc. Engineering Science, University of Mississippi, USA, 2014.

Dissertation

Submitted in Partial Fulfillment of the

Requirements for the Degree of

Doctor of Philosophy

Engineering

The University of New Mexico

Albuquerque, New Mexico

May 2022

Dedication

To my loving parents Abdul-Rahman and Rana, sister Buthayna, and brothers Ahmed and Ibrahim.

Acknowledgement

(الْحَمْدُ لِلّهِ الَّذِي هَدَانَا لِهَـذَا وَمَا كُنَّا لِنَهْتَدِيَ لَوْلا أَنْ هَدَانَا اللّه)

I would like to thank my advisor and committee chair, Dr. Mahmoud Reda Taha, for his mentoring, encouragement, and guidance throughout this research. I'm also grateful to committee member Dr. Eslam Soliman for his advice and encouragement throughout the development of this research and the expertise shared with me on this subject. I would also like to thank Dr. Yu-Lin Shen and Dr. Fernando Moreu for serving on my committee.

The generous support of the Dana C. Wood Endowment at the University of New Mexico is greatly acknowledged.

I would like to thank my colleagues Daniel Heras Murcia, Shreya Vemuganti, and Serafin García Fernández for their help and support.

3D Printed Mechanically Interlocked Viscoelastic Dampers for Energy Dissipation

BY

Mohammed Jaradat

B.S. Civil Engineering, Jordan University of Science and Technology, Jordan, 2011.

MSc. Engineering Science, University of Mississippi, USA, 2014.

Ph.D. Engineering, University of New Mexico, USA, 2022.

ABSTRACT

Elastomeric materials are extensively used in energy dissipation applications to mitigate large lateral displacements and attenuate vibrations. One way of exploiting the capabilities of elastomeric materials is using shear-damping mechanisms such as viscoelastic damping devices (VEDs).

In this research the freedom of design offered by additive manufacturing technology is utilized to produce 3D printed elastomeric parts that act as the viscoelastic layer in an energy damping device. A mechanically interlocked viscoelastic damper (MIVED) with a jigsaw-like interlocking mechanism was designed and manufactured. MIVED is composed of a rigid and soft phase. It operates in two modes, modes I and II, that depend on the stiffnesses of the rigid and soft phases as well as the stiffness of the connection used to fix it to the testing machine or structural element. The modes are illustrated through changing the rigid and soft phase materials. For that purpose, two devices were fabricated MIVED-1 and MIVED-2 to observe modes I and II, respectively. The rigid phase of MIVED-1 was made of steel, while the soft phase is 3D printed using

thermoplastic polyurethane (TPU). MIVED-2 had a rigid phase made from 3D printed fiber reinforced nylon, and 3D printed TPU injected with silicone rubber for the soft phase.

The devices were cyclically tested under different amplitudes and frequencies, and the response was examined. 3D printed TPU was mechanically characterized using uniaxial cyclic tension tests under different rates and different printing processing parameters. Stress relaxation tests were also conducted to obtain the viscoelastic behavior of the TPU material. Material characterization of TPU was used to develop a finite element (FE) model that is used to simulate the mechanically interlocked damper. The FE model was validated with the experimental observations of TPU specimens and MIVED-1 and was then used to examine the significance of damper geometry and material parameters on the efficiency of energy dissipation using the 3D printed interlocking mechanism.

Finally, the performance of the device was evaluated as a part of a structural frame system. A simplified analytical model of the device was developed and incorporated within the frame system. The frame was then subjected to El Centro ground acceleration and the response of the structural system was studied.

Table of Contents

LIST OF FIGURES

LIST OF TABLES

Chapter 1: **Introduction**

1.1 Background and motivation

The implications of structural vibrations and the need to sustain higher dynamic loads has led to the development of various structural control methods. These methods are mainly used to suppress or mitigate vibrations. The aftermath of vibrations can be sometimes devastating such as earthquakes where human lives can be lost, and vital infrastructure can be left damaged or not functional. Vibrations can also cause great discomfort to humans occupying vehicles such as cars, airplanes, or space shuttles, especially long exposure durations to vibrations close to the natural frequency of human organs [1]. Therefore, vehicle designers always consider the effects of noise, vibration, and harshness (NVH) that results from dynamic loading on the structure to provide safety and comfort to the passengers. On the other hand, some engineers and scientists are working on utilizing structural vibrations to produce energy. For instance, exploiting the wind loads sustained by tall buildings or traffic induced loads in bridges through using piezoelectric transducers to produce electricity [2]. Compliant mechanisms of flexible structures or functionally graded ones have also been used in piezoelectric energy harvesting [3,4]. Therefore, whether it is to suppress structural vibrations or harness the energy it produces, many industries are interested in the development of novel structural control methods.

Many damping methods for structural control were developed over the years that can be broadly categorized into two types: active and passive damping. Both types involve providing counter forces to the ones that are producing the vibrations. The difference

between them, however, is that active damping requires an external energy source to be activated whereas the passive damping does not. Viscoelastic dampers (VEDs) are a type of passive energy dissipating systems that provides good damping for a wide range of frequencies. They are used in buildings and bridges to attenuate vibrations resulting from earthquakes or winds [5,6]. They are also used in automotive and aerospace industries which usually requires mitigation of vibrations at much higher frequencies [7,8]. They operate using shear mechanisms that converts the mechanical energy generated by the device into thermal energy that gets dissipated into the environment, thereby alleviating vibrations. Elastomeric materials are typically used as the energy dissipating constrained layer in a VED. VEDs in their current form, however, do not offer any control over the behavior of the device such as a tailorable energy dissipation behavior. They are often manufactured using conventional casting methods. These methods impose part design restrictions that limit the design freedom and the ability to innovate.

The emergence of Additive Manufacturing (AM) has revolutionized the way we conceptualize structural components due to the design flexibility offered by this method. This has led researchers to experiment with complex geometries and designs aimed at increasing energy absorption of structural components under certain load conditions. For example, several classes of biomimetic or bio-inspired materials have been produced through 3D printing to enhance energy absorption [9,10]. Moreover, 3D printed bistable mechanisms have also been utilized in energy dissipation through exploiting both material and geometrical instabilities [11,12]. Lattice structures such as open cell structures have also shown that they can improve energy dissipation either through structural hierarchy

[13], self-interlocking techniques [14], or by adding a small fraction of a soft phase to a mostly rigid phase material [15].

This research takes advantage of the design flexibility offered by AM technology to develop viscoelastic energy damping devices. Hence, a mechanically interlocked viscoelastic damper was developed using Fused Deposition Modeling (FDM) technology. The device consists of a rigid phase and a soft elastomeric phase joined through a mechanical interlocking geometry. The salient feature of the device is its ability to dissipate energy through multiple modes of deformation of the soft phase and not only shear.

1.2 Research objective

This dissertation aims to investigate the use of 3D printing technology in structural control applications through:

a) Characterization of 3D printed TPU experimentally using uniaxial-cyclic loading and stress relaxation tests.
b) Study the effect of certain AM processing parameters on TPU specimens in addition to the effect of loading rate applied to the specimens.
c) Development and validation of a computational model using the results of the tested 3D printed TPU specimens.
d) Fabricate a mechanically interlocked viscoelastic damper (MIVED) with a jigsaw-like geometry acting as the interlocking joint.

e) Characterize the MIVED device both experimentally and numerically to understand its behavior and the effect of different geometrical and material parameters on its energy dissipation efficiency.

1.3 Dissertation outline

Chapter 1 provides an introduction to the dissertation as it highlights the motivation and objectives behind the work. A flow chart of the dissertation is also presented in this chapter.

Chapter 2 provides a background on energy dissipation systems and specifically VEDs and the techniques employed in modeling such devices. Additively manufactured viscoelastic elastomers are then discussed with an emphasis on Thermoplastic polyurethane (TPU) and Fused Deposition Modeling (FDM) technology. Lastly, the concept of mechanical interlocking and its application in the literature is reviewed.

In Chapter 3, the printed TPU via FDM technology was mechanically characterized using uniaxial cyclic tension tests. TPU was characterized using different infill patterns and under different loading rates. A viscoelastic damper made from 3D printed TPU and steel was assembled and tested cyclically under different amplitudes and frequencies. Material parameters were extracted from these tests and were used then to develop a Finite Element (FE) model of the tested specimens and the VED as well.

Chapter 4 introduces the mechanically interlocked viscoelastic damper (MIVED). The MIVED was tested experimentally at different frequencies and amplitudes to assess its performance. A FE model of MIVED was developed using the material parameters

that were extracted in Chapter 2. The model was validated with the experimental observations of the damper. The FE model was then used to conduct a parametric study to examine the effect of various geometrical and viscoelastic parameters on the damper response.

Chapter 5 studies the behavior of a single-story frame structure equipped with an analytical model of the MIVED. The response of the frame is studies and compared to the case with other dampers and without dampers.

Chapter 6 concludes the work, discusses limitations, and provides recommendations regarding future work on 3D printed mechanically interlocked viscoelastic dampers.

The flow chart in *Figure 1* shows the dissertation outline.

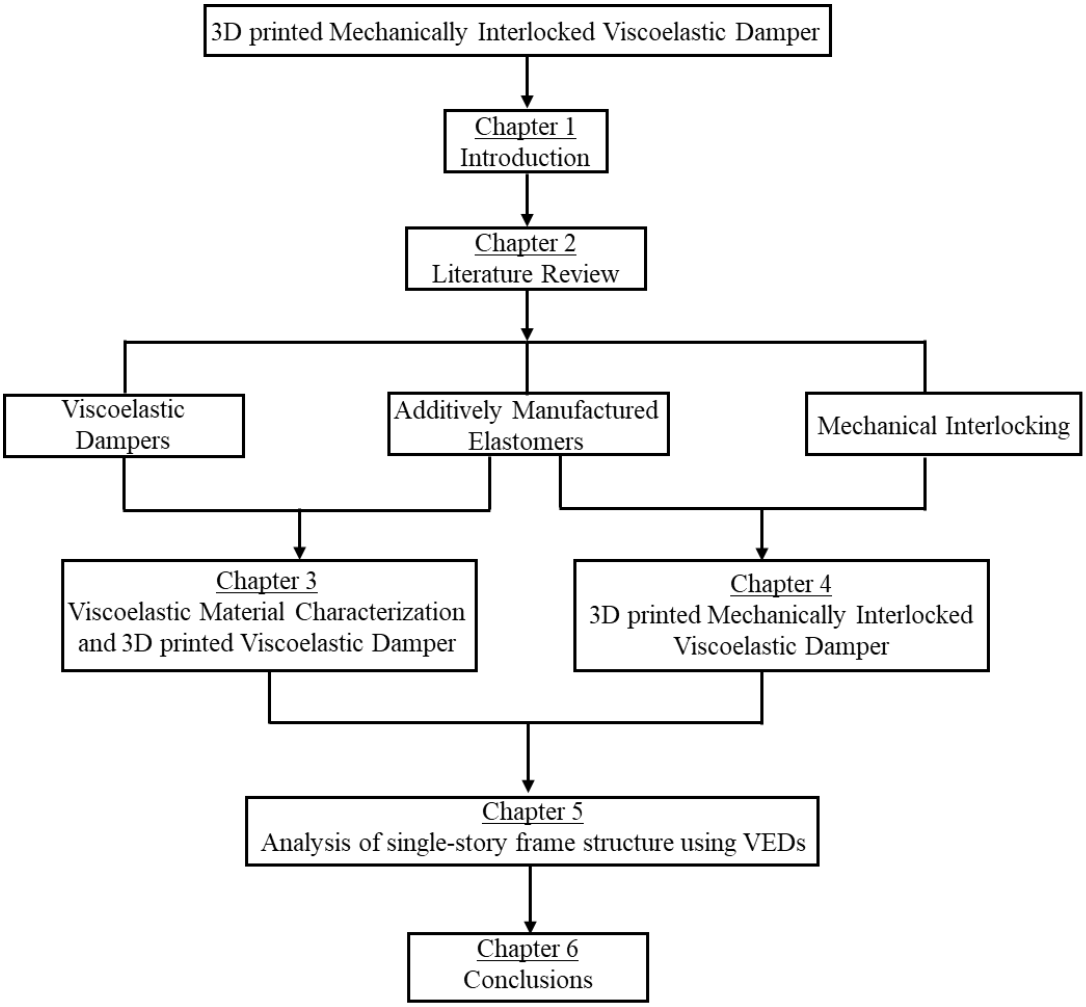

Figure 1 Dissertation flowchart

Chapter 2: **Literature review**

2.1 Viscoelastic Dampers

Structural control devices can be generally classified into three main types: active, semi-active and passive. Active and semi-active dampers require the use of a control algorithm to adjust the damping coefficient according to the displacement levels that the structure is experiencing. While passive dampers involve only the installation of the device within the structural system and requires no additional energy to operate.

Passive energy dissipation devices are often preferred due to their good damping, simplicity, ease of installation in construction, and low cost. The main objective of a passive damping device is to limit the deformations in the components of the frame system through reducing the inelastic energy dissipation demand on those components. They can be classified into two main types: displacement-dependent and rate-dependent devices. Metallic yield and friction devices are dependent only on the relative displacement across the device. Therefore, they represent displacement-dependent devices where the initial stiffness of the structure is increased until yielding and energy dissipation occurs at large deformations. This type of passive damping will increase the residual deformation in a structure due to residual plastic deformation in the metallic yielding device. Fluid viscous and viscoelastic dampers on the other hand represent rate-dependent devices as they mainly depend on the relative velocity across the device as means of energy dissipation. These devices reduce damage in a structural framing system because they generate minimal inelastic deformations and reduce the weight of the steel moment frame used in a structure [16].

VEDs are classified as rate-dependent, passive energy dissipation devices as shown in *Figure 2* that presents the main types and mechanisms of energy damping devices. Therefore, the following sections will focus on certain aspects of VEDs such as the design, materials used in VEDs, and how the performance of such devices is evaluated.

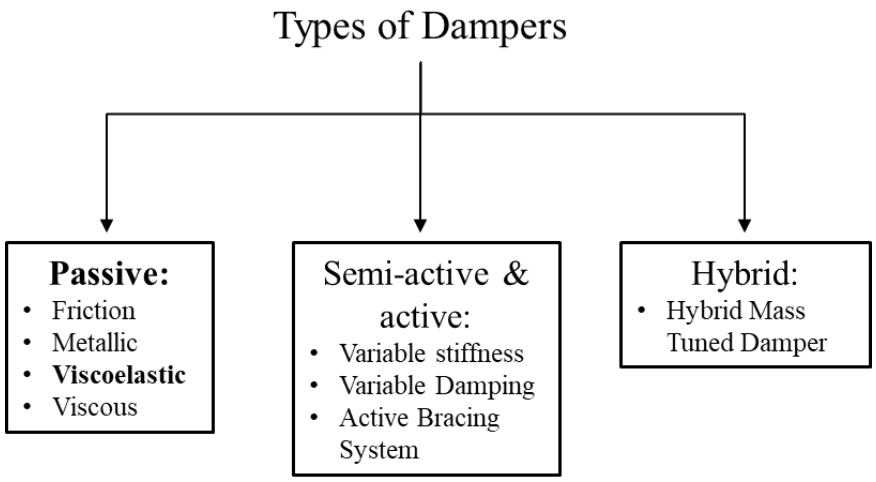

Figure 2 Types of dampers

2.1.1 Background and description of VEDs

Figure 3 shows a typical VED which consist of rigid steel plates with a viscoelastic material sandwiched in between the plates. They are typically fabricated using conventional casting methods such as injection molding, transfer molding, and compression molding. These devices are usually placed in locations where structural vibrations will cause shear deformations in the viscoelastic material. Energy is dissipated in such devices through the heat that is generated from the shear deformations that the viscoelastic material experiences.

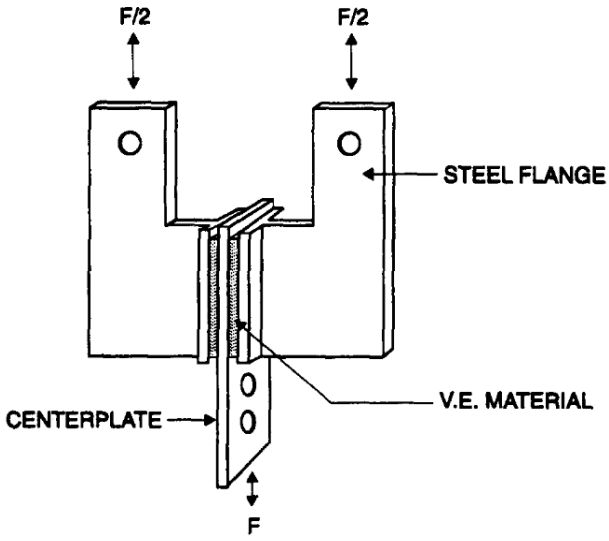

Figure 3 Typical VED

The primary advantage of using VEDs is that energy will be dissipated from the vibrating structure regardless of the level or magnitude of vibration as it operates under low as well as high frequencies. Moreover, VEDs will always provide a restoring force which is desirable in structural control. Nevertheless, their mechanical properties are solely dependent on the constrained viscoelastic material properties. Furthermore, the ability of a viscoelastic material to dissipate energy is influenced by different factors such as amplitude and frequency of vibrations in addition to the temperature of viscoelastic material [16].

VEDs are very common in high-rise buildings. They were first used to reduce wind-induced vibrations in the world trade center twin towers in 1969 [17]. They are now also used for seismic applications in buildings and bridges [5,18,19]. VEDs are used in automobiles and airplanes to support components against fatigue caused by cyclic loading [20]. For example, they are employed in aircraft wings vibrating at large amplitudes to avoid failure [21]. They are also used to improve the performance of some components such as engine mount systems by reducing vibrations [22].

Improvements on typical VEDs in the literature was found in the form of hybrid VEDs. This type of dampers combines viscoelastic damping with a different passive damping mechanism to either target an increase in damping capacity or to target a broader frequency range. Silwal et al. [23] developed a super viscoelastic damper through incorporating shape memory alloys to a typical VED design to increase damping as well as stiffness of the device. Chou et al. [24] combined a velocity-dependent viscoelastic damper and a displacement-dependent friction damper in a device to provide wind and seismic resistance. In a similar manner, Ibrahim et al. [25] developed a visco-plastic device for seismic protection of structures. The device amplifies strains at low level vibrations and dissipates energy through the viscoelastic material, whereas under high level vibrations dissipation is acquired through yielding of steel as well as the viscoelastic material. Mehrabi et al. [26] proposed a rotary rubber braced damper that dissipates energy through rotational shearing of a viscoelastic material.

2.1.2 Materials in VEDs

Elastomers are the most widely used materials as the constrained viscoelastic damping material in a VED. However, elastomers represent a wide range of materials that can have varying physical and chemical behaviors. Therefore, the characterization of the elastomeric constrained layer is of great importance to understand and predict the response of VEDs.

High damping rubber and high damped butyl elastomer are not affected much by loading frequency, but they are significantly affected by the shear strain amplitude. The effects are substantial at high strains where they display a pinching behavior in the response

curve [27,28]. On the other hand, polyurethane elastomers demonstrate obvious frequency dependence and no dependence on strain amplitude [29]. Xu et al. considered Nitrile Butadiene Rubber (NBR) and Silicone Rubber (SR) to be tested as damping devices [30]. NBR registered high energy dissipation and a dependency on frequency, while SR had a more stable response with slight dependency on strain amplitude.

2.1.3 Mathematical models

The general constitutive relation that governs the stress-strain relationship for polymeric materials can be expressed using what is known as the Boltzmann super-position principle as follows:

$$\tau(t) = \varepsilon_0 G(t) + \int_0^t G(t-\rho)\frac{d\varepsilon(\rho)}{d\rho}d\rho \qquad 1$$

Where: $\tau(t)$ is the shear stress, $\frac{d\varepsilon(\rho)}{d\rho}$ is the shear strain rate, $G(t-\rho)$ is the relaxation modulus, and t and ρ are time variables. ε_0 and $G(t)$ are the strain and instantaneous modulus. This constitutive relation shows how the stress at any given time is dependent on the entire strain history of the material, i.e., when $\rho < t$. If the initial strain is zero, then only the terms after the addition sign will be considered as part of the stress value. It is also valid for any linear viscoelastic material regardless of the model used to express the relaxation modulus. The most used models in the literature that employs Equation1 are rheological models and fractional-derivative models. Other models do not use the constitutive relation described above such as the bouc-wen model but it is not as widely used.

The simplest form of rheological models to describe viscoelastic behavior is a Maxwell or kelvin-voigt models as shown in *Figure 4*. The shortcomings of these models lie in their inability to capture the frequency or temperature-dependence of viscoelastic materials.

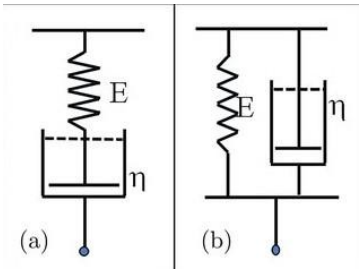

Figure 4 (a) Maxwell element (b) Voigt element

Standard mechanical models such as generalized Maxwell or Voigt models, shown in *Figure 5,* are a more advanced form of rheological models. They are widely used to describe the behavior of VEDs using the theory of linear viscoelasticity [19,23]. Their use is advocated by a number of researchers [31,32]. These models are usually preferred due to their simplicity, sound physical basis, and computational efficiency in explaining the behavior of VEDs. They are comprised of several elementary models such as Maxwell or Voigt models connected in either series or parallel. The most known are the generalized maxwell and generalized kelvin models shown in *Figure 5*. They are proven to capture the frequency-dependent behavior of viscoelastic materials with a reasonable number of parameters [5,31,32]. The parameters of such models are usually obtained in the frequency domain from test data at a range of frequencies.

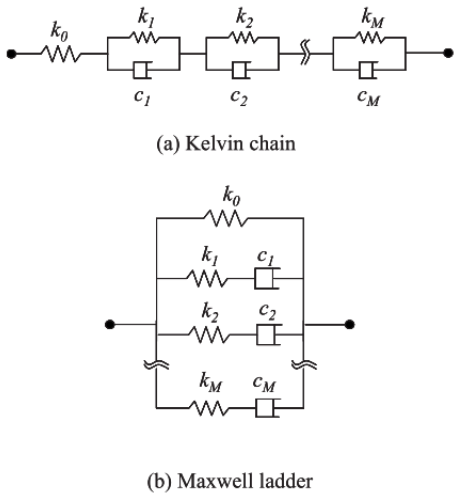

Figure 5 Kelvin chain and Maxwell ladder models (Chang 2009 [33]*)*

To further generalize the modeling of viscoelastic materials ordinary derivatives were replaced by fractional-order time derivatives. This led to a robust approach referred to as the fractional derivative method which have been used to capture the frequency and temperature-dependence and damping properties of VEDs [30,34,35]. The main advantage of fractional derivative models is that they can provide a better fit than a classical maxwell model over a broad range of frequencies with less parameters [36]. Nevertheless, they are composed of more complex mathematical expressions which makes the model numerically cumbersome and therefore less efficient for routine implementation [31]. This explains why the fractional derivative models are not used in commercial finite element (FE) programs.

The Bouc-Wen model is a widely used hysteretic model to describe a wide variety of engineering applications [37]. It has been used in structural control applications in modeling different kinds of damping devices and in the analysis if structures made from different materials [38]. As for VEDs, Bouc-Wen has been used by a number of researchers

but its major drawback that it requires different parameters when used under different strains [27,39].

A visco-hyperelastic material approach assumes that the mechanical response of viscoelastic materials undergoing large deformations can be divided into a rate-independent hyperelastic behavior and a rate-dependent viscoelastic behavior. This approach have been used by a number of researchers to describe elastomeric materials that have frequency dependency [40–42]. It was also used with 3D printed thermoplastic elastomers and can be implemented conveniently using standard mechanical rheological models [43–45].

Hyperelastic behavior is characterized by the strain energy density function, w, under adiabatic conditions:

$$w = w(I_1, I_2, I_3) \quad (2)$$

Where w is expressed in terms of the first, second, and third strain invariants. The stress can then be expressed as follows:

$$\sigma = \frac{\partial w}{\partial \varepsilon} \quad (3)$$

Several hyperelastic material models exist in the literature such as Mooney-Rivlin, Neo Hookean, Yeoh, and Ogden models. The parameters of those models are evaluated through one or more mechanical tests depending on the intended loading application of the material. The stress is then evaluated using those parameters.

The viscoelastic response, however, is characterized using stress-relaxation tests and the relaxation modulus can be represented by Prony series:

$$E(t) = E_e + \sum_{t=1}^{N} E_i e^{\frac{-t}{\tau_i}} \quad 4$$

Where: E_e is the equilibrium modulus at infinite time, E_i and τ_i are the parameters of the Prony series. Although, individually, the terms of Prony series depict only a narrow-band behavior, the series with all the terms included can describe a broad-band behavior [31]. Also, the exponential basis of the Prony series helps immensely in model calibration and interconversion between time and frequency domains.

The Boltzmann super-position, Equation 1, is then used to obtain the total stress of a visco-hyperelastic material through the summation of viscoelastic and hyperelastic stresses. The first term on the right-hand side of the equation is used to represent hyperelastic stresses, while the second term represents viscoelastic stresses. Numerical integration schemes are available to obtain a solution to the convolution integral in the second term such as the one provided by Taylor et al. [46].

2.1.4 Numerical evaluation of steel frame structures with VEDs

Numerical investigation of a 10-story building with VEDs subjected to different earthquake ground motions using a finite element analysis method was carried out by Tsai et al. (1994). It was shown that not only the displacements were reduced but also the stresses of the structure were significantly reduced. Xu et al. (2011) conducted a similar study using 52 VEDs that were employed as a part of a seismic retrofit scheme of a

building. The study showed that the stiffness, damping, and natural frequencies of the structure have increased, while the displacement responses were decreased. Furthermore, Gong et al. (2017) subjected a tall building to several earthquake ground motions using a FE simulation. It was shown that due to the additional stiffness provided by the damper, inter-story drift responses were significantly reduced, whereas floor acceleration and base shear forces not as much. Indicating that the additional stiffness cannot be ignored in the design process. A number of studies utilized the nine-story five-bay steel frame designed for the SAC building project to test their own VED devices numerically [25,49–52].

2.2 Additively manufactured elastomers

Elastomer is a term used to describe rubber and rubber-like materials. The term is made up from the word's elastic and polymer describing the behavior and nature of the material. They typically have a low young's modulus and high elongation at break. These characteristics are enabled by the molecular structure of the crosslinked polymer network which is composed of both flexible and hard segments. Moreover, elastomers, in general, exhibit low crosslinking density and possess high molecular weight. They can be broadly classified as thermoset and thermoplastic elastomers. The latter generates the molecular network structure by thermally induced chemical cross-linking reaction, while the former employs physical crosslinking.

Thermoplastic Elastomers (TPEs) are synthesized by copolymerizing two or more monomers, where one of the monomers provide a hard segment through physical crosslinks that form a crystalline region. While the other monomer provides a soft segment, which is a low glass transition temperature polymer that is amorphous and provides chain flexibility

and mobility. This micro-phase separated network of the TPE structure enables the elastomer, once stressed, to conform and elongate through the long chains, while the crosslinks prevent flow [53]. The 3D dimensional networks of physical crosslinks are made possible by the covalent linkages between the chemically dissimilar soft and hard segments. These covalently crosslinked TPEs are responsible for achieving mechanical properties comparable to vulcanized elastomers or rubber [54]. Examples of TPEs include copolyester elastomers, styerene block copolymers, and polyurethanes. The molecular structure of thermoplastic polyurethane (TPU) which is a reaction product of the compounds shown in *Figure 6*. The ratio of hard/soft segments can be fine-tuned and varied which influence the properties of the final polymer product to yield a wide variety of TPUs [55].

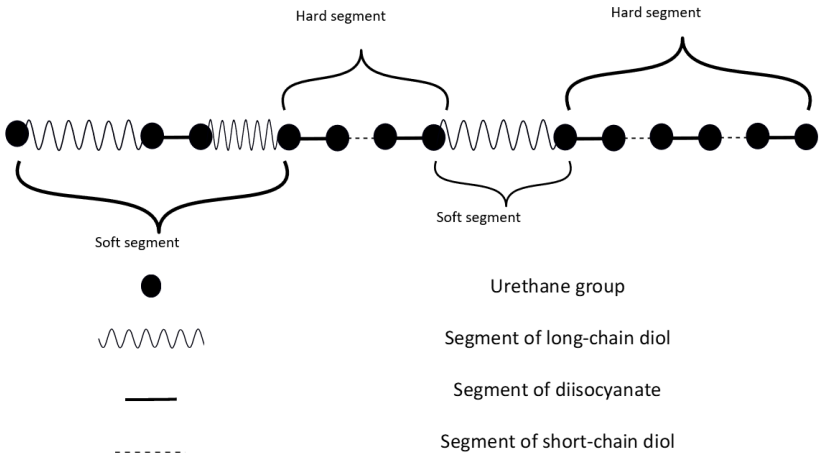

Figure 6 Molecular Structure of TPU, Adapted from McKeen (2017)

The main advantages of TPEs lie in the easy, fast, and energy efficient processing when compared to conventional thermoset (vulcanized) elastomers. Moreover, TPEs are recyclable materials that can be manufactured through extrusion or molding techniques which makes the production cycle of a part shorter [53]. Additive manufacturing (AM) of

elastomers is gaining significant interest due to the versatility of the polymer in terms of the number of existing and potential applications such as tires, gaskets, shoe soles, toothbrushes, bicycle grips, artificial vascular constructs or implants [55]. 3D printed TPE objects can be produced via different AM technologies. They can also retain some of the favorable features and characteristic strengths of bulk TPE such as recyclability, high elongation, and wear resistance. Moreover, it was shown that 3D-printed TPU can achieve densities comparable to bulk TPU if printed with minimal to negative air gap [44] and a similar inelastic behavior as bulk specimens [56]. Nevertheless, the mechanical performance of bulk TPU usually outperforms the 3D-printed one. This is due to the extrusion process that leads to changes in the length and distribution of the hard segment which consequently affects the mechanical properties of TPU [57].

The idea of AM is based on creating successive layers of materials until a complete part is fabricated. The process begins with creating a 3D CAD file that is then sliced into layers using a slicing software. The resolution of these layers is highly dependent on the AM technology used to produce the part. The main technologies as identified by Ngo. et al. [58] are fused deposition modeling (FDM) and contour crafting that depend on material extrusion. In addition, selective laser sintering (SLS) and selective laser melting (SLM) which are powder-based printing techniques, as well as polyjet which is a material jetting method and direct energy deposition (DED) are also main technologies of AM. However, there are still challenges associated with AM in general as well as challenges that are specific to each technology. In general, AM suffers from a limited material selection, inter-

layer bonding defects that affects the mechanical behavior, and the constraints on multi-material printing due to material and technology limitations.

The mechanical properties of 3D printed TPEs can be affected by the technology used to produce it, the chemical composition of the material, loading rate, and print parameters. For instance, Abayazid and Ghajari [45] characterized 3D printed elastomers using Polyjet technology. Test specimens of two types of elastomers were printed and evaluated at different strain rates and build orientations using tensile, compressive, dynamic mechanical analysis, and stress relaxation tests. The mechanical response was found to be highly dependent on strain rate and build orientation, although the effect of the latter diminished at high strain rates. Adams et al. [43] followed the same mechanical characterization method using 3D printed elastomer specimens produced via laser sintered TPE powder. The study concluded that build orientation has a significant effect on overall mechanical properties. Specimens printed ‘flat’ demonstrated the highest stress and strain-to-failure when compared to ‘on edge’ and ‘upright’ specimens. Pagac et al. [59] tested TPU produced via continuous digital light processing (CDLP) method. Cylindrical and dog bone samples were printed at different build orientations and tested in compression and tension, respectively, to obtain the mechanical properties. The test results revealed that anisotropy due to build orientation in CDLP produced TPU can practically be disregarded, and the material can be treated as isotropic.

TPU reinforced with a small amount of functionalized Carbon Nanotubes (CNT) demonstrate improved mechanical, thermal, and electrical properties which makes these composites multi-functional [60]. The effect of adding Multi-wall Carbon Nanotubes

(MWCNTs) into the 3D printed TPU matrix was investigated by Christ et al. [61] for robotic applications. The nanotubes enhanced conductivity and stiffness which improved the printing capability and interlayer adhesion of the printed specimens. Kim et al. [62] developed a multiaxial sensor by printing the TPU/CNT nanocomposite directly on top of the TPU structure. This creates piezo resistivity on the surface of the structure and through changes in resistance, the applied force can be measured.

3D printed TPEs have a huge potential in the future of manufacturing due to the versatility of the material and the design flexibility of AM. Furthermore, the ability to create multifunctional parts is very promising for 3D printed TPE parts and opens the doors for numerous new applications. Nevertheless, 3D printed TPE response can vary significantly based on the technology used to produce it. Therefore, 3D printed TPE using FDM technology only will be discussed to highlight the factors that influence its mechanical properties.

FDM gained a lot of attention due to the simplicity of the whole process, from mechanical design to printing and affordability. It involves the direct deposition of a feedstock material, typically a thermoplastic material, from a heated nozzle in a layer-by-layer fashion. The deposition of an entire layer is done in the XY plane then the printer moves in the Z direction to add more layers. FDM technology featuring dual extrusion is shown in *Figure 7*.

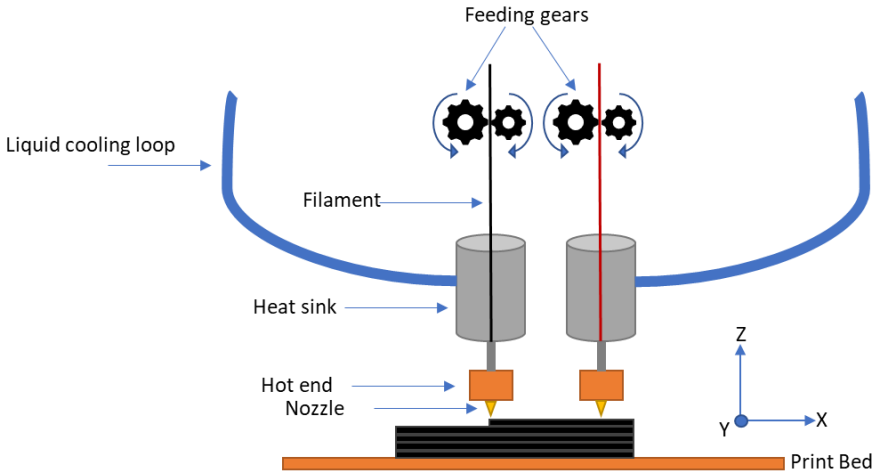

Figure 7 FDM process with dual extrusion

However, it is well-established that the mechanical properties of FDM parts are lower than those fabricated using conventional casting methods. This is explained by the high pressure induced in conventional methods which causes an increase in the density and mechanical properties of the final part. 3D printed parts can be affected by thermally induced stresses which lower its performance. This is caused by deposited polymers cooling down to ambient temperature relatively fast due to low surface area to volume ratio [63]. FDM also suffers from poor interlayer adhesion and object/bed adhesion, and extrusion failure mechanisms. Some challenges are specific to FDM-produced elastomers such as filament buckling through the extrusion head. This occurs when the resistance to flow at the nozzle (viscosity) overcomes the ability of the filament to act as a piston to drive the polymer melt out of the nozzle. This can be avoided by reducing the extrusion speed. Nozzle drool is another problem that can be solved by turning off retraction.

One of the main concerns for FDM-produced parts is anisotropy [64]. The anisotropy stems from the AM process itself where layers are deposited in a layer-by-layer fashion [65]. It can also arise due to the relatively low strength of thermoplastic materials

which causes locations of weak bonds between raster and layers as shown in Figure 8. The review conducted by Popescu et al. [66] concluded that the mechanical properties are strongly influenced by filament bonding which is related to the process parameters chosen for the print. A depiction of filament bonding and voids (airgaps) is shown in Figure 9.

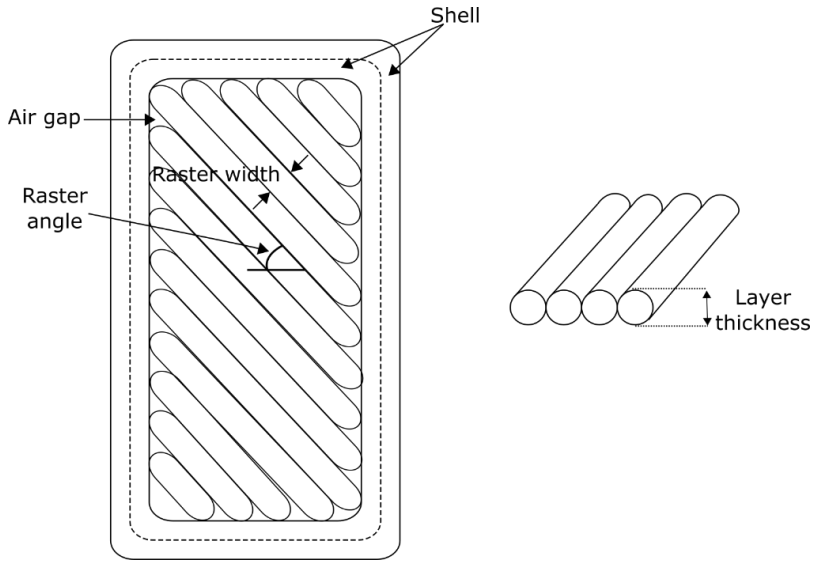

Figure 8 Top view of 3D-printed layer (Adapted from Rahim et al. [63]*)*

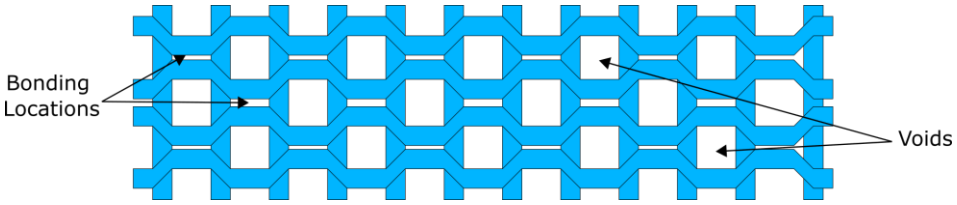

Figure 9 100% Honeycomb filling; bond between rasters and voids (Adapted from Akhoundi et al. [67]*)*

Build orientation and raster orientation, as shown in *Figure 10*, can also be a source of anisotropy in 3D printed parts as it can significantly influence the mechanical properties of 3D printed parts. This knowledge helps in developing a printing strategy-property relationship which greatly affects the mechanical performance of 3D printed parts [64]. It was also shown that different materials can exhibit different anisotropic behaviors [68].

Therefore, the final properties of a 3D printed part are dependent on both the material and printing parameters used.

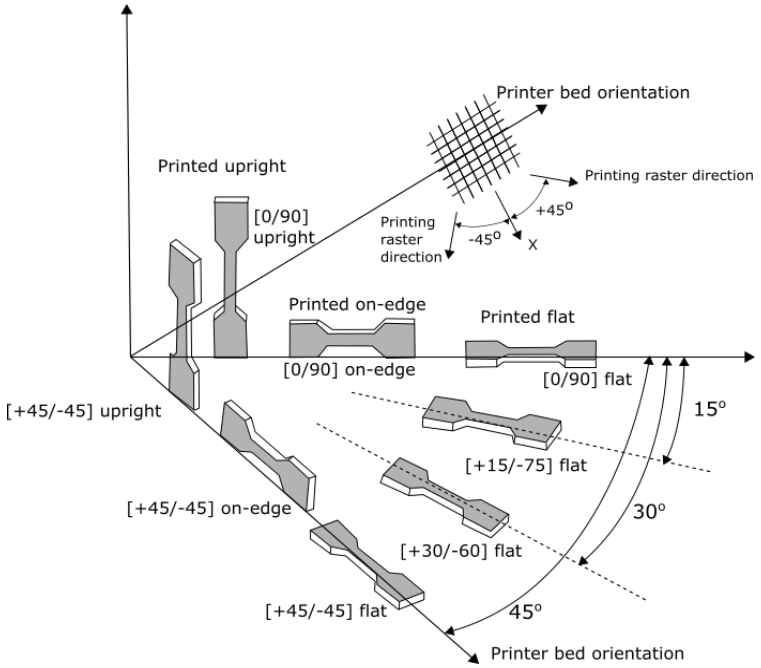

Figure 10 Representation of different build orientations and raster orientations (Adapted from Rohde et al. [68]*)*

Hohimer et al. [69] studied the mechanical properties of FDM-produced TPU and concluded by stating that unlike other rigid thermoplastic materials TPU can be printed to produce isotropic mechanical properties. The results showed that negative air gap is associated with almost isotropic material behavior, regardless of raster orientation or nozzle temperature. While raster orientation has a large influence only on samples with positive air gap. Chaudhry et al. [70] observed that the orientation of the infill did not affect the tensile strength of specimens, however, infill percentage (density) and layer height did affect the tensile strength. Additionally, the effect of process parameters became more evident at high strain rates. The optimum print processing parameters were identified by Xiao et al. [71] to be raster orientation and temperature. The study concluded that 45°

orientation angle and 215°C are the optimum printing parameters for TPU FDM process based on test results. The authors claimed that those parameters help in reducing internal stresses and provide good thermal bonding between layers. Robinson et al. [44] examined 3D printed TPE specimens using tensile, biaxial, and planar tests in a cyclic fashion. The TPE specimens were printed with high resolution and almost 99.97% density which made 3D printed TPE parts achieve high density levels. The material displayed a stress softening behavior in cyclic loading and a dependence on strain rate. In general, there seems to be an agreement in the literature over the importance of density in achieving a high mechanical response.

FDM parts are associated with weak interlayer bond limitations when multiple materials are printed together. Lopes et al. [72] showed that 3D printed multi-material parts produced via FDM are weak at the boundary interface due to the process of switching print heads and the chemical affinity between the materials at the interface. It is also known that most thermoplastic materials have low surface energy and lack polar functional groups on their surface necessary to make strong bond [73]. However, it was shown that the interface adhesion strength can be improved through selecting print processing parameters that reduce thermal stresses and increase wettability. Printing order was recognized as having a noticeable effect on the adhesion of multi material parts [74,75]. It was noticed that better adhesion was achieved when lower viscosity polymers were printed onto higher viscosity ones due to their ability to infiltrate voids. Yin et al. [76] identified the building stage temperature to be the most effective parameter in improving inter-layer adhesion between

two printed materials. This was explained by proximity of printed specimen temperature and the temperature of the building stage during most of the printing time.

The anisotropy of 3D printed TPU parts produced via FDM has been examined in the literature to study how it impacts the mechanical properties. The print process parameters that contribute to the final density of the printed part such as infill percentage and layer height can help in eliminating anisotropic behavior. All those print processing parameters that are involved in inter layer adhesion add to the complexity of the printing process of multi materials parts. This creates a need to combine hard-to-bond FDM-produced materials, such as most thermoplastics used in AM, in a more reliable manner.

2.3 Mechanical Interlocking

Mechanical interlocking is proposed in this work as a way of overcoming the interlayer bond limitation in FDM technology. A prominent feature of interlocking assemblies is that each interlocking element is kinematically constrained by its surrounding neighboring elements. This enables joining different materials in one assembly or structure to work together, therefore, allowing the generation of a wide range of properties. These interlocking assemblies are larger than what is considered microstructural length but smaller than the size of the final part or product [77].

Interlocked geometric assemblies have shown their ability to manipulate the mechanical properties of a structure by controlling the load bearing capacity. The work by Khoshhesab and Li [78] shows that a biomimetic Koch fractal interlocking mechanism was able to increase the load bearing capacity of a structure. However, the mechanical response

is sensitive to geometry imperfections, especially when the fractal complexity increases. Jigsaw-like interlocking sutures were tested using uniaxial pull-out tests by Malik et al. [79]. It was shown that both the pull-out strengths and toughness increase with higher interlocking angles and for higher coefficients of friction. In a subsequent study by the same research group, a bistable jigsaw-like interlocking mechanism was tested for pull-out strengths and showed 10 times the toughness of the polymer material it is made from [12]. In both studies, it was shown through optimization of the interlocking structure that it is preferable to choose low friction coefficient with high locking angles.

They can also alter the failure mode of a structure when a small volume fraction of a soft phase is introduced in a mostly rigid phase geometry to create a more ductile form of failure. Rezaee Javan et al. [80] studied the mechanical response of a "hybrid" topologically interlocked plate that is composed of interlocked concrete blocks with a rubber soft interface between them. A series of quasi-static tests showed that a more ductile mode of failure can be obtained using the hybrid interlocking assembly. Liu et al. (2020) [10] produced tough nacre-like composites using a brick-and-mortar structure. This interlocked structure is characterized by the aspect ratio of stiff polymer (brick) and the volume fraction of stiff polymer to soft polymer (mortar). The high toughness values exhibited by this composite were attributed to the combination of parameters that enables load transfer through the "bricks" without breaking them. The choice of parameters directly affects the modes of failure of the composite.

Tunable and configurable properties have been associated with such geometries also through the introduction of rigid and soft phases. Haldar et al. [81] used a soft damping

polymer as an interlayer between stiff structures joined using a micro architecture interlocking mechanism. The result is a composite structure with simultaneously high stiffness and high damping. Imam et al. [82] investigated the incorporation of hierarchy in an interlocking geometry consisting of circular, jigsaw-like, pattern between brittle polymer blocks that are produced via Polyjet 3D printing technology. The produced parts were studied experimentally and through a finite element analysis. The study found that both stiffness and energy absorption properties can be tuned by incorporating hierarchy in interlocking mechanisms. Moreover, the study revealed two energy dissipation mechanisms induced by interlocking: sliding at the weak interface and fracture in the polymer block. Liu et al. (2019) [11] proposed a class of 3D printed architected materials that consists of inclined flexible beam elements as repeating unit cells where each beam is constrained to a more rigid material at both ends. The developed material structure allows modifying the shear response and controlling energy dissipation under cyclic shear deformations in a rate-independent manner by exploiting the elastic instabilities in the microstructure. Hussey et al. [14] used FDM technology to create 3D printed polycaprolactone tetrahedron unit elements that are kinematically bounded by the surrounding self-repeating unit elements via interlocking. The self-interlocking structure was characterized experimentally and numerically, and the results showed that mechanical properties and energy absorption of the part had a clear dependence on the relative density of the unit cells.

Complex topologically interlocked structures were produced through AM alongside conventional material casting technologies for soft robotic applications. This

technique produces multi-material heterogenous structures with complex geometries that utilizes mechanical anchors between the soft and rigid materials interface. Ma et al. [83] showed the practicality of this technique by producing and testing components in robotic mechanisms like a robotic hand. Rossing et al. [84] utilized the same concept to control the bond between silicone and plastic parts produced via FDM for similar applications involving soft robotics.

Chapter 3: **Characterization of 3D printed Thermoplastic polyurethane (TPU) and viscoelastic energy dissipation device**

3.1 Materials and fabrication of 3D printed specimens

The material used in this study is NinjaFlex® which isa TPU that is commercially available in spools with filament diameter of 1.75 mm from NinjaTek (Manheim, PA, USA), shown in *Figure 11*. This material is a specially formulated thermoplastic polyurethane that contains a low-tack, easy-to-feed texture. It has a durometer shore hardness of 85A which yields flexible and strong prints.

Figure 11 NinjaFlex Thermoplastic Polyurethane

The 3D printer used to produce test specimens is the industrial 3D printer AON-M2 by AON3D (Montreal, QC, Canada) shown in Figure 12. It uses FDM technology with dual independent extruders that allow multi-material printing. The printer uses a direct drive extruder system with a total build volume of 454 x 454 x 640 mm. The hot end extrusion temperature of the printer can reach up to 470°C and it is cooled through a liquid cooling loop system instead of a cooling fan like other commercial printers. The printer also offers the ability to heat the print bed up to 200°C and the build chamber up to 120°C.

Figure 12 AON-M2 3D printer (Courtesy of AON 3D)

The TPU printing process parameters used in this study are provided in Table 1. Those parameters were kept constant for all printed specimens. Variation in the printing process parameters and the effect they have on the mechanical properties of the printed part are discussed in the literature review chapter. Prior to any printing, due to the hygroscopic nature of TPU both the material and the chamber of the 3D printer were maintained at 60 °C for 4h [55].

Table 1 Printing Process Parameters

Parameter	Value
Nozzle diameter (mm)	0.8
Layer height (mm)	0.2
Infill (%)	100
Extrusion Multiplier	1.2
Extruder temperature (°C)	240
chamber temperature (°C)	60
Speed (mm/s)	20

The test specimens were straight pieces of uniform cross-sectional area (105 mm length; 15 mm width; 3.2 mm thickness) as shown in *Figure 13*. The straight specimen was chosen instead of the dog bone specimen because it provides enough width in the gauge length to potentially show the effect of the infill pattern. The specimen was tabbed at both ends with Neoprene of similar thickness and durometer to distribute the tension uniformly

through the cross-section and avoid slippage. Furthermore, the surface of the tabs was roughened using sandpaper to promote better grasp to the UTM grip fixture. All the specimens were produced with one layer that serves as the perimeter of the specimen (wall) and three rectilinear layers on top and bottom at 45 degrees (ceiling and floor).

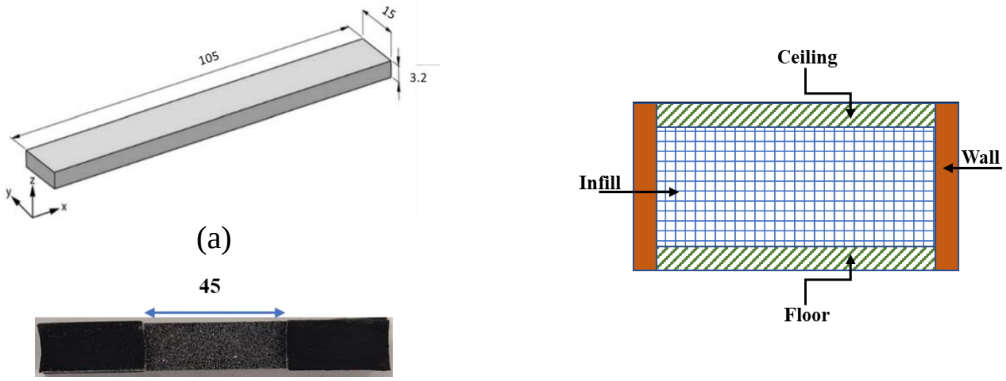

Figure 13 Uniaxial tension specimen: a) specimen dimensions b) gauge length (c) cross-section of specimen normal to y-z plane

The infill patterns used in this test are shown in *Figure 14* with Y-axis being the loading direction, and the nomenclature used with these infill patterns are listed in

Table 2. Specimens used for testing were printed using different infill patterns that are enabled through the default infill patterns provided by the slicing software Simplify3D®. Angle orientation represents the orientation of the deposited layer(s) in a specimen with respect to the loading direction. Deposited layers are printed at a specific angle throughout the part, or multiple angles can be chosen through printing each layer at an angle different than the layers above or below. The rectilinear pattern was printed at different angles to study the effect of orientation. However, the R±45 was printed to explore the effect of having two different angles of layers deposited within the same specimen. The T60 and H0 were printed to check whether geometrical patterns other than rectilinear have an influence over mechanical properties.

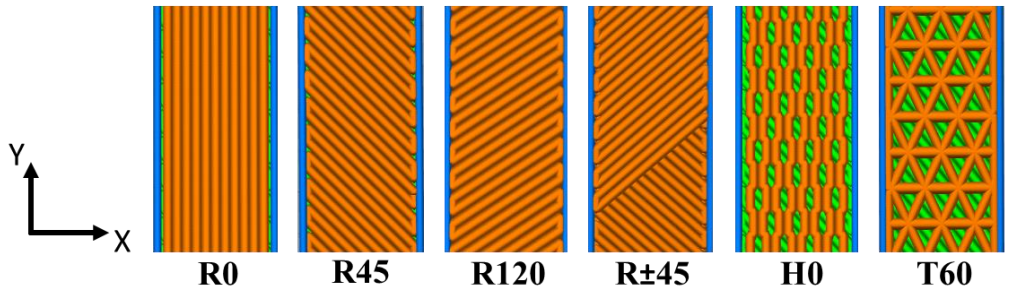

Figure 14 Infill patterns

Table 2 Infill patterns used in uniaxial tension tests

Infill pattern	Angle orientation	Abbreviation
Rectilinear	0	R0
	45	R45
	±45	R±45
	120	R120
Triangular	60	T60
Honeycomb	0	H0

3.2 Methods

3.2.1 Experimental Methods

3.2.1.1 Uniaxial-cyclic tension

A displacement-controlled test was conducted at two crosshead speeds: 5 mm/s and 18 mm/s to check the rate effect using straight specimens with constant cross-section as specified by ASTM D412 - 16. The test was conducted using MTS Bionix servohydraulic system that is equipped with a 25 kN load cell with a resolution of 1 N. Two different sampling frequencies, 30 Hz and 90 Hz, of the test data were used depending on the rate of loading applied.

All the tests were performed in cyclic loading using a ramp function to study the stress softening effect that is inherent in elastomers due to Mullins effect [86]. Each specimen type was cycled 7 times at two different loading rates using the cyclic loading protocol shown in *Figure 15*. The cycling tests stopped once the hysteresis loops reached a state in which inelastic effects cease to increase.

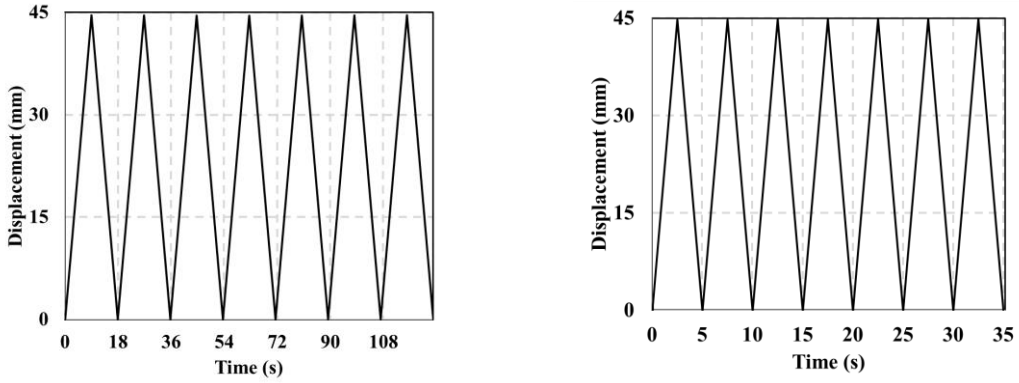

(a) (b)

Figure 15 Loading protocol (a) 5 mm/s (b) 18 mm/s

Prior to uniaxial testing to study the effect of the infill patterns on the uniaxial response of TPU, the mass of each specimen was measured and recorded in *Table 3*. Although the same printing parameters were used for all the specimens, by changing the infill pattern the specimen mass was affected. This is caused by the slicing software which does not account for maintaining the mass of parts with the same infill percentage in its slicing algorithm. Therefore, to produce specimens of different infill patterns and similar mass the printing parameters should be optimized separately for each specimen. It can be observed in *Table 3* that rectilinear patterns in general weigh more than the triangular or honeycomb patterns. This means that rectilinear patterns can achieve higher densities when they are printed which leads to a higher mass compared with specimens of the same volume but with different infill patterns such as H0 and T60.

Table 3 Mass of specimens of different infill patterns

Infill pattern	Mass (g)
R45	5.90 ± 0.20
R120	5.84 ± 0.18
R0	5.85 ± 0.13
R±45	5.90 ± 0.32
T60	5.44 ± 0.28
H0	5.21 ± 0.15

Therefore, to create a fair comparison across the different patterns, all the mechanical properties were normalized by their respective specimen mass and are called thereafter normalized properties. The mechanical properties are studied through comparing the effects of rate, pattern, and the possible interaction between rate and pattern. The properties that are involved in this study are stress, elastic modulus, and dissipated energy.

To evaluate the statistical significance of the obtained properties a randomized complete design is applied in this study to assess the data. The design consists of two factors: rate and pattern with a total of 3 levels of treatment corresponding to each mechanical property. A fixed effect two factor Analysis of Variance (ANOVA) model is used to analyze the data. Hasse diagram shown in *Figure 16* helps to interpret the model. μ is the mean effect of all factors, R and P are the rate and pattern effects, RP is the interaction effect due to the factors, and E represents the error in the experiment. The superscripts and subscripts that are associated with each factor are the factor level and degrees of freedom associated with each factor, respectively. This design of experiment was used on all mechanical properties at both primary and stable responses. The ANOVA study was conducted with a significance level of $\alpha = 0.05$ all throughout the study.

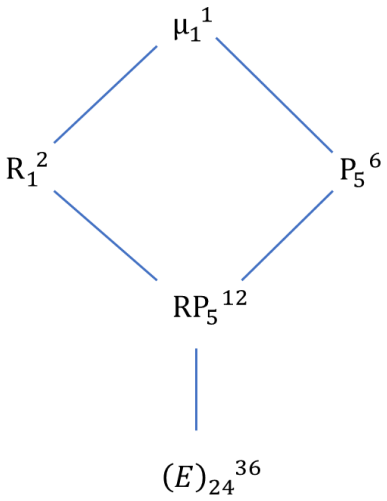

Figure 16 Hasse Diagram

3.2.1.2 Stress-Relaxation

Single step stress-relaxation tests were conducted by first applying uniaxial tension at a fast rate, 60 mm/s, until a fixed strain value of 100% was reached. The strain value was then sustained for a period of at least 100 seconds. The same testing equipment and specimen described in uniaxial tension testing were used for stress relaxation tests. The stress-relaxation test was conducted to explore the viscoelastic properties of the 3D printed TPU and to use these properties later in the numerical modeling of VED. The use of uniaxial tension in measuring the stress relaxation is justified because of the independence of the bulk modulus to time. Therefore, the need for a pure shear stress relaxation test is eliminated, and the normalized young modulus and shear modulus are considered to be equivalent against time [43].

3.2.1.3 Digital Image Correlation (DIC)

DIC is a non-contact optical technique used in the measurement of displacements and strains [87]. This cost-effective technique works by comparing a series of digital images of a test specimen or a component through the different stages of deformation it is

experiencing. 2D-DIC, which is what is used in this research, captures only in-plane deformation measurements. This is done through defining a facet size, the size of the group of pixels that would be tracked using the digital images, and a step size which defines the distance between the facets. The tracking is done between the undeformed image and the deformed images. Match algorithms are then used solve initial guesses using integer-pixel estimation. A center reference point in every facet in the undeformed image is used as an input and then its location in the deformed image can be found. Figure 17 shows a schematic that describes the basic DIC method of tracking images.

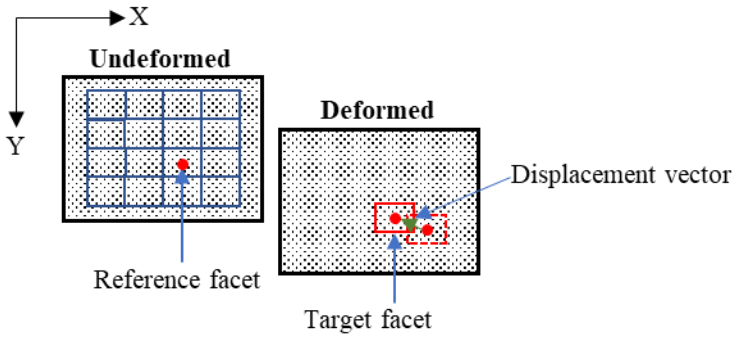

Figure 17 Undeformed and deformed facets in 2D-DIC Adapted from Zhao (2019)

A commonly used function to represent this is the following linear transformation [88]:

$$x^* = u + \frac{\delta u}{\delta x}\Delta x + \frac{\delta u}{\delta y}\Delta y \quad (5)$$

$$y^* = v + \frac{\delta v}{\delta x}\Delta x + \frac{\delta v}{\delta y}\Delta y \quad (6)$$

Where x^* and y^* are the displacements of the center reference point; u and v are the displacement components of the center reference point; Δx and Δy are the initial

distance between an arbitrary point in the facet and the center reference point; $\frac{\delta u}{\delta x}$, $\frac{\delta u}{\delta y}$, $\frac{\delta v}{\delta x}$, $\frac{\delta v}{\delta y}$ are displacement gradient components of the reference point.

The tracking of those facets usually requires creating a high-contrast speckled pattern on the surface of the specimen [89]. *Figure 18* shows the specimens with the speckled pattern covering their gauge length. PlastiDip® which is a silicone-based coating material was used to create a speckled pattern on the specimen. The white coating was applied by holding the can 15 cm from the black surface of the specimen and spraying. PlastiDip® proved to work well because of the highly stretchable and wear resistant nature of the coating.

Figure 18 Tabbed specimen prepared with a speckled pattern for DIC

A Sony® AX33 4K camera with CMOS sensor was used for recording videos. High intensity lights were used to illuminate the tested specimen. The videos were recorded in a high contrast black and white mode to improve the distinction between contrasting colors. They were then converted into images to be analyzed using GOM Correlate software for strain computations. The data sampling rate for the tensile test conducted was chosen to be equal to the maximum frames per seconds produced by the camera which is 30. For the analysis of the images, A facet size of 37 pixels and a step size or distance of 14 pixels were used for strain computations. Two facet points at a known distance from each other

are entered into the surface component that is defined by the software on the image of the specimen. The two points are then tracked throughout the loading and unloading regimes to measure the strain. The DIC setup used in this work is shown in *Figure 19*.

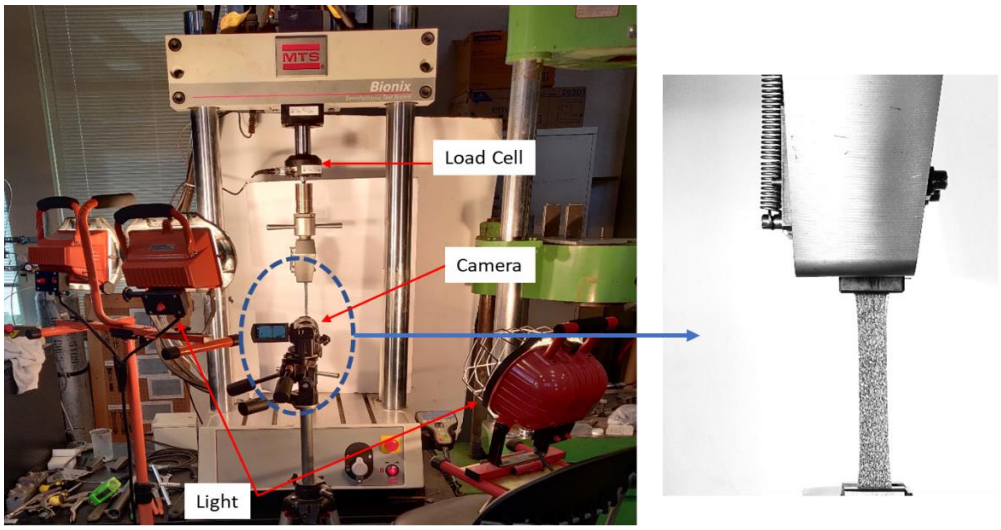

Figure 19 DIC setup of the test showing the universal testing machine, test speciemen with speckled pattern on surface, camera to capture images at high rates, and lights necessary to eliminate the effect of shadows

3.2.1.4 Viscoelastic damper testing

The VED was assembled using two 3D printed TPU blocks with an infill pattern R45 and A36 steel plates that function as the rigid parts of the damper. An ethyl cyanoacrylate glue, Loctite® 401, was used to adhere the parts together. To promote and enhance the adhesion in low surface energy TPU, Loctite® 770 low viscosity primer was applied on the TPU surface prior to applying the cyanoacrylate adhesive while the steel plates were sand blasted. The primer functions as a bonding layer between the substrate and the adhesive. The VED assembly was left for a period of 24 hours to achieve full functional strength. A schematic for the tested VED is shown in *Figure 20*.

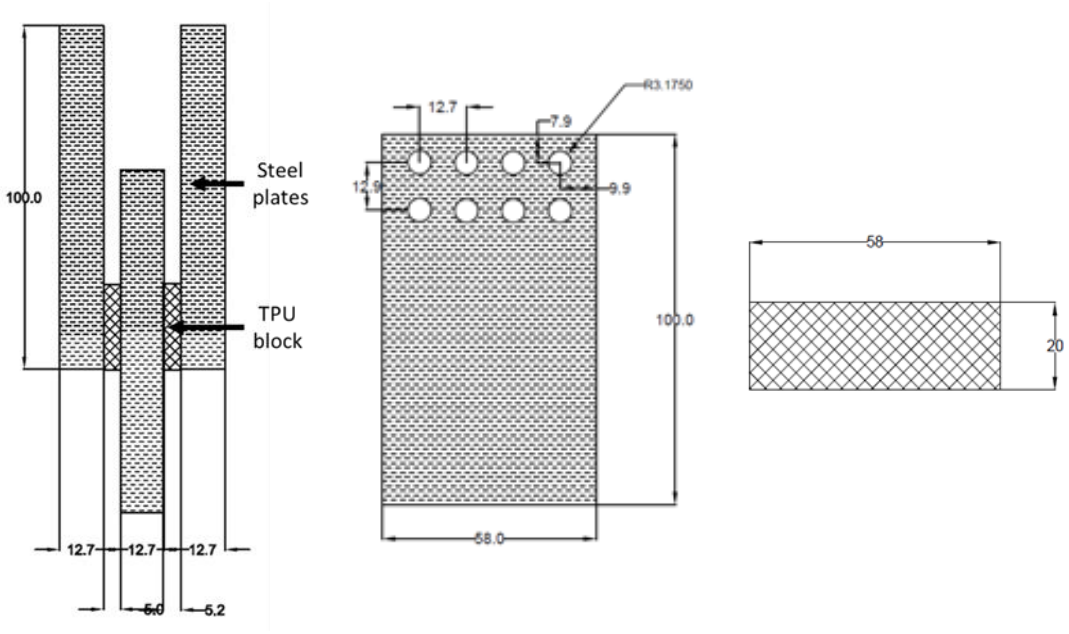

(a) (b) (c)

Figure 20 Dimensions of 3D printed VED (a) Geometry of tested VED (b) Steel plate connected to VED (c) TPU block. All dimensions in mm.

A special test setup, shown in *Figure 21*, was fabricated to test the VED. The setup is adjustable in a way that would accommodate different thicknesses of the tested damper. The moveable part of the test setup slides into the fixed part which is connected to the UTM on top and bottom. The damper is then bolted to the moveable part.

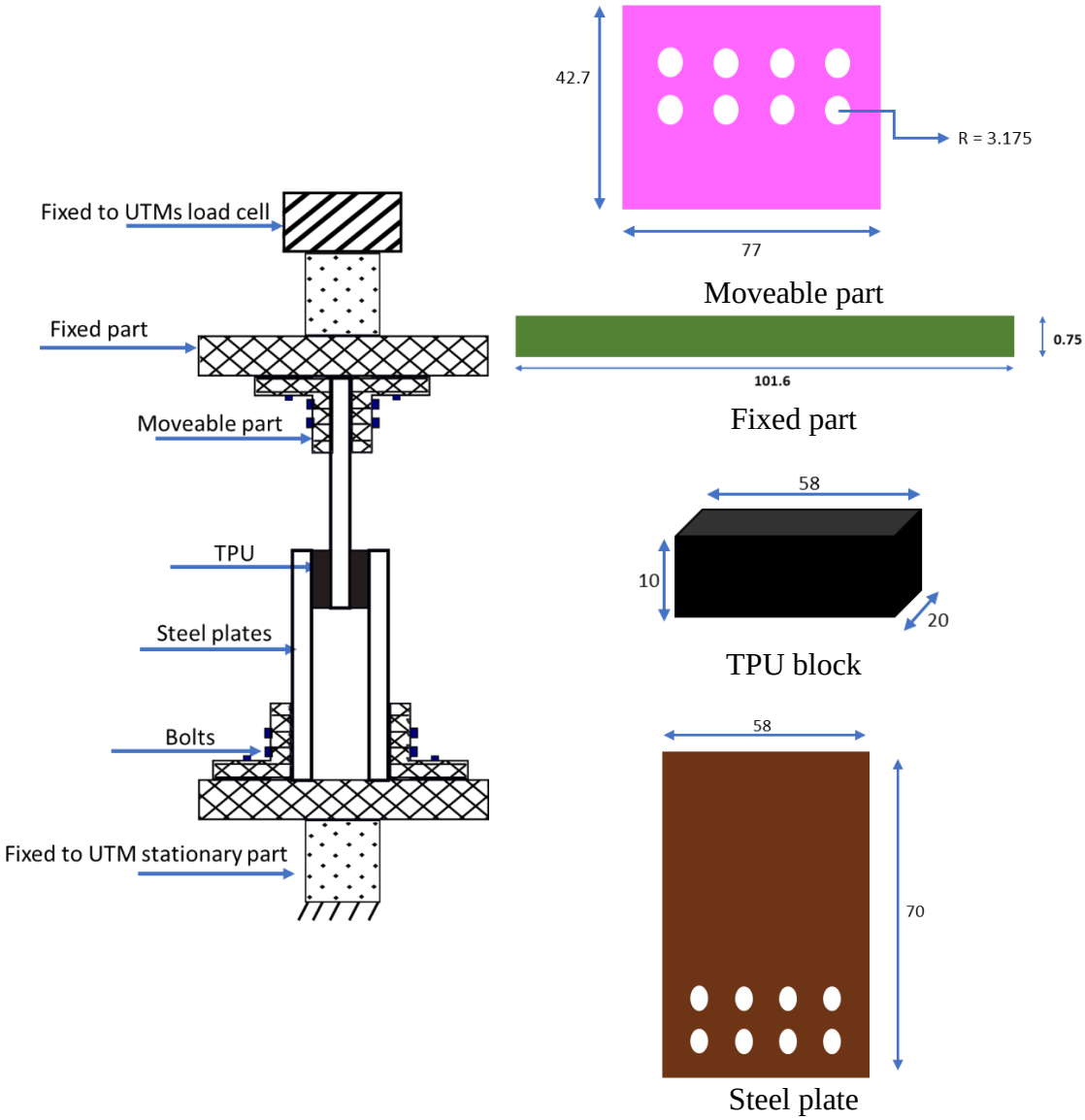

Figure 21 VED test setup

The damper was evaluated according to the testing program shown in *Figure 22* and summarized in *Table 4*. This testing program is designed to assess the damper at different amplitudes and frequencies.

Table 4 VED testing program

Amplitude (mm)	Number of cycles	Shear strain (mm/mm)	Frequency (Hz)
±1	10	0.1	0.05, 0.15, 0.3, 0.5
±3	10	0.6	0.05, 0.15, 0.3, 0.5
±5	10	1	0.05, 0.15, 0.3, 0.5

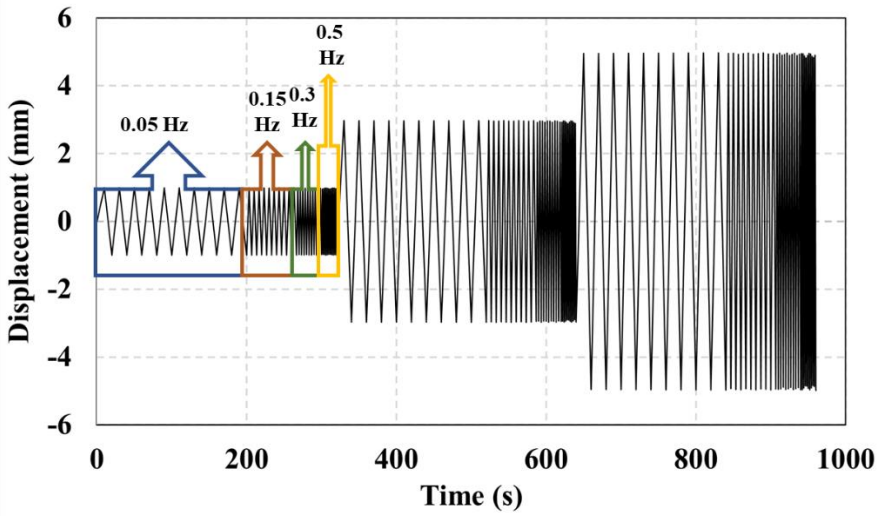

Figure 22 VED loading protocol

3.2.2 Computational Methods

3.2.2.1 Material Modeling

The material model development consists of two parts: a hyperelastic material model and a linear viscoelastic material model which are integrated to produce a visco-hyperelastic material model. The elastic response of TPU was modeled using a hyperelastic constitutive model to account for the large deformations it undergoes. Whereas a viscoelastic constitutive model that represents the internal damping of the material was used to characterize the time-dependent response. The influence of temperature was not considered in the proposed material model. Test data of uniaxial responses were curve fitted into different hyperelastic models using ABAQUS® to evaluate the materials

response. The curve fitting procedure obtains the appropriate parameters of the strain energy potentials chosen for evaluation through a least square fit. The material is assumed to be an isotropic incompressible solid (no volumetric changes) which is appropriate for elastomers especially in applications where the material is not highly confined [90].

Two types of hyperelastic strain energy functions were used in this work: Ogden strain energy function and reduced polynomial strain energy function. The Ogden strain energy function [91] assuming incompressibility is given by:

$$W = \sum_{i=1}^{N} \frac{2\mu_i}{\alpha_i} (\lambda_1^{\alpha_i} + \lambda_2^{\alpha_i} + \lambda_3^{\alpha_i} - 3) \qquad 7$$

Where λ_1, λ_2, and λ_3 are the principal stretches, μ_i is the shear modulus, and α_i is a non-dimensional material constant. The nominal stress-strain equation for the uniaxial mode can be derived as follows:

$$\sigma_U = \frac{\partial W}{\partial \lambda_U} = \sum_{i=1}^{N} \frac{2\mu_i}{\alpha_i} (\lambda_U^{\alpha_{i-1}} - \lambda_U^{-0.5\alpha_i - 1}) \qquad 8$$

Where: $\lambda_1 = \lambda_U$, $\lambda_2 = \lambda_3 = \lambda_U^{-0.5}$, and $\lambda_U = 1 + \epsilon_U$. The reduced polynomial strain energy function which is a particular form of the polynomial function proposed by Rivlin and Saunders [92] provided the best fit and therefore it was used in this study. The reduced polynomial strain energy function assuming incompressibility is given by:

$$W = \sum_{i=1}^{N} C_{i0} (\bar{I}_1 - 3)^i \qquad 9$$

Where: C_{i0} is a material parameter and $\bar{I}_1$ is the first deviatoric strain invariant. The nominal stress-strain equation for the uniaxial mode can be derived as follows:

$$\sigma_U = \frac{\partial W}{\partial \lambda_U} = 2(\lambda_U - \lambda_U^{-2}) \sum_{i=1}^{N} i C_{i0} \, (\bar{I}_1 - 3)^{i-1} \qquad 10$$

Where: λ_1 is the principal stretch where: $\lambda_1 = \lambda_U$ and $\lambda_U = 1 + \epsilon_U$.

The general constitutive relation that governs the stress-strain relationship for viscoelastic materials can be represented in the following integral form using the Boltzmann superposition principle:

$$\sigma = \varepsilon_0 G(t) + \int_0^t G_R(t-s) \frac{d\varepsilon(s)}{ds} ds \qquad 11$$

Where the first term on the right-hand side of the equation can be used to represent hyperelastic stresses, while the second term represents viscoelastic stresses. $G(t)$ and $G_R(t-s)$ are the instantaneous and time-dependent shear relaxation modulus, respectively. ε_0 and $d\varepsilon(s)/ds$ are the strain at time t and the applied strain rate at time s, respectively. The shear relaxation modulus can be written in dimensionless form using the instantaneous shear modulus (G_0):

$$g_R(t) = \frac{G_R(t)}{G_0} \qquad 12$$

Linear viscoelastic behavior can be numerically modeled using a Prony series expansion of the dimensionless relaxation modulus:

$$g_R(t) = 1 - \sum_{i=1}^{N} \bar{g}_i^p \, (1 - e^{\frac{t}{\tau_i}}) \qquad 14$$

The relaxation coefficients can be applied to the constants that define the energy function. The Ogden function containing relaxation coefficients is formulated as follows:

$$\mu_i^R(t) = \mu_i^0 \left(1 - \sum_{i=1}^{N} \bar{g}_i^p \left(1 - e^{\frac{t}{\tau}} \right) \right) \qquad 15$$

While the reduced polynomial function containing relaxation coefficients is formulated as follows:

$$C_{ij}^R(t) = C_{ij}^0 \left(1 - \sum_{i=1}^{N} \bar{g}_i^p \left(1 - e^{\frac{t}{\tau}} \right) \right) \qquad 16$$

The steel was modeled using a linear elastic material model with an elastic modulus and Poisson's ratio equal to 210 GPa and 0.3, respectively.

3.2.2.2 Modeling procedure

A 2D model was developed for the TPU specimen with the same dimensions used in the experiment shown in *Figure 23*. The mesh size was different for different regions within the model. The tabbed areas of the specimen, shown in *Figure 23*.a, are meshed using 1 mm global mesh size, while in the gauge area the mesh size transitioned from 4 mm to 1 mm in the gauge length to prevent stress singularities when load is applied. A 4-node bilinear plane strain quadrilateral, hybrid, constant pressure element (CPE4H) was used for TPU. The boundary conditions were applied on the nodes of the tabbed areas as

shown in *Figure 23*.b. Nodes in the left tab were fixed in displacements and rotations, while the displacement loading was applied to nodes in the right tab.

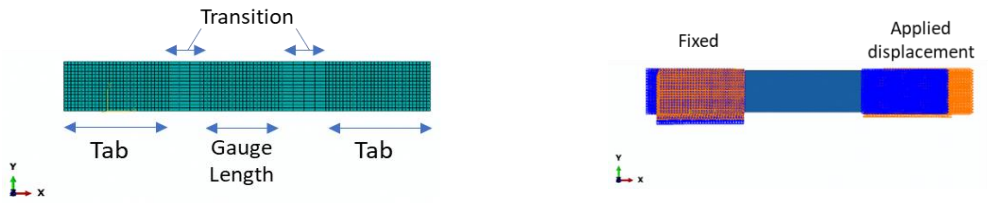

(a) (b)

Figure 23 2D model of TPU specimen (a) mesh details (b) boundary conditions

A 2D model of a viscoelastic damper was created consisting of three A36 steel plates with TPU sandwiched in between them. The TPU was assumed to be perfectly bonded to the steel plates using surface-to-surface tie constraints. All degrees of freedom were fixed in all three directions on one side of the damper. Mesh details and boundary conditions are shown in *Figure 24*. The loading scheme was enabled via a displacement boundary condition that was applied on the surface of the middle steel plate using an amplitude periodic function to simulate deformation. A 2 mm global seed was generated for the TPU part. Since TPU was assumed to be incompressible, due to the nature of the application, hybrid elements were used in the simulation. The same CPE4H element was used again for the TPU. As for the steel plates, a 10 mm global seed was used for a 4-node bilinear plane strain quadrilateral element (CPE4).

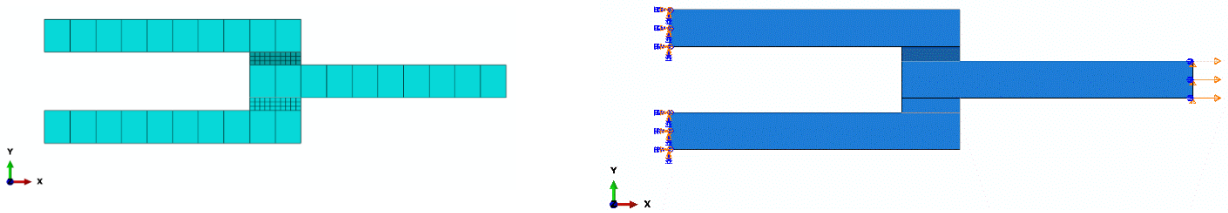

(a) (b)

Figure 24 VED model (a) mesh details (b) Boundary conditions

3.3 Results and Discussion

3.3.1 Effect of infill pattern and rate on 3D printed TPU specimens

All the tested TPU specimens exhibited a non-linear behavior accompanied by inelastic effects such as stress-softening and residual strain which is expected of elastomers. Both inelastic effects can be observed in *Figure 25* which shows a typical behavior of TPU specimens when tested cyclically. The figure shows that the stress drops with each consecutive cycle, while the initial strain does not return to its initial position indicating residual strain (ϵ_r). The residual strain depends on $\epsilon_{\max}$; the applied maximum strain which was fixed at 100% for testing of all infill patterns.

The cyclic response is divided into two parts: a primary response and a stable response. A primary response is represented by the first loading-unloading cycle where the response is defined by the maximum primary stress (σ_p) and a primary elastic modulus (E_p). Whereas the loading-unloading cycle of the stable part is determined based on the number of cycles it took to reach constant inelastic effects and achieve a stable hysteresis curve. In this case, it was the third cycle that corresponded to a stable response. The stable response is characterized by the maximum stable stress (σ_s) and the stable elastic modulus (E_s). The calculation of the elastic modulus was extracted from the loading curve for both primary and stable responses considering strains from 0 – 10%.

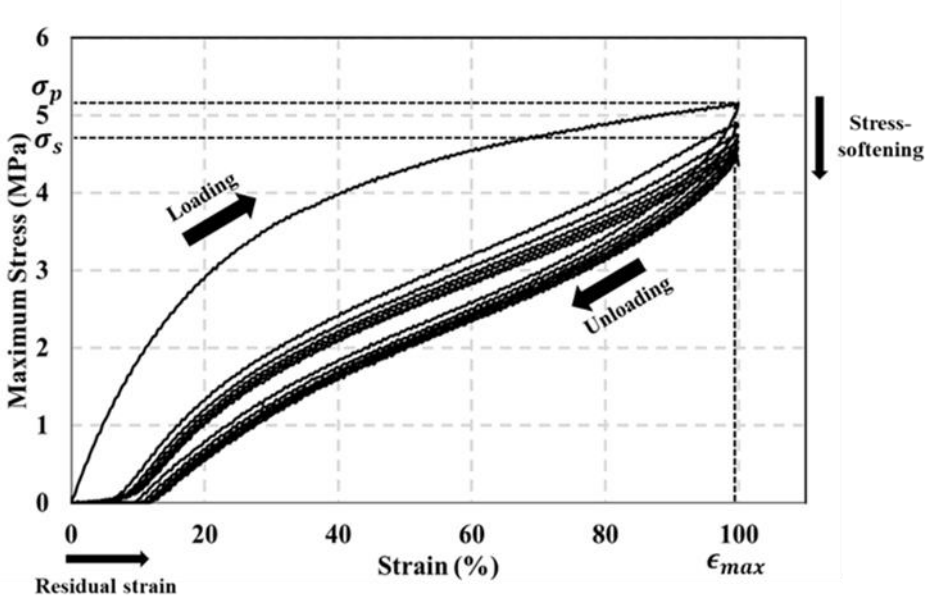

Figure 25 Typical stress-strain response of 3D printed R45 TPU specimens in cyclic uniaxial tests

The stress was obtained by dividing the force recorded by the machine over the initial area of the specimen. While the strain as previously mentioned was captured using DIC. The DIC method involved using GOM Correlate software in calculating the strains by defining two facet points, which are individual pixels shown in *Figure 26*, to be tracked for displacement measurements throughout the test. The images were analyzed and the difference in displacements was recorded at each time step and then divided by the original initial distance between them.

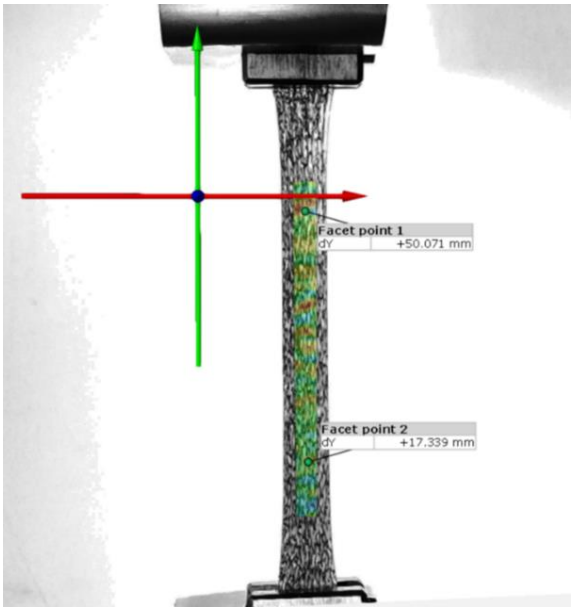

Figure 26 DIC analysis showing the displacement of two facet points for strain calculations

Figure 27 shows both the primary and stable responses of TPU at two rates. The primary response shows the loading curve of the first cycle. Whereas the stable response shows the loading curve of the stabilized response (third cycle) of the hyperelastic behavior that is constructed by eliminating ϵ_r and restarting the reloading curve from the point of zero strain. Due to this elimination the final strains of the stabilized responses vary. The two loading rates used in this study are 5 mm/s and 18 mm/s which are equivalent to strain rates of 0.2 1/s and 0.055 1/s, respectively. It is noticed from *Figure 27* that the higher rate leads to a higher stress-strain response of the TPU specimen. Also, the difference between specimens tested at the two rates becomes smaller as the specimens are reaching a stable response.

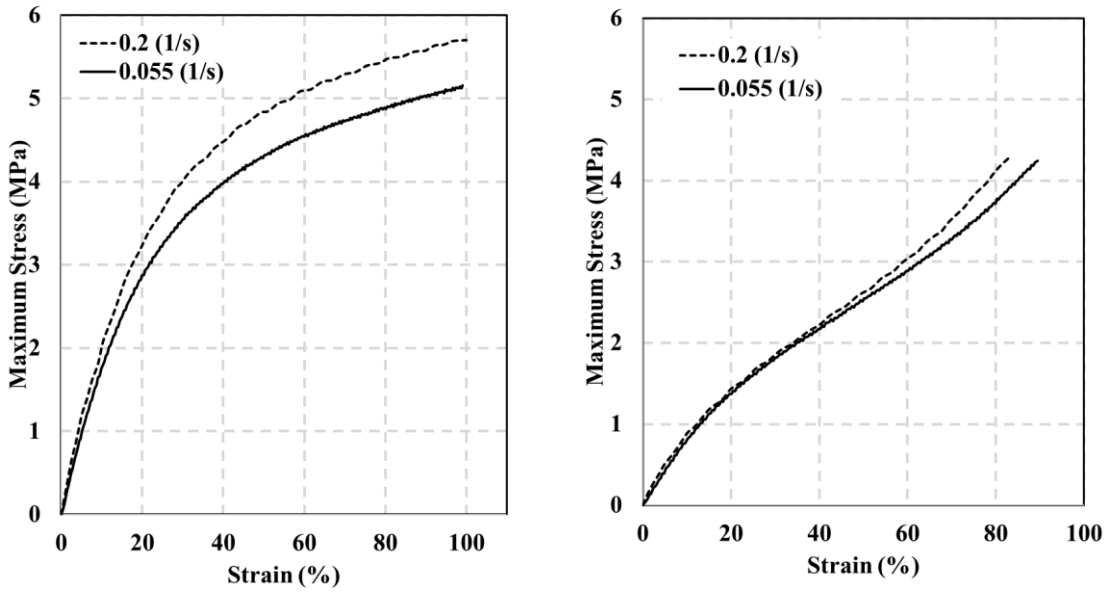

(a) (b)

Figure 27 Cyclic tension response at two strain rates 0.2 1/s and 0.055 1/s of R45 TPU specimen (a) Primary response and (b) Stable response

Table 5 Summary of mechanical properties of tested TPU specimens

	R0		R45		R120		R±45		H0		T60	
Strain rate (1/s)	0.055	0.2	0.055	0.2	0.055	0.2	0.055	0.2	0.055	0.2	0.055	0.2
σ_p (MPa)	5.02	5.68	5.05	5.76	4.83	5.75	4.98	5.60	4.72	4.83	4.45	5.16
E_p (MPa)	18.45	47.76	19.27	41.75	18.63	33.60	20.34	35.55	18.91	34.41	18.20	33.77
ED_p (Joule)	3429	3910	3640	3934	3309	3998	3311	3802	3231	3198	3078	3712
σ_s (MPa)	4.31	4.21	4.16	4.29	3.98	4.36	4.11	4.08	3.97	3.43	3.61	3.80
E_s (MPa)	7.33	8.43	9.11	10.83	8.69	9.44	9.26	7.78	9.27	6.09	8.13	6.82
ED_s (Joule)	987	1146	1032	1165	969	1153	975	1120	917	908	879	1105

The results of the cyclic tensile test are summarized in

Table 5. It can be observed from the results that the rectilinear pattern in its different angle orientations has outperformed both the honeycomb and triangular patterns in almost

all the mechanical properties. Nevertheless, the results obtained in the table below are affected by the mass of each specimen as specimens with higher mass registered a higher mechanical response.

Figure 28 shows the primary and stable responses of normalized stress and elastic modulus at two strain rates for all the tested specimens. The results show that the increase in strain rate causes primary responses to increase, whereas stable responses did not show any significant changes between rates. This might be explained by the sudden changes that occur in the entangled chains, as demonstrated in *Figure 29*, of the polymer when deformations are applied at high strain rate. The chains must reorient themselves abruptly to accommodate the macroscopic deformations and the material will not have enough time to adapt with the applied deformations [42,93]. However, once the response stabilizes, all the polymer chains have already been stretched and oriented in the loading direction, and the rate effect that was evident in the primary response disappears.

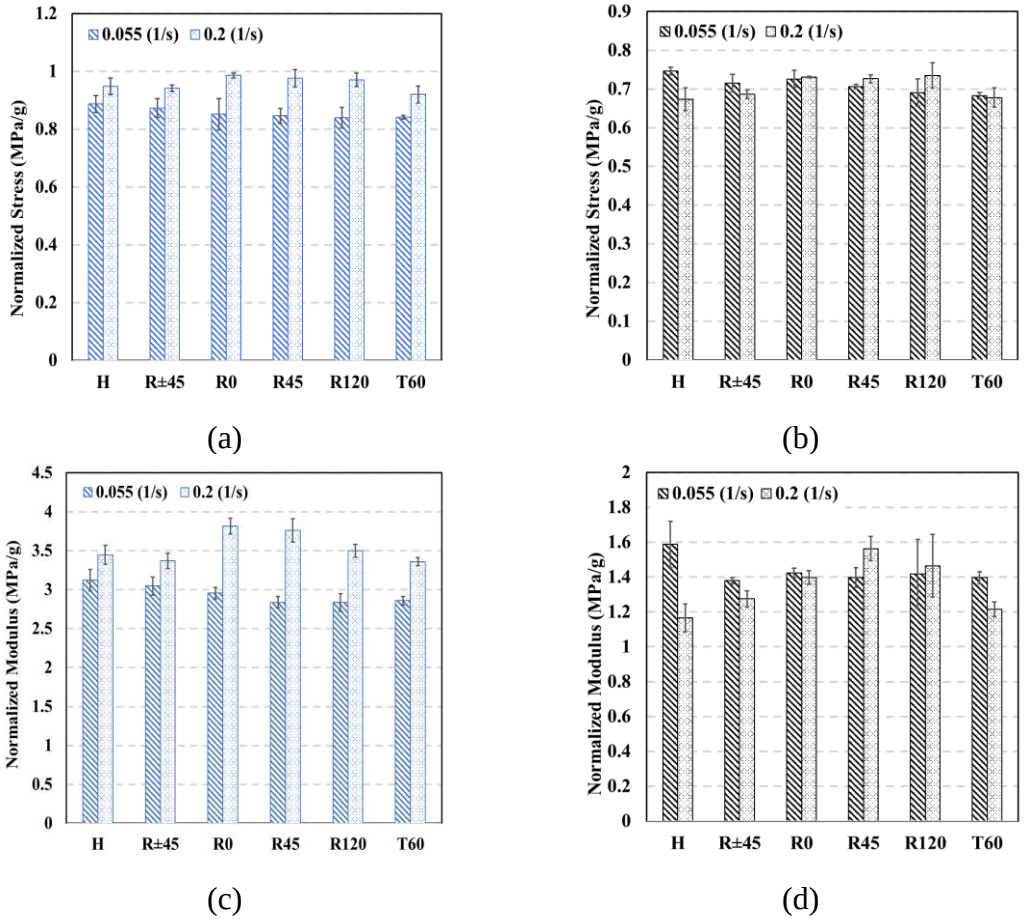

Figure 28 Primary and stable responses of tested specimens at two different rates (a) Primary stress (b) Stable stress (c) Primary modulus (d) Stable modulus

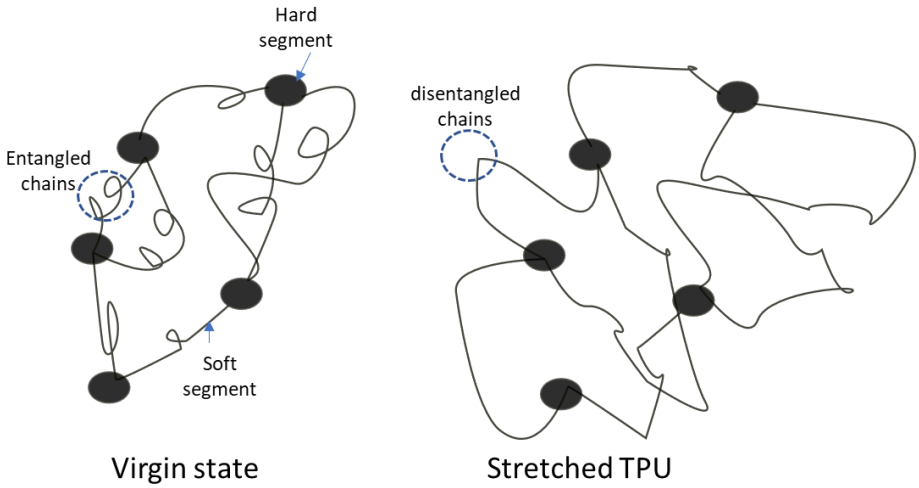

Figure 29 Molecular network for TPU showing virgin and stretched states

The dissipated Energy (ED) was also evaluated for each specimen in primary and stable responses. It is defined as the area entrapped between the loading and unloading curves of the force-displacement response, as seen in *Figure 30*, measured directly from the testing machine. It is defined mathematically according to Equation 17.

$$\mathrm{ED} = \int_0^{x_{max}} F_{Loading}\, dx - \int_0^{x_{max}} F_{Unloading}\, dx \qquad 17$$

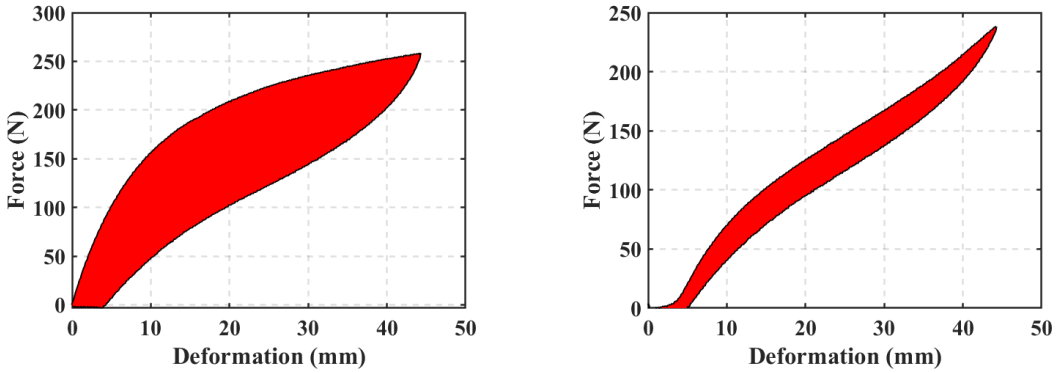

(a) (b)

Figure 30 Energy dissipation description in force-displacement response at two different rates (a) Primary response (b) Stable response

Figure 31 shows comparison of the energy dissipated for all patterns in both primary and stable responses. The results demonstrate that higher rate yielded higher energies in both primary and stable response.

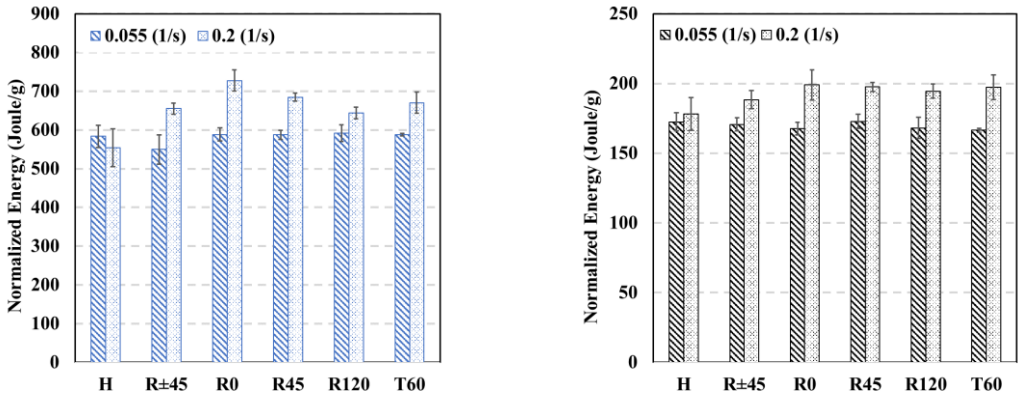

(a) (b)

Figure 31 Primary and stable responses of tested specimens at two different rates (a) Primary energy (b) Stable energy

The results of the two factor ANOVA analysis showed that the only factor that created a statistical significance is strain rate. Although, this significance is only established for properties measured at the primary response. Once the response stabilizes the properties do not differ with different rates applied. On the other hand, the pattern and the interaction effect of rate-pattern had no impact on the mechanical properties. Appendix 1 shows a summary of the results from ANOVA in a tabulated form.

The results indicate that 3D printed TPU acts as an isotropic material with similar inelastic behavior regardless of the filament orientation. This observation also shows that FDM technology, with its filament microstructure, produces specimens that can obtain similar mechanical properties to bulk TPU with no significant influence from filament orientation and interface. The normalization also showed that the infill density of the printed specimen is what governs its mechanical properties. Robinson and Hohimer [44,69] reached similar conclusions in relation to reducing air gap between layers to reach high

and almost isotropic material behavior. Ultimately, the R45 pattern was used to print the TPU because it resulted in the highest mass or part density.

The inelastic effect of residual strain is also studied and compared across the different patterns and the results are shown in *Figure 32*. At a low strain rate, the residual strain values did not vary much from one pattern to the other. As the rate was increased, the residual strain values also increased indicating higher damage to the specimen. This shows that the application of higher rate causes more inelastic damage in the TPU specimen in the form of residual strain.

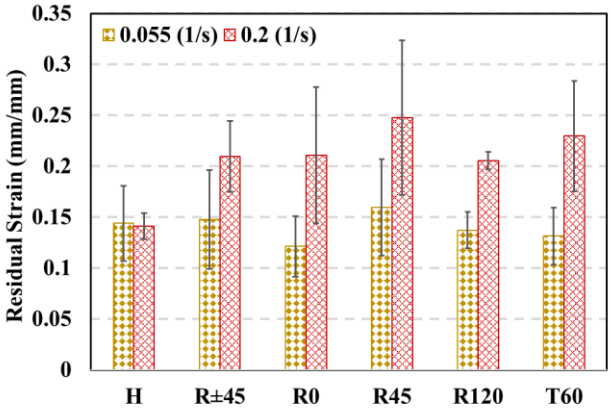

Figure 32 Residual strains of TPU specimens at two different strain rates

The effect of different rates on the stable/primary ratio is shown in *Figure 33*. It was observed that the ratio is consistent for all mechanical properties within the same rate for all the patterns. The ratio for stress and modulus dropped as the rate was increased for every pattern, indicating that more damage is induced in TPU at higher loading rates. Conversely, the energy dissipation ratio did not change with strain rate regardless of the mass and infill pattern of the tested specimen. This means that the stable energy will always have a consistent drop from the primary response of about 70% when it is strained to ϵ_{max}=

1. Therefore, damage induced due to inelastic effects has a higher impact on maximum stress and modulus at higher rates, whereas energy dissipation is impacted the same at both rates.

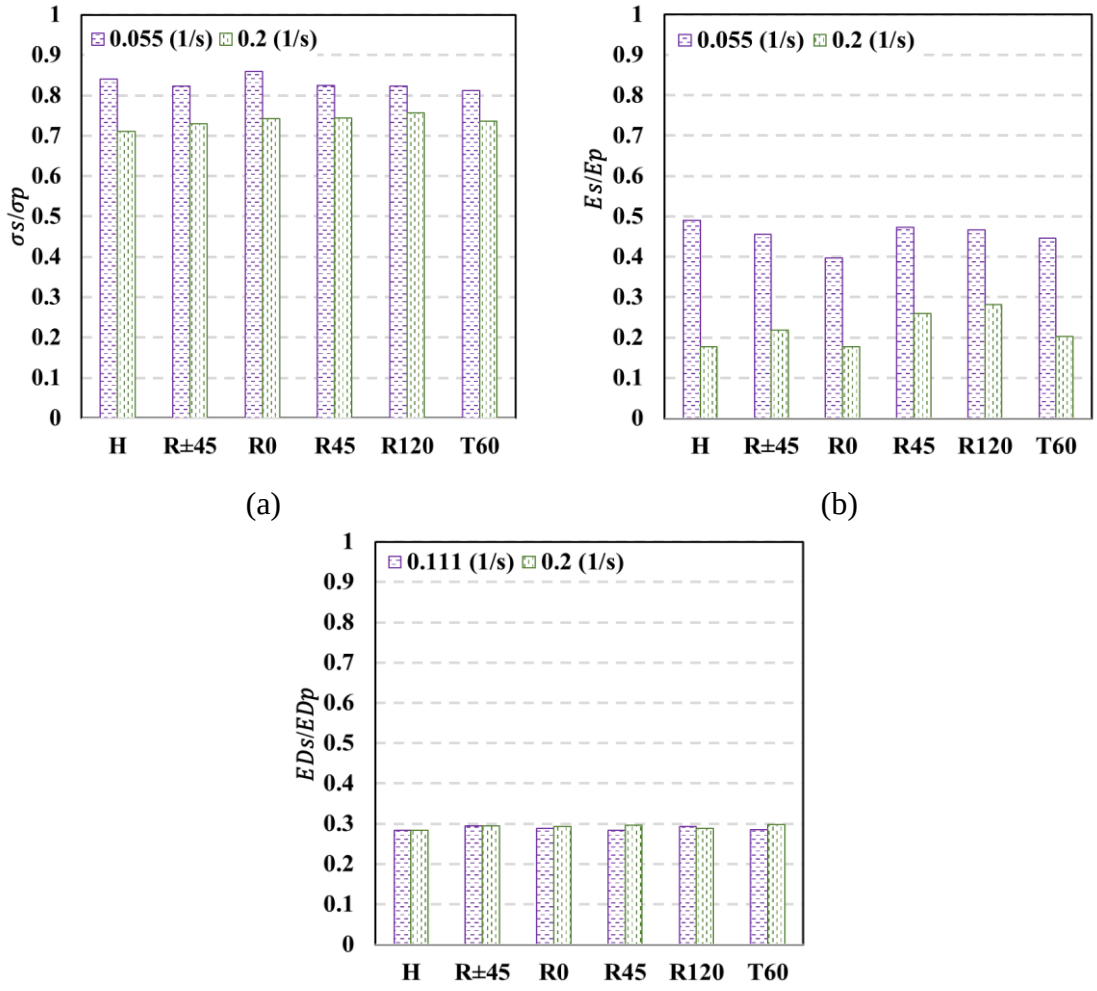

Figure 33 Stable over primary response at two different rates for (a) stress (b) modulus (c) dissipated energy

Finally, the infill pattern that was chosen for implementation in a VED is R45. This pattern has shown that it achieves high energy dissipation due to the high part density attained when printed using the same printing parameters as other infill patterns.

3.3.2 VED Testing

The 3D printed TPU blocks were printed using R45 pattern in the dimensions shown in *Figure 21*. The VED testing configuration is shown in Figure 34.

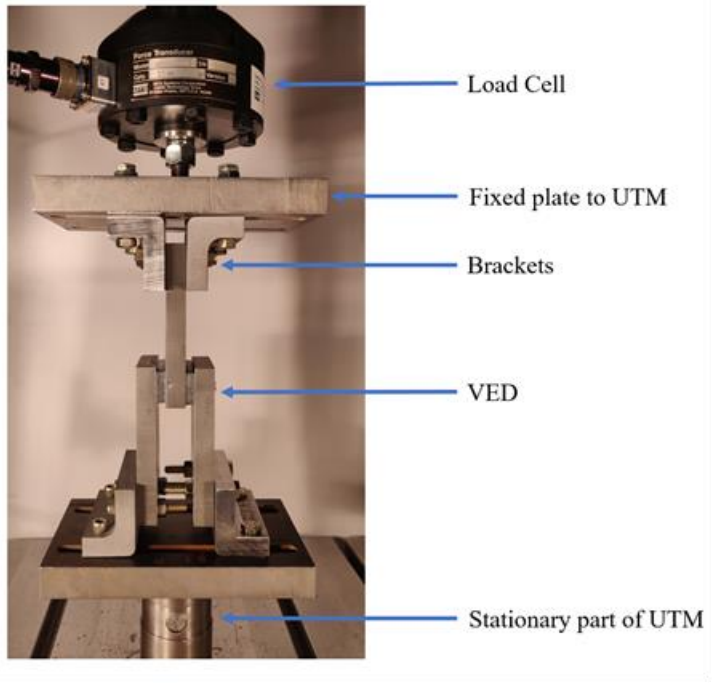

Figure 34 VED test setup

*Figure 35*a shows the results of the tested damper at 0.05 Hz frequency for amplitudes of 1, 3, and 5 mm. It can be observed that the change in amplitude does not significantly affect the tilt of the response (stiffness of the device) for 1 mm and 3 mm amplitudes, whereas the 5 mm amplitude response showed lower stiffness. This drop in stiffness is caused by the gradual failure of the adhesive connecting TPU to steel at 5 mm amplitude as shown in *Figure 35*.c. *Figure 35*.b, shows the response of the damper at an amplitude of 3 mm at different frequencies. Each response is taken from the first cycle of the tested frequency except for 0.05 Hz where both first and second cycles were taken. This

selection was made to show the significance of the initial stress softening in the material. Once the stress softening ceased to progress, the VED did not display a change in stiffness even as the frequency increased. Therefore, the stiffness response of TPU in simple shear motion is not significantly affected by the frequency of the applied displacement at the tested frequency range. Nevertheless, TPU is affected by the inelastic effects such as stress softening and residual strain, as can be observed clearly in Figure 35.b.

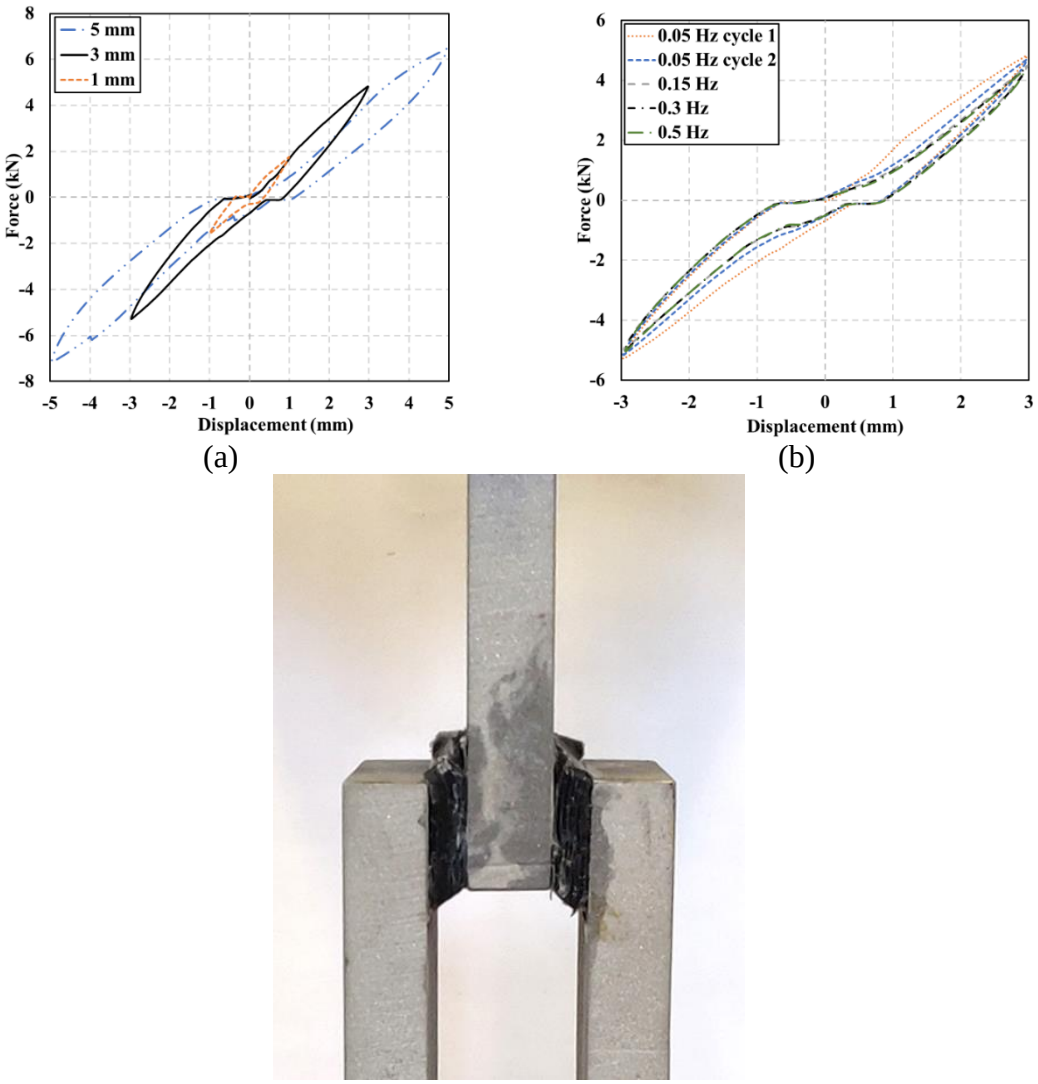

Figure 35 Force-Displacement response of VED (a) at 1, 3, and 5 mm amplitudes (b) 3 mm amplitude at all frequencies (c) adhesive failure at 5 mm amplitude

As a potential material to be used in VED devices; 3D printed TPU was compared to dampers made out of nitrile butadiene rubber (NBR) and silicon rubber (SR) produced by Xu et al. [30]. The energy dissipation efficiency is compared using a damping efficiency coefficient (η) representing the ratio of the normalized dissipated energy to the applied energy as described by Equation 18. The normalized efficiency coefficient shall allow comparing dampers with different sizes.

$$\eta = \frac{\int_0^{x_{max}} F_{Loading}\, dx - \int_0^{x_{max}} F_{Unloading}\, dx}{\int_0^{x_{max}} F_{Loading}\, dx} \%$$ 18

The damping efficiency for the 3D printed TPU damper is shown in *Figure 36* and is compared with NBR, and SR dampers from the literature. All the values were obtained for cycles at 60% strain and frequency between 0.05 and 0.1 Hz. *Figure 36* shows that the 3D printed TPU damper has adequate damping efficiency of 15% of the applied energy. However, the 3D printed TPU damper has lower efficiency than the rubber dampers. The new 3D printed damper showed 50% of the SR damper and about 30% of the NBR damper. Improvement in damping efficiency is necessary to provide comparable performance to that of the other dampers.

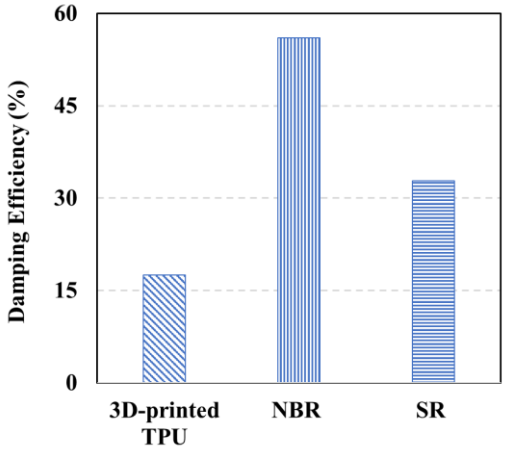

Figure 36 Damping efficiency of 3D printed TPU, NBR, and SR dampers

3.3.3 Finite Element Analysis

3.3.3.1 Material model coefficients

The uniaxial tension test data at 0.055 1/s rate of the R45 infill pattern was used for hyperelastic properties. Since the stable response of TPU will be dominant in cyclic applications it will be used for modeling throughout this work. Two different strain energy

density functions were used in this work. One used the stable response without inelastic effects to simulate the tests conducted on TPU specimens, while the other was for the stable response with inelastic effects to simulate the VED test.

A 3rd order Ogden strain energy function was used to simulate the TPU straight specimen. The coefficients of the fit are presented in *Table 6*. The fit is mathematically stable within the tested strain range with a root mean square error of 0.3. *Figure 37* shows the experimental stress-strain plotted with 3rd order Ogden fit of the test.

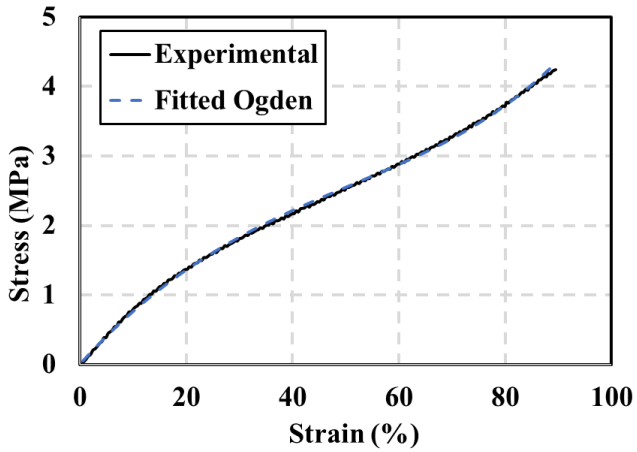

Figure 37 Experimental stress-strain vs. 3rd order Ogden fit

Table 6 Hyperelastic material model, Ogden N = 3, coefficients

	μ_i	α_i
1	-8.52	4.5
2	2.7	5.8
3	8.67	2.97

For simulating the VED, a 6th order reduced polynomial strain energy density function was used. The coefficients of the fit are presented in

Table 7. The fit is mathematically stable within the tested strain range with a root mean square error of 1.59. *Figure 38* shows the experimental stress-strain with a 6th order reduced polynomial fit of the test.

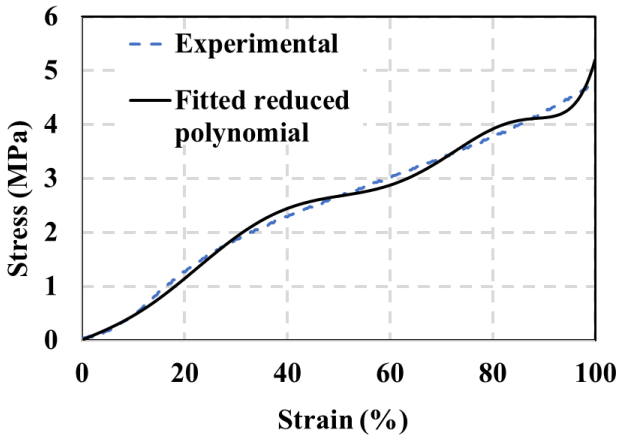

Figure 38 Experimental stress-strain vs. reduced polynomial fit

Table 7 Hyperelastic material model, Reduced polynomial N = 6, coefficients

i	C_{i0}
1	0.67
2	2.88
3	-5.36
4	4.61
5	-1.86
6	0.28

The Prony series parameters, $\bar{g}_i^p$ and τ, were identified by performing a curve fitting procedure on normalized stress relaxation tests. The normalized stress relaxation curve along with the Prony series fit of the test are shown in *Figure 39*. The fit was produced using a two-term Prony series model with a root mean square error of 0.54. The coefficients of the two-term Prony series are shown in *Table 8*.

Table 8 Prony series fit parameters

	$\bar{g}_i^p$ (Mpa)	τ_i (s)
1	0.26	0.44
2	0.12	24.56

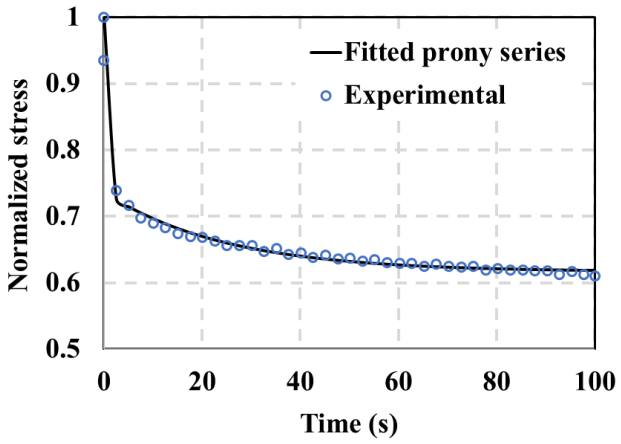

Figure 39 Normalized stress relaxation vs. Prony series fit

3.3.3.2 TPU specimen model

Figure 40 shows the experimental stable response and the stable response from the FE model both loaded using a strain rate of 0.055 1/s. The two responses show good agreement between them, with the simulated response achieving a slightly higher force and more nonlinear response. This can be explained by the equations of the Ogden strain energy function for uniaxial deformation. The equations define the lateral deformations as a fixed value of the longitudinal deformation as shown in Equation 9. This leads to a reduction in cross-sectional area that is not necessarily consistent with the experimental one. This change directly affects the strain energy density function and therefore the response of the modeled specimen will not be consistent with the experimental response of the specimen.

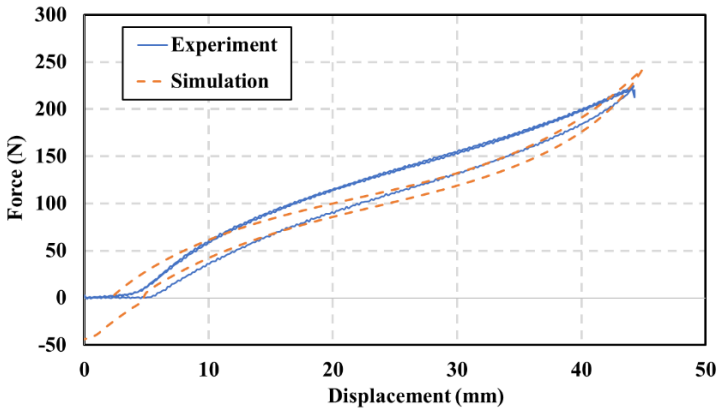

Figure 40 TPU specimen: experimental stable response at 0.055 (1/s) strain rate vs. model predictions

The point at which the unloading portion of the simulated response, shown in *Figure 40*, intersects the x-axis is considered to represent the onset of inelastic deformations. These inelastic deformations represented by the residual strain in the experimental response matched well with the simulation as seen in *Figure 40*. The force contours of TPU specimen in *Figure 41* shows two different time frames of the unloading process. An increase in force in the sections that are meshed with a larger seed (transition mesh) is observed when the specimen is transitioning to a lower displacement (*Figure 41*.b). This explains the unrealistic increase in compression force in the last potion of the unloading curve of the simulated response.

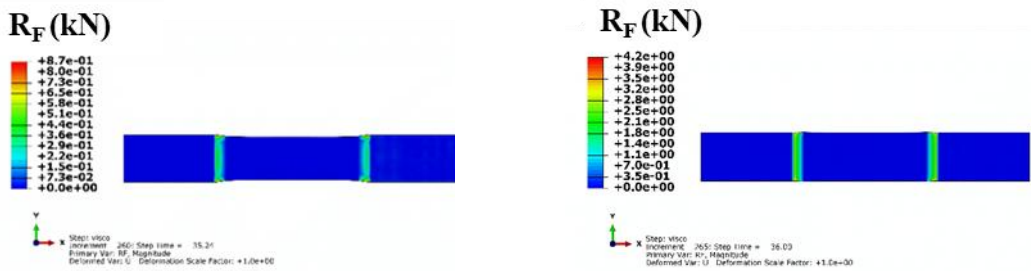

(a) (b)

Figure 41 Resultant force contours in TPU specimen during unloading showing an increase in force towards the end of the loading-unloading cycle (a) at time = 35.24 s (b) at time = 36 s (end of cycle)

Figure 42 shows contours of creep strain (CE) in the TPU specimen. CE is defined as the difference between the total strain and the elastic strain. The value of CE is 0.11 mm/mm in the gauge area which is in good agreement with the residual strains observed in *Figure 32* for R45 specimen. This further strengthens the claim that the point at which the compression force starts increasing in the model is the start of inelastic deformations or residual strain.

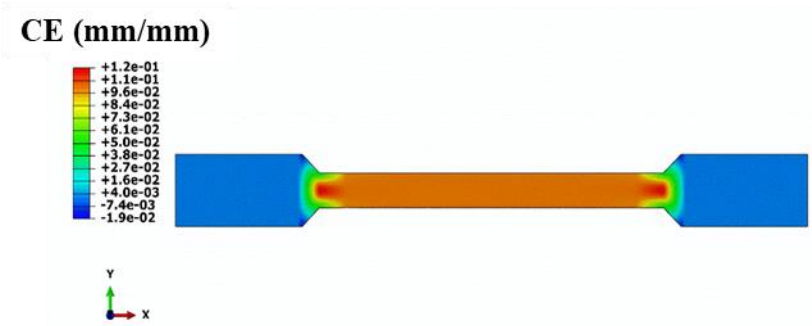

Figure 42 Creep strain contours of TPU specimen at full stretch showing the residual (inelastic) strain induced in the specimen due to loading-unloading

Figure 43 shows the contours of logarithmic or true strains in the TPU specimen at full stretch and towards the end of the unloading curve at time = 35.24 s. It is observed that the strain distribution within the gauge area is quite uniform in both cases. The maximum strain value at full stretch when calculated as an engineering strain would result in a value of 1.11 mm/mm which is close to the strain measured in the experiment (1 mm/mm) for an R45 specimen. *Figure 43*b shows that the logarithmic strain at the point where compression force start increasing in the transition mesh area is equal to 0.1 mm/mm. This value is in line with the CE value and confirms that this is the residual strain value.

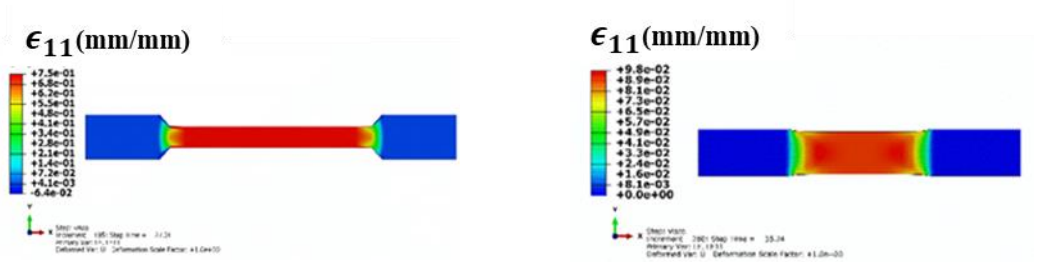

(a) (b)

Figure 43 Logarithmic (true) strain contours for TPU specimen showing (a) strain at maximum stretch (b) strain at end of loading-unloading cycle

The Ogden strain energy function fitted to the stable TPU response without inelastic effects was able to provide good results when simulating cyclic uniaxial tension tests of TPU specimen. It should be reiterated that the Ogden function was fitted based on uniaxial test results and was then used to simulate TPU under uniaxial tension.

3.3.3.3 Viscoelastic damper model

Figure 44 shows the experimental response of the damper at 1 mm amplitude and 3 mm amplitude with their finite element model predictions. The 5 mm amplitude was disregarded because of the adhesion issues in the experiment which makes the results unreliable. Since the experimental behavior does not show noticeable changes within the range of tested frequencies it is assumed that if a set of parameters of a model work in predicting the response at a certain frequency, then certainly it can predict the rest. Therefore, only one frequency, 0.5 Hz, was used in simulating the response of VED.

Figure 44 shows that the model at 1 mm amplitude does not match well with the experimental behavior. This can be attributed to the relatively higher strain at which both the hyperelastic and viscoelastic functions were determined at. On the other hand, the model prediction of the 3 mm amplitude provides a good match with the experimental

behavior. The slight differences might be caused by the absence of a damage function in the finite element model in addition to the use uniaxial response only in the material model without considering other modes of deformation.

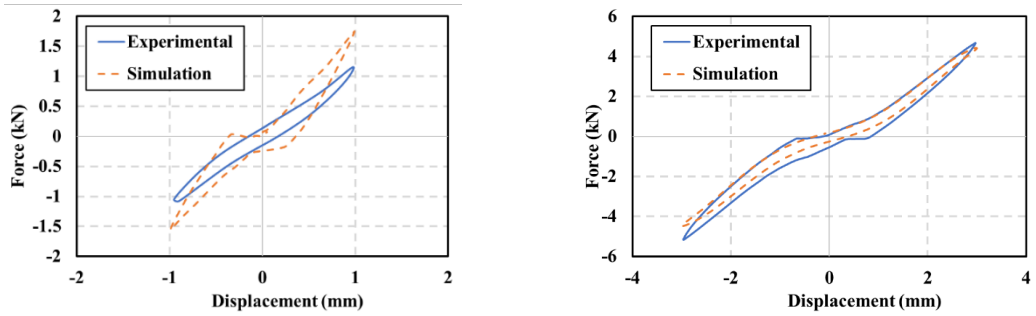

(a) (b)

Figure 44 VED: Experimental vs. Model Predictions at (a) 1 mm amplitude and (b) 3 mm amplitude

The creep strain (CE) contours and average values that resulted from the shear deformation at 3 mm amplitude are shown in *Figure 45*. The contours show that the creep strain distribution is uniform in the middle, and the extreme values (high and low) are located closer to the edges of TPU. This non-uniform distribution induces higher stresses at the extremities of the TPU block which can lead to failure such as the one seen in Figure 35.c The values of creep strain in TPU are averaged and shown in *Figure 45*.b for the first loading cycle. Interestingly, the highest creep strain value (0.158) is extremely close to the value of residual strain calculated from the experimental response (0.146).

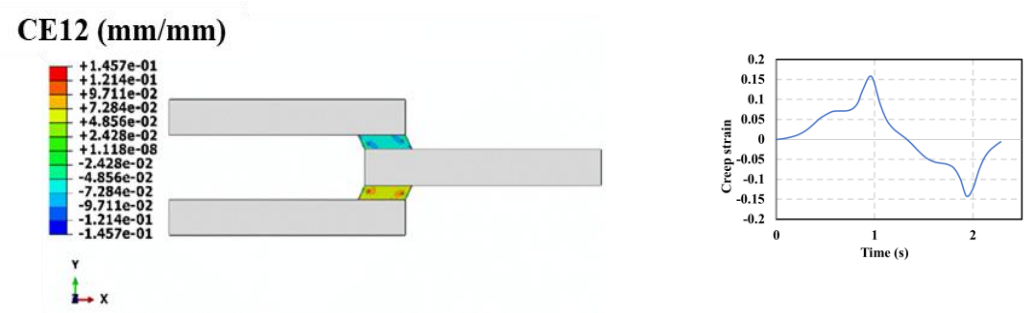

(a) (b)

Figure 45 Creep strain at 3 mm amplitude and 0.5 Hz frequency (a) contours (b) averaged values

Hence, the model correlates well with the experimental behavior at relatively higher strain ranges. It is, however, incapable of accurately modeling responses at a significantly lower strain value than what was used in tests to determine the parameters of the model. Also, the reduced polynomial function fitted to the stable TPU response with inelastic effects was able to simulate the behavior of VED and creep strain values under shear deformations.

In this chapter 3D printed TPU produced via FDM was mechanically characterized and the effect of loading rate and infill pattern of specimens was examined. It was found that infill pattern has no impact on the tensile behavior of 3D printed TPU specimens and only the density of the part matters. On the other hand, increasing the loading rate leads to an increase in mechanical response but once the response stabilizes the rate effect becomes negligible. 3D printed viscoelastic dampers with rectilinear infill pattern oriented at 45 degrees were produced and tested at different strain amplitudes and frequencies. The 3D printed viscoelastic damper showed a response independent of strain amplitude and frequency at the tested range. The results of damping efficiency showed that 3D printed TPU damper has lower efficiency when compared with rubber dampers. A computational

model of the VED was developed using the finite element method. A visco-hyperelastic material model was used to simulate the behavior of the 3D printed TPU. The results of the simulation showed a good agreement with experimental results.

Chapter 4: **Mechanically Interlocked Viscoelastic Damper**

4.1 Design concept

The goal of the study is to investigate the effect of mechanical interlocking on the energy dissipation of a VED that contains 3D printed elastomeric material. The device consists of rigid and soft phases that are mechanically interlocked without chemical adhesion or bond as shown in *Figure 46*. The device is loaded from the center plate in the horizontal direction like conventional VEDs. The jigsaw-like interlocking pattern design chosen for this study follows the design presented in the work of Malik et al. [79]. This design will cause an interlock between the rigid and soft materials. The rounded features of the jigsaw help in minimizing premature failure due to local stress concentrations in the rigid material, thus presenting global failure due to applied loads. The geometrical features of the interlocking pattern have a dominant role in the overall performance of the device. The parameters that characterize the jigsaw interlocking pattern can be studied by isolating an individual cell of the repeating pattern as shown in *Figure 46*. The parameters are the radius (R), the angle between centers of adjacent jigsaw joints (θ), and the thickness of the interlocking pattern (t).

The ability to 3D print the energy dissipating viscoelastic part allows for easy replaceability of that part after it experiences a destructive event such as earthquakes. Since the mechanical properties of TPU decrease as it approaches the stable response, the ease of replaceability can facilitates one-time use of 3D printed TPU used as an energy dissipating part in an interlocked VED. Moreover, AM expedites the response time needed to produce and retrofit a structure after the occurrence of a disruptive event which

leads to a more resilient structural system. The use of an interlocking system allows more control over the response of the damping device through changing the geometrical parameters that govern the interlocking system. It also eliminates the need for chemical adhesion between the two phases of the device. The combination of AM and an interlocking system in the proposed damping device provides the ability to have a multi-functional passive damping device.

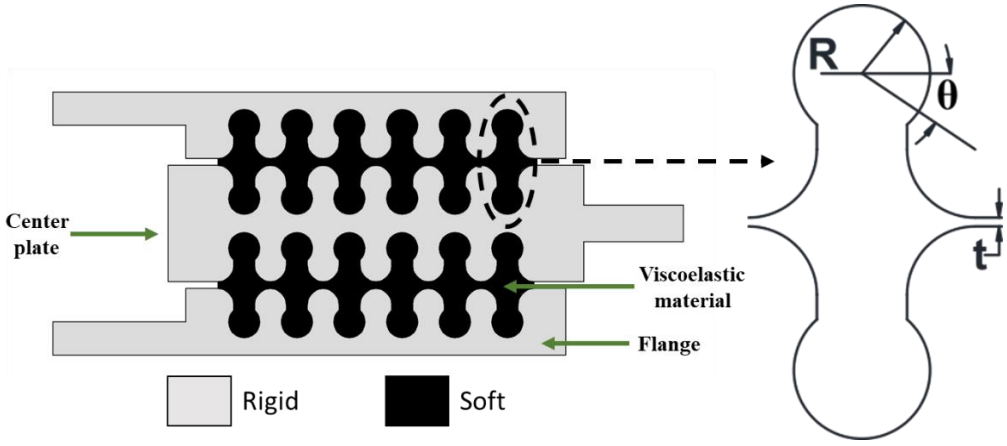

Figure 46. Components of proposed MIVED and geometrical parameters of jigsaw pattern

The imposed displacements on the MIVED causes the development of contact forces (CF) due to the soft phase material pushing against the rigid phase material as seen in *Figure 47*. The center plate stays in place because of the symmetry of the contact forces acting on it from both sides. The resultant of the contact forces (R_{CF}) causes the flanges to deform in two modes: Mode I and Mode II. The occurrence of a specific mode depends on the boundary conditions at the flanges which are a result of the stiffnesses of the connection, the soft phase, and the rigid phase. Mode I represent a device with a roller at the flange that suppresses displacements in the horizontal direction and two springs that

limit displacement in the vertical direction. These boundary conditions allow the device to rotate in a rigid body motion. Whereas Mode II corresponds to a device with a fixed boundary condition that restrains the device from all translations and rotations. The boundary conditions in this mode causes the rigid phase to rotate as a result of the out-of-plane bending moment (M_{RCF}) generated from the eccentricity of the applied contact forces by the soft phase. Due to this rotation, the device in both modes is allowed to reach high levels of displacement in the horizontal direction without failure in the soft phase. Additionally, both modes of operation allow for multiple modes of deformation such as uniaxial, biaxial and shear deformations in the soft phase through rotation of the rigid phase. Mode II, however, undergoes additional deformation in the rigid phase itself in the form of buckling due to the bending moment (M_{RCF}).

The multiple modes of deformation in the soft phase makes the single-state normalization of displacements of the TPU part into a measure like strain not possible. Therefore, the design of the device is dependent on how much it would be displaced during load application. This is contrary to conventional VEDs where only shear deformations take place and shear strain is used as a normalized displacement measure.

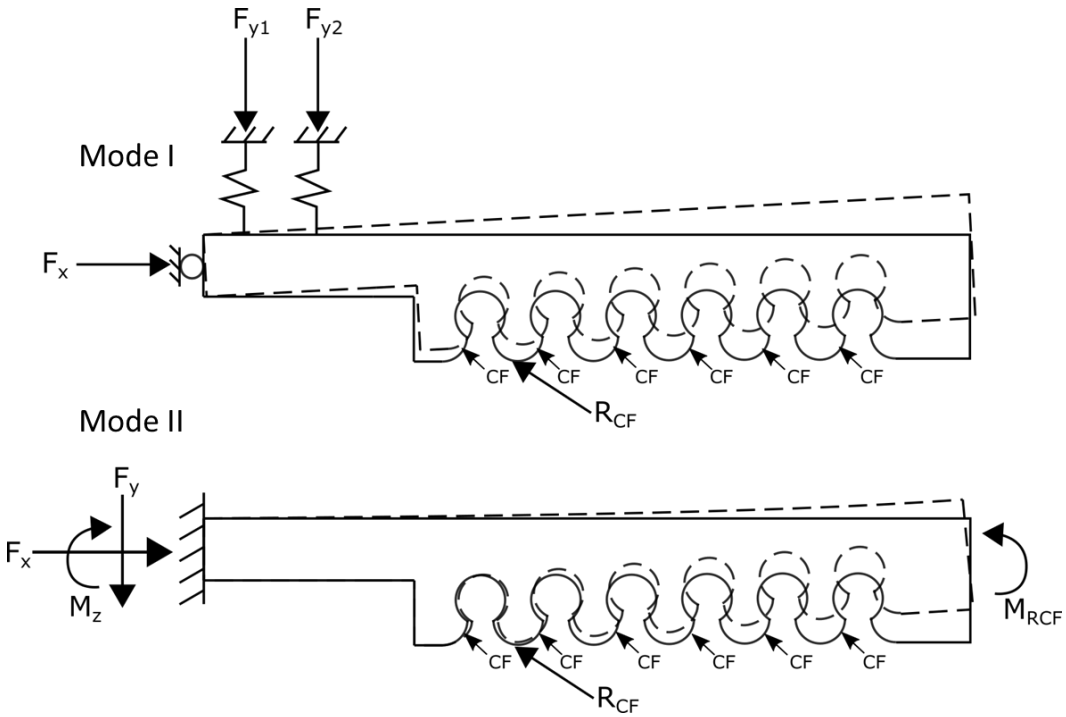

Figure 47. Contact forces acting on MIVED

4.2 Fabrication

Two devices were fabricated, MIVED-1 and MIVED-2, to demonstrate the two modes of operation of MIVED modes I and II, respectively. The choice of material in each device influenced the mode it operates in. The same dimensions were used for both devices. A schematic of the components of the tested devices and their dimensions is shown in *Figure 48*. The thickness or the out-of-plane dimension is 58 mm. Both devices were assembled by inserting the soft phase into the rigid phase along the out-of-plane direction of the damper.

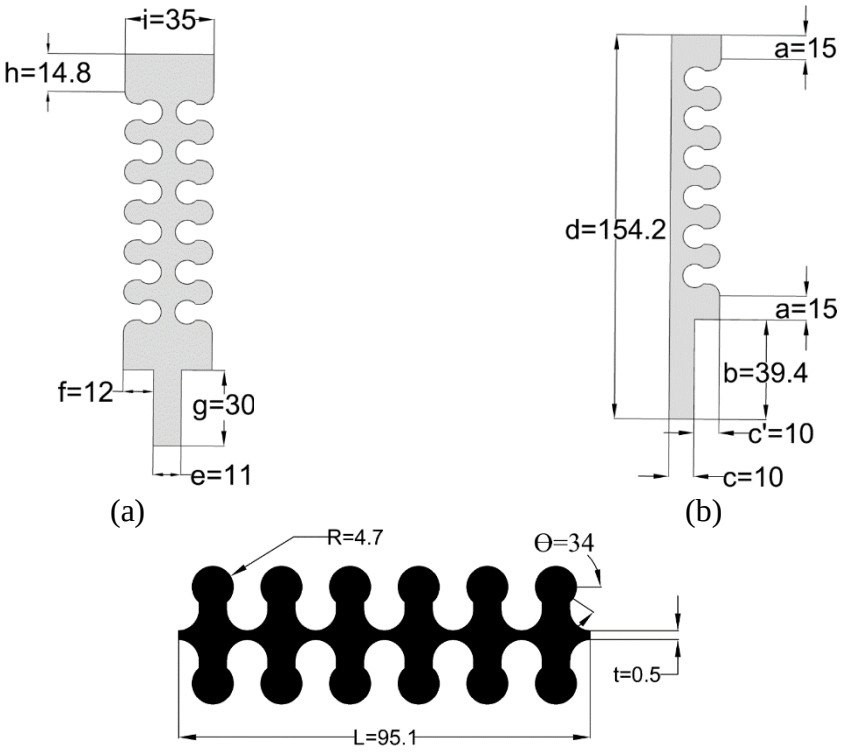

Figure 48. Components of MIVED device and dimensions (a) Center plate (b) Flange (c) TPU part. All dimensions in mm.

4.2.1 MIVED-1

The soft phase of the MIVED is made from TPU which is printed using the same printing parameters described in *Table 1*. The rigid phase of the device was fabricated from grade 1018 steel using conventional machining methods. *Figure 49* shows the soft phase of the device and the final assembly with soft and rigid phases.

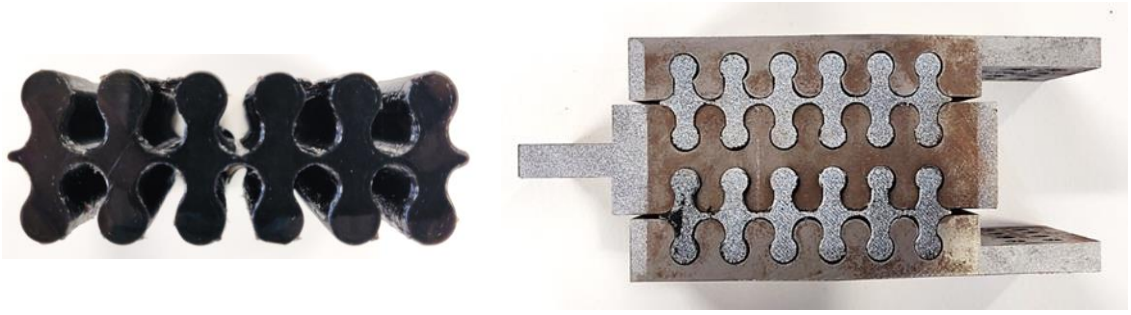

(a) (b)

Figure 49 (a) 3D printed interlocked TPU part (b) MIVED-1

4.2.2 MIVED-2

In this device the rigid phase was fabricated using 3D printed Nylon reinforced with chopped carbon fiber. This proprietary material to Markforged® is called onyx. Mark Two™ 3D printer with FDM technology was used to print the onyx material. Continuous 3D printed fiberglass was used to reinforce the onyx to enhance the flexural rigidity of the rigid phase. This was possible because the Mark Two™ printer employs dual extrusion technology to print thermoplastics and continuous reinforcement as shown in *Figure 50*a. The print was done with 4 roof and floor layers, 2 wall layers, and a triangular fill with 55% infill percentage. The final fiber volume fraction of all rigid phase components is 45%. The continuous reinforcement is coated with a Nylon 6 material that enables extrusion and adhesion to the matrix material it is being extruded onto. The flexural properties of the onyx and fiber glass as provided by the manufacturer are provided in *Table 9*. The fabrication of MIVED-2 and the rigid phase of it are shown in *Figure 50*.

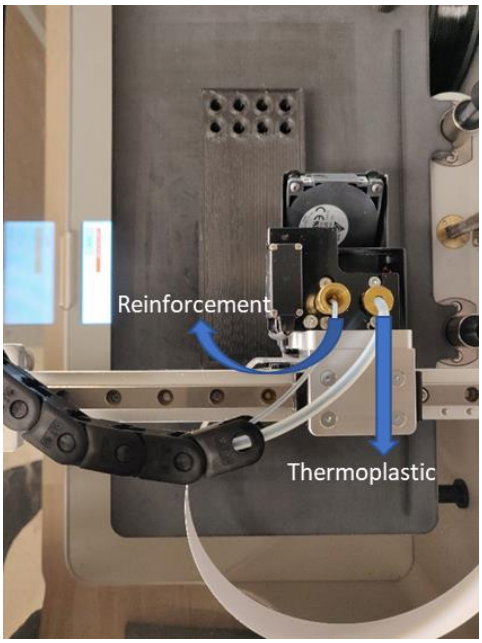

(a)

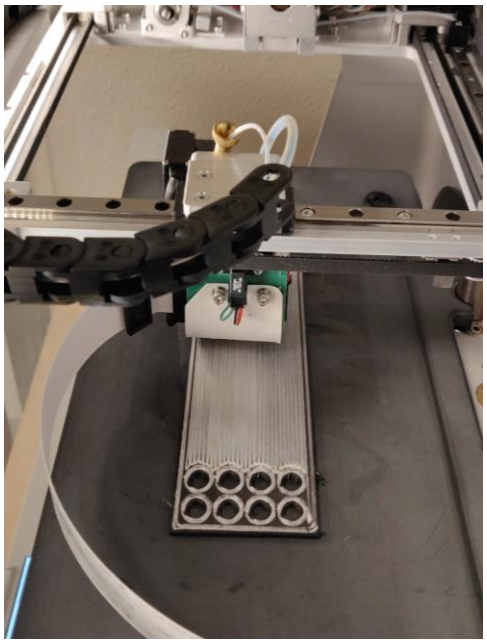

(b)

(c)

Figure 50 MIVED fabrication (a) dual extrusion in 3D printer (b) Onyx reinforced with continuous fiberglass reinforcement (c) 3D printed rigid phase of MIVED-2

Table 9 Flexural properties of 3D printed onyx and fiberglass

Flexural property \ Material	Onyx	Fiberglass
Strength (MPa)	71	200
Modulus (GPa)	3	22
Strain at break (%)	-	1.1

As for the soft phase soft polymeric materials are incorporated within the matrix of 3D printed TPU through means of injection as shown in *Figure 51*a. The middle portion

between every two opposing interlocks of the soft phase was sliced using 0% infill percentage with only a floor layer at the bottom. The resulting cavities are then filled with Silicone Rubber (SR) which was degassed prior to injection. Also, the entire TPU part was vibrated throughout the injection process to eliminate air voids. The material used was Mold Max™ 40 which is a 40A shore hardness silicon rubber material by Smooth On, Inc. (Easton, PA). The pot life of SR is 45 minutes, and the cure time is 24 hours. The tensile strength, modulus, and elongation at break of SR are 3.8 MPa, 1.31 MPa, and 250% respectively. The final form of the soft phase is shown in *Figure 51*b. The damping and stiffness in such a composite can be considered tunable as constituent materials can be changed and volume fractions can be controlled to produce specific properties.

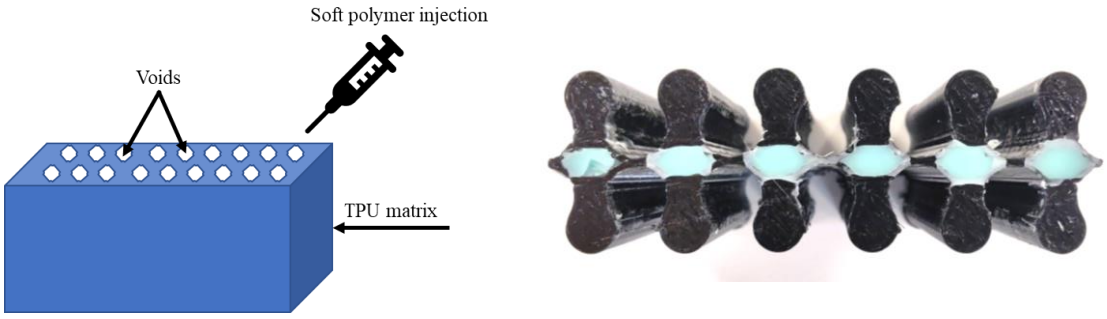

(a) (b)

Figure 51 (a) Injection process (b) 3D printed TPU injected with silicone rubber (SR)

4.3 Experimental methods

4.3.1 MIVEDs testing

The test setup, shown in *Figure 52*, was fabricated to test the MIVED. The flanges of the MIVED are bolted to steel single-angle connections which in turn are bolted to steel plates that are attached to the UTM using a pin connection at the top and bottom.

The same loading protocol as VED shown in *Figure 22* and summarized in *Table 4* was used for MIVED. The loading history covers displacement amplitudes ranging from 1.0 mm to 5.0 mm and frequency range between 0.05 Hz and 0.5 Hz. This loading protocol enables evaluating the device in different vibrational scenarios.

Despite using the same single-angle all-bolted connection in all the devices, the resulting modes are not the same. This is because the boundary conditions are a result of the stiffnesses of the connection, the soft phase, and the rigid phase. This combination of stiffnesses govern the boundary conditions through controlling the applied contact forces. If the rigid phase is of very high stiffness or flexural rigidity then high contact forces are expected and, therefore, the semi-flexible connection allows for rigid body rotation. On the other hand, a rigid phase with more flexibility results in lower contact forces and the connection becomes fixed.

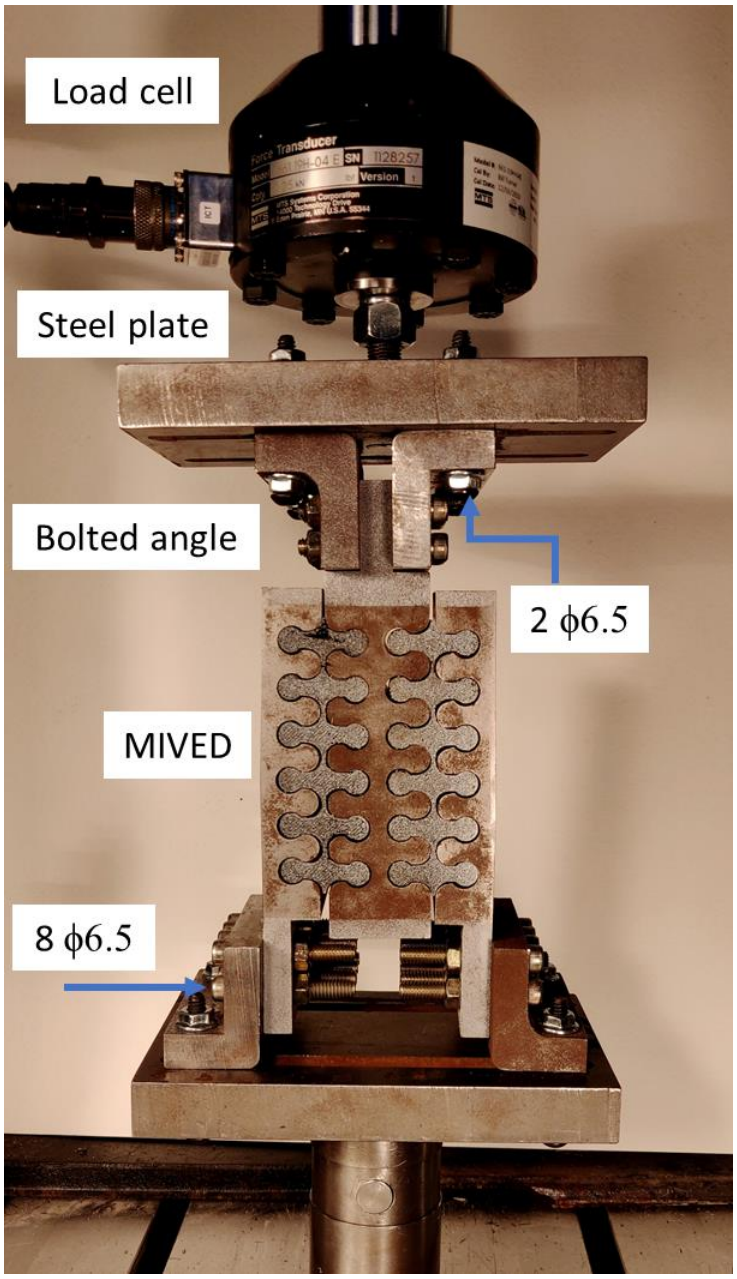

Figure 52. MIVED test setup. Bolts dimension in mm.

Furthermore, the device was tested at a higher frequency range using the loading protocol shown in *Figure 53*. The range of frequencies varied from 0.5 Hz up to 10 Hz at an amplitude of 5 mm with 10 cycles per frequency. The test was conducted using the same UTM with a higher sampling rate of 2048 Hz.

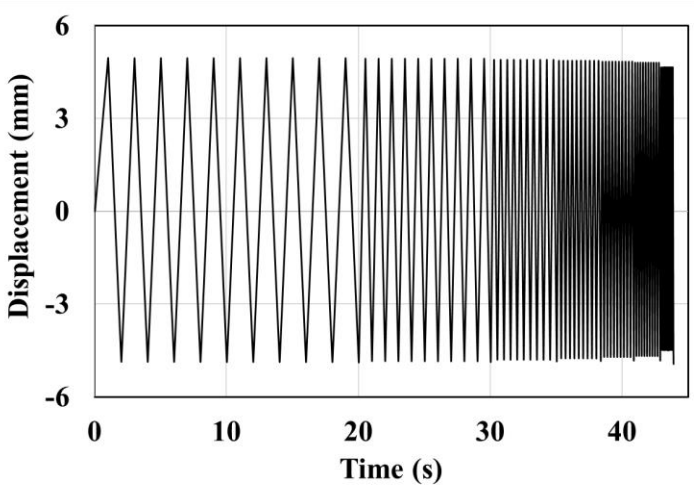

Figure 53 Higher frequency loading protocol

4.4 Computational methods

A 2D model of MIVED-1 was analyzed using the finite element method to further explore the effect of geometrical and mechanical factors on the performance of the device. The behavior of the model is first compared to experimental behavior for validation. Then a parametric study was conducted on the geometry of the jigsaw pattern and the viscoelastic properties of the soft phase to understand their effects on the damping efficiency of the device.

4.4.1 Material model

The visco-hyperelastic material model described in Chapter 3 is used to simulate the behavior of MIVED-1. The reduced polynomial strain energy function described by Equation (9) is used for the hyperelastic part.

4.4.2 Model details

A 2D FE model was developed to simulate the response of MIVED-1. A 4-node bilinear plane strain quadrilateral, hybrid, constant pressure element (CPE4H) was used for TPU. As for the steel parts, a 4-node bilinear plane strain quadrilateral (CPE4) was used. The minimum mesh size for the TPU was 0.65 mm, whereas for the flanges and the center plate the mesh near the interface was refined to a minimum of 1.25 mm. The global mesh size for the single-angle connection was 4.8 mm. Surface-to-surface contact was used assuming no friction between interfaces due to the smooth surface of the steel part. Also, in an interlocking geometry between rigid and soft interfaces it was shown that the friction coefficient has practically little effect on the structural performance of the assembly [94]. The contact between the soft and rigid interfaces was modeled using a penalty method that approximates a hard contact. In this method, the contact forces are proportional to the penetration distance as opposed to the hard contact method where a zero-penetration condition is applied. *Figure 54* shows the FE model developed for the device.

All the simulations were run under quasi-static cyclic loading conditions using ABAQUS® implicit solver. The load is applied on the center plate in a displacement-controlled mode using the same ramped loading scheme of the experimental part. Since multiple modes of deformation are triggered in the TPU part, it was not possible to achieve a normalized displacement value (strain) for all models. Therefore, the maximum imposed displacement used was 5.0 mm displacement for all models. The boundary conditions of the experiment were simulated by fixing the flanges to the single-angle

connection which in turn is connected to a roller to prevent displacements in x-direction. These conditions allow the device to rotate through the lateral rigid body motion of the flanges as observed in the experiment. However, there is limited restriction on the amount of lateral movement that the flanges of the device are allowed. Therefore, to control the rotation of the device, spring elements were attached to the flange leg of the connection to add restraints in the y-direction as shown in *Figure 54*.b. Two spring elements were used on each side with stiffness $k_s = 3E^5$ N/mm in the y-direction to mimic the behavior of the flexible single-angle connection. This approach has been used in the literature to model the components of angle connections [95,96]. Artificial geometrical imperfections were introduced to the soft part of the model in order to simulate the gaps between the soft and rigid parts in the experiment and the associated reduction in contact area. The imperfections were modeled by introducing a reduction factor of 0.1xR to the interlocking geometry.

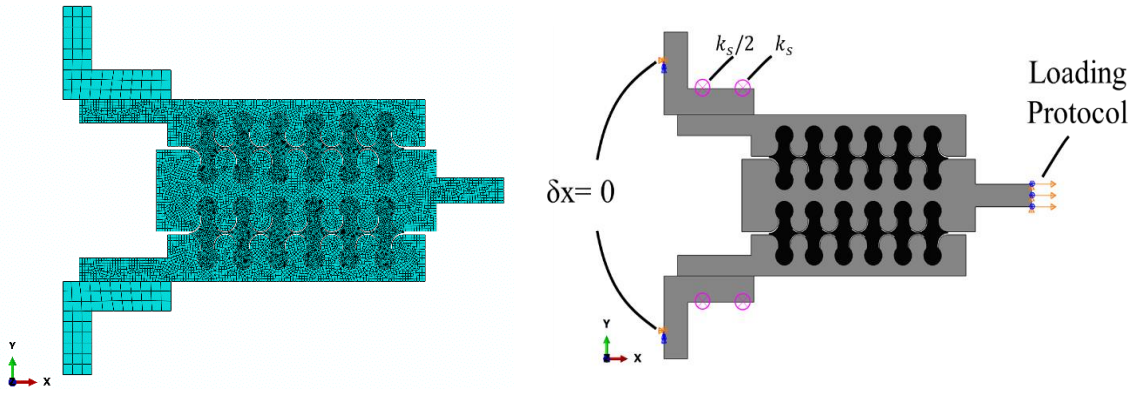

(a) (b)

Figure 54. Numerical model of MIVED (a) mesh details (b) boundary conditions

4.4.3 Parametric study

A parametric study is conducted to examine the effect of various geometrical parameters on the energy dissipation of MIVED. The parameters for this study are thickness of TPU (t), radius of interlocks (R), and angle between successive interlocks (θ). Each parameter impacts the performance of the device in a certain way. The change in thickness increase the amount of deformed TPU which directly affects the energy dissipation of the device. The radius and angle are expected to influence the interlock performance of the device and the development of stress concentrations within the interlocking geometry.

Also, the viscoelastic material parameters of the soft phase will be varied to study the time-dependent effects on the response of the damper. The hyperelastic time-independent parameters, however, will remain unchanged throughout the study because they only affect the instant time-independent response with no implications on the energy dissipation. Therefore, for a given hyperelastic material, the application of different time-dependent properties will produce different modulus, maximum force, and energy dissipation.

The energy dissipation efficiency is compared using the damping efficiency coefficient (η), described by Equation 18, representing the ratio of the dissipated energy to the applied energy. The normalized efficiency coefficient allows comparing dampers with different geometric and material parameters.

4.5 Results and discussion

4.5.1 MIVED-1

Figure 55 shows the hysteresis response of the tested device at 0.5 Hz frequency for different amplitudes of applied displacements. The figure shows that the device response is highly nonlinear because of the TPU response, interlocking nature of the device, and the gaps between the soft and rigid interfaces. It can be observed that the response of the device is not symmetrical in tension “Pull” and compression “Push”, denoted by A and C respectively in *Figure 55*. In both pull and push motions it was observed that the segments of the TPU part that connect the interlocks together start pushing the flanges outwards as they deform and become in contact with the steel. This caused the device to be stiffer in compression since it is being pushed towards the angle connection, which restrains the lateral movement of the flanges. Whereas in tension it is being pulled away from the connection and the flanges are free to rotate. This causes an increase in the device stiffness in the push direction leading to higher forces than in the pull direction. It was also observed that the change in amplitude affects the tilt of the response or the stiffness of the device in the push direction but not in the pull. If the flanges of the device were adhered to the TPU then the push and pull behaviors would not have been observed and the device would behave as a conventional VED.

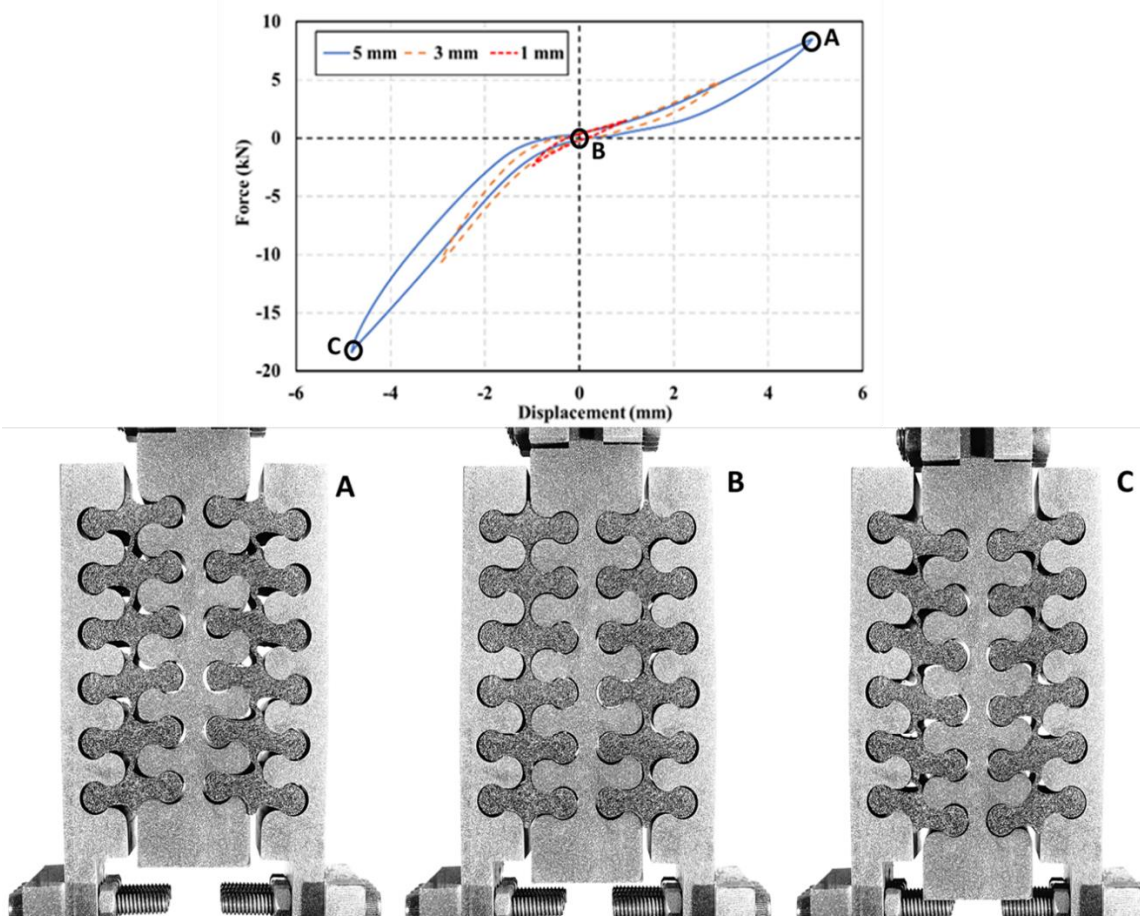

Figure 55. MIVED test results showing push and pull movements

*Figure 56.*a through *Figure 56.*c show that the stiffness of the device is not significantly affected by the change in frequency at this low frequency range. It can be noticed that the response of the device at 1 mm amplitude is slightly different than the rest. The reason is the gap between rigid and soft parts in the case of 1 mm amplitude is almost half the imposed amplitude which does not help in developing the full behavior of the device seen at 3 mm and 5 mm amplitudes.

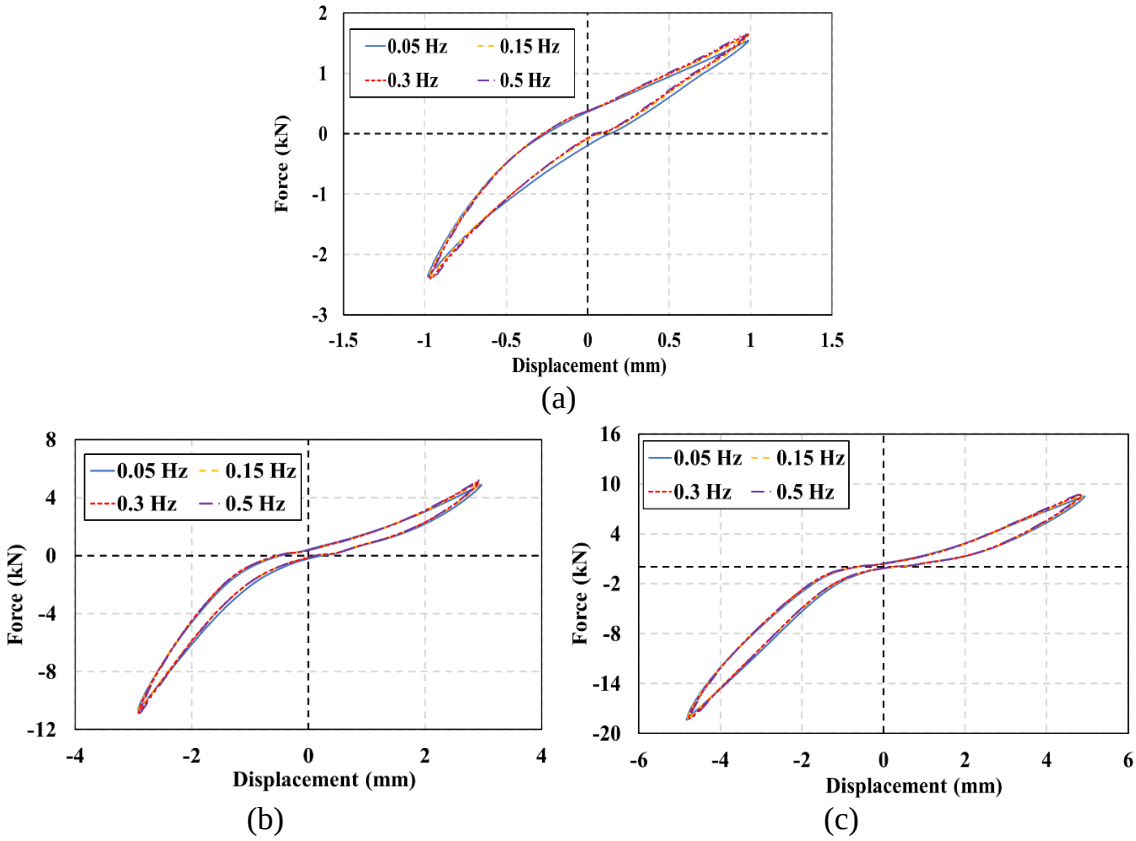

Figure 56. MIVED test results at (a) 1 mm (b) 3 mm (c) 5 mm

Due to the high stiffness and bending rigidity of the rigid phase the angle connection develops boundary conditions equivalent to mode I of the device. The rigid body rotations of the flanges in mode I are allowed by the semi-rigid single-angle all-bolted connection with only two bolts at the outstanding leg. This connection allows for load eccentricity to impose a flexural deformation at the outstanding leg in the form of rotation about the lower end of the angle [97,98].

To further explore the effect of the pull and push movements on the response of the device, DIC was used to track the movement of the flanges and center plate as the device is being loaded. Facet points 2 and 3 (FP2 and FP3), shown in *Figure 57*.a, were tracked and the displacements in the longitudinal and transverse directions were recorded. *Figure*

57.b shows the force of the device and the X and Y displacements of FP2 and FP3 all plotted against time for a 0.5 Hz, 5 mm loading cycle. The first peak represents the pull motion while the peak after represents the push motion. The displacements of the flange (FP2) indicate that the lateral and longitudinal displacements are increased in the pull direction resulting in lower maximum forces. On the other hand, loading the device in the push direction is associated with lower displacement and higher forces.

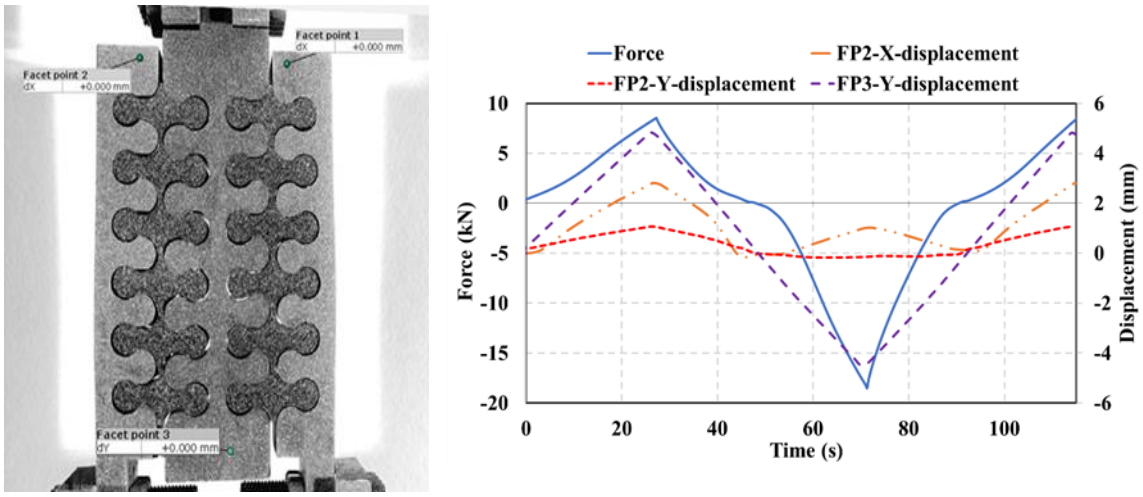

(a) (b)

Figure 57. Force and displacements of MIVED (a) Facet points locations (b) force, lateral displacement, and longitudinal displacement during one loading cycle with amplitude 5 mm at 0.5 Hz

Figure 58 shows the results of MIVED-1 tested at a range of higher frequencies 0.5-10 Hz. As the frequency increased the servo hydraulic testing machine was not able to reach the 5 mm amplitude value. This is evident from *Figure 58* as lower frequency loading of MIVED-1 resulted in a higher force. Nevertheless, the stiffness of the response clearly increases in pull and decreases in push as the loading frequency increases. It appears that MIVED-1 in push manipulates the material response through the change in rate enforced by the device. This makes MIVED-1 stiffer in push at lower frequency loadings.

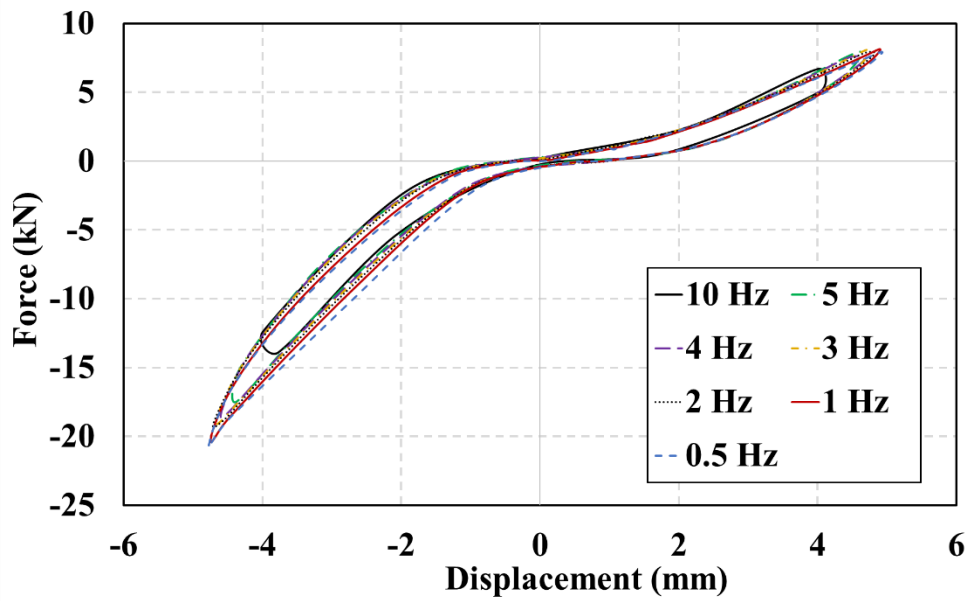

Figure 58 MIVED at higher frequencies

The coefficients for the viscoelastic and hyperelastic material model of the TPU were obtained by fitting the experimental data as was shown in chapter 3. The Prony series parameters and the 6^{th} order reduced polynomial strain energy function parameters are shown in *Table 8* and *Table 7*, respectively.

The results of the FE model of the reference geometry are compared with the experimental results for validation. The experimental and numerical force-displacement curves of the reference device are shown in *Figure 59* for applied displacement with 5 mm amplitude at 0.5 Hz frequency. The results show relatively good agreement between the predictive model and the experiment. *Table 10* shows a comparison of maximum force in pull and push and the total energy dissipation between the experiment and the numerical model. The numerical force values are fairly close to the experimental values (± 10% error), while the energy dissipation values are 23% lower than the experimental value. The differences between the two curves can be explained through multiple reasons. First, the

artificial imperfections introduced in the simulation do not mimic the actual gaps between TPU and steel in the experiment due to randomness and machine induced errors during fabricating the steel and TPU parts. Second, the quasi-static 2D model does not account for the inertial effects associated with cyclic loading and 3D modes of deformation such as biaxial and planar shear. However, the FE model can still capture the general deformation response of MIVED-1 as can be observed when comparing the simulated behavior to the experimental one in *Figure 60*.

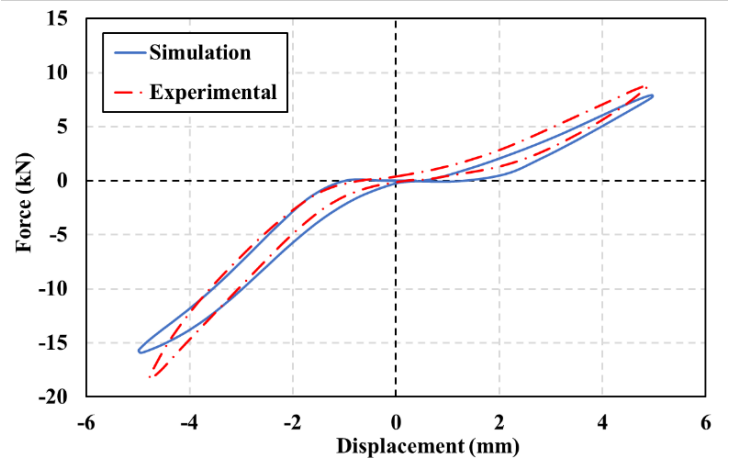

Figure 59. Experimental vs. Numerical results for 5 mm amplitude at 0.5 Hz

Table 10 Numerical vs. experimental results for the mechanical response of MIVED-1

	Simulation	Experiment	Error (%)
ED (N.mm)[a]	1.94 x 10^4	1.49 x 10^4	23.1
F_{push} (kN)[b]	15.91	18.24	12.8
F_{pull} (kN)[c]	7.92	8.79	9.80

[a] Energy dissipation [b] Maximum push force [c] Minimum pull force

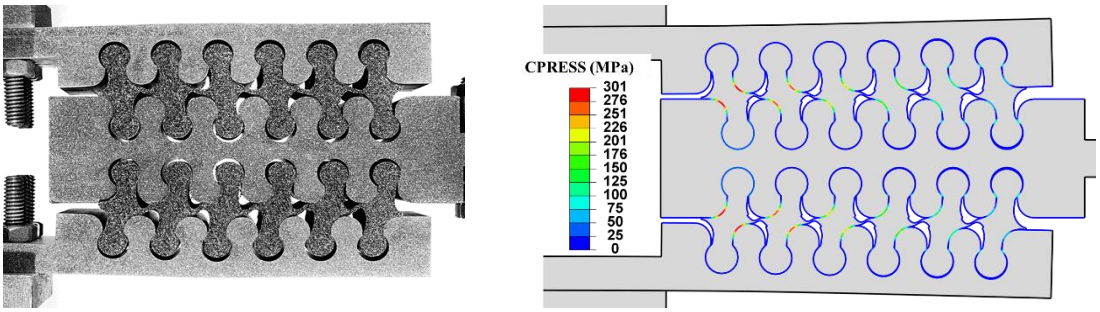

(a) (b)

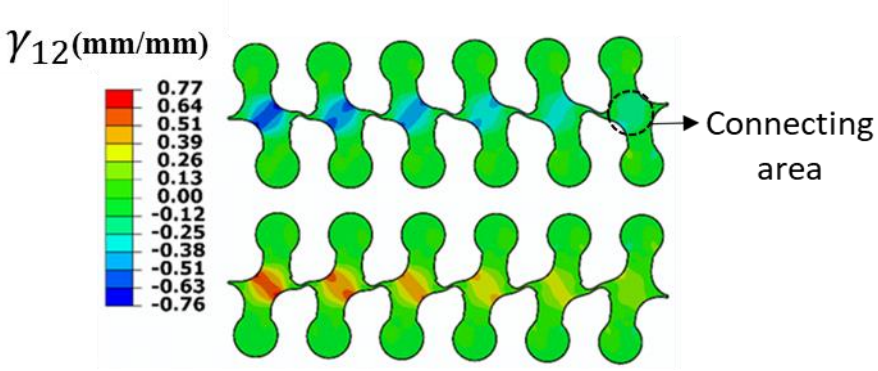

(c)

Figure 60. Pull behavior in MIVED at 5 mm amplitude and 0.5 Hz frequency (a) experimental behavior (b) pressure in TPU part due to contact with steel part (c) shear strain in TPU part

*Figure 60.*c shows that the deformation of TPU part in the FE model reasonably depicts the deformations observed experimentally of the TPU part (*Figure 60.*a). In addition, *Figure 60.*b shows the contact pressure developed in the numerical model between rigid and soft interfaces, which provides a good explanation of the experimental behavior of the device. The simulation shows that the TPU is pushing the side flanges laterally away from the center due to the development of contact pressure in the jigsaw interlocks. The contact pressure on the center plate is cancelled out by the equal and opposite pressure development on the two sides. Moreover, the maximum strain in the TPU

part was caused by shear (115%) does not reach the failure strain value (1040%) as measured by Reppel [99]. This is an indication that the TPU, in the 3D printed mechanical interlocking form, can withstand the applied stresses.

The simulations highlighted the different strain states that the TPU experience during pull and push. The strain states of pull and push, as shown in *Figure 61*, are axial strain in x and y directions (both tension and compression), in addition to shear strains. It is observed that the two TPU parts, top and bottom, in the damper undergo the same strains in all states but in opposite directions. Tensile and compressive strains are a direct consequence of the contact forces the TPU exerts on the rigid phase or steel. Tension is dominant in the y-direction, whereas compression is dominant in the x-direction. A combination of loading in x and y directions is what determines the amount of rotation the angle connection or the flange undergoes. The addition of compressive test data of TPU will help in improving the accuracy of the model. However, in this work the compression values that the TPU is experiencing are relatively low and, therefore, the effect on the quality of the results is not significant. Nevertheless, at higher compressive strains (The simulation also showed that interlocks closer to the angle connection are strained more in push than the ones that are farther away, and vice versa in pull where interlocks farther away from the angle connection are strained more. On the other hand, the segments between successive interlocks do not experience high strains regardless of the direction.

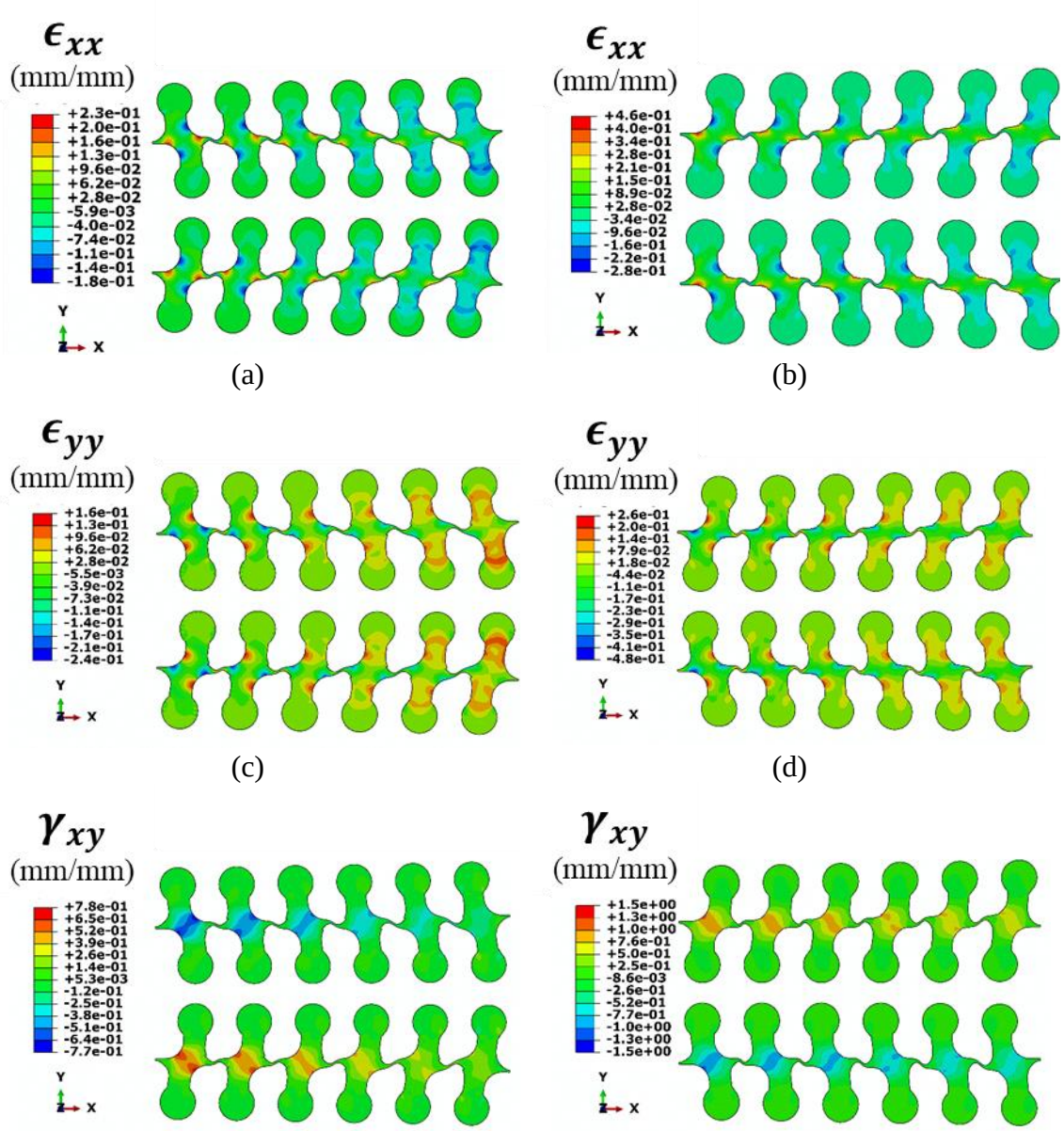

Figure 61 True strain states of MIVED (a) ϵ_{xx} pull (b) ϵ_{xx} push (c) ϵ_{yy} pull (d) ϵ_{yy} push (e) γ_{xy} pull (f) γ_{xy} push

Comparison between the energy dissipation efficiency (η) for the examined geometrical parameters: thickness of TPU (t), radius of interlocks (R), and angle between successive interlocks (θ) can be seen in *Figure 62*. The reference model which was experimentally tested is singled out in *Figure 62* by using a different pattern to the bar that

represent its energy efficiency. *Figure 62*.a shows that the damping efficiency is higher for interlocks with lower radius. Moreover, there seems to be an optimum value for the radius that produces higher efficiency which is 4 mm in this case. The radius of the TPU part is proportional to the connecting area of the part, shown in *Figure 60*.c, which is strained the most. Therefore, a lower radius with a smaller connecting area exhibits higher strains which makes it more efficient. Conversely, *Figure 62*.b shows that an increase in angle causes an increase in efficiency. In a similar manner, a higher interlocking angle in a TPU part leads to smaller connecting area, which in turn leads to higher strains and, therefore, higher efficiency. On the other hand, *Figure 62*.c demonstrates that the change in efficiency due to increase in thickness is not very pronounced and can be considered negligible. As the TPU thickness increases, lower strains are exhibited by the TPU part because they deform less when compared to a part with a lower thickness. Nevertheless, the efficiency lost due to reduction in strain is compensated by the increase in thickness, which increases the connecting area, and consequently maintains similar efficiency levels.

In summary, the variation of the geometric patterns in the study revealed that higher strains in the TPU are associated with higher efficiency levels. Since the same displacement was imposed on all the models, the area of the TPU part, especially that of the connecting segments which are strained the most, controlled the strain levels. Therefore, the parameters that can provide the higher strains would be the most efficient. Thickness does not contribute to the efficiency of the damper; therefore, it can be disregarded when considering the geometrical parameters of the device. Nevertheless, there is an advantage in using a higher thickness as it reduces the strains while maintaining the same efficiency

levels. Moreover, increasing the thickness will yield lower stress levels in the device which reduces the likelihood of the TPU part to fail.

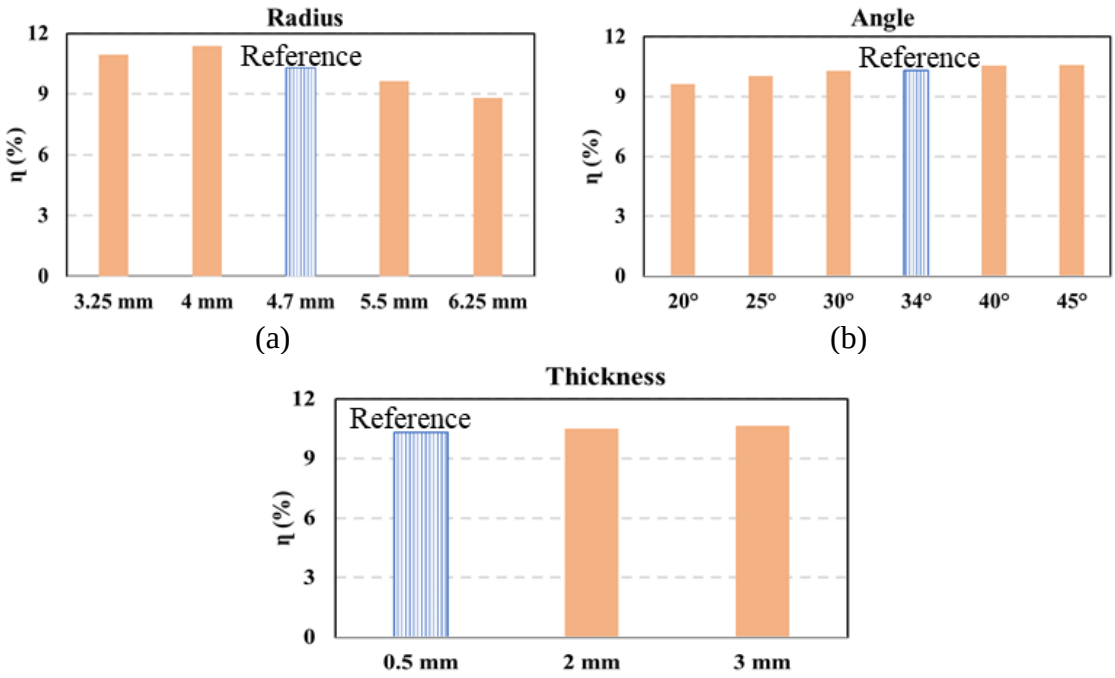

Figure 62. Effect of geometrical parameters on the damping efficiency of MIVED (a) Radius (b) Angle (c) Thickness

The energy dissipation efficiency was also checked for different viscoelastic material properties while maintaining the same hyperelastic material properties shown in *Table 7*. The different materials used in this study are summarized in *Table 11* in terms of their viscoelastic properties in the form of a Prony series expansion.

Table 11 Prony series coefficients of materials used in parametric study

	$\bar{g}_1^p$ (MPa)	τ_1 (s)	$\bar{g}_2^p$ (MPa)	τ_2 (s)	$\bar{g}_3^p$ (MPa)	τ_3 (s)	$\bar{g}_4^p$ (MPa)	τ_4 (s)
Material A	0.008	0.04	-0.108	1.17	0.0715	73.08	0.858	1.85
Material B	0.068	0.001	0.142	7.50	-0.008	692.64	0.568	0.61
Material C	0.132	0.03	0.131	0.64	0.015	6.04	0.083	6.09
Material D	0.143	0.001	0.171	1.22	0.033	118.90	0.156	17.24

The simulations are done at a fixed amplitude and frequency of 5 mm and 0.5 Hz, respectively. *Table 12* shows that the maximum force as well as the damping efficiency vary significantly across the different materials. Since the hyperelastic properties remained unchanged it means that only the viscoelastic properties contributed to the variance in material response. It appears from *Figure 63* that the stress relaxation curves that represent the viscoelastic behavior differ in both the amount of drop in normalized stress and the rate of the drop. In terms of drop in normalized stress, material A showed the highest drop followed by materials B and D, and lastly material C. It can be noticed that material B with the highest efficiency has the same ultimate drop as material D with the lowest efficiency. Therefore, no clear correlation can be deduced between ultimate drop and the damping efficiency. On the other hand, the rate of the drop can be divided into short time (0-1 s) and long time (0-100 s) response. In long time it can be observed that material A has a higher change in rate over a longer period followed by B, D, then C. Whereas at short times materials B and C are showing a higher change in rate followed by A and then D. A correlation can be established between the change in rate and the efficiency through considering both short and long times responses.

Table 12 Maximum force and damping efficiency for different materials

	Maximum Force (kN)	Damping efficiency (%)
Material A	11.473	0.11
Material B	9.755	0.22
Material C	10.158	0.08
Material D	10.181	0.05

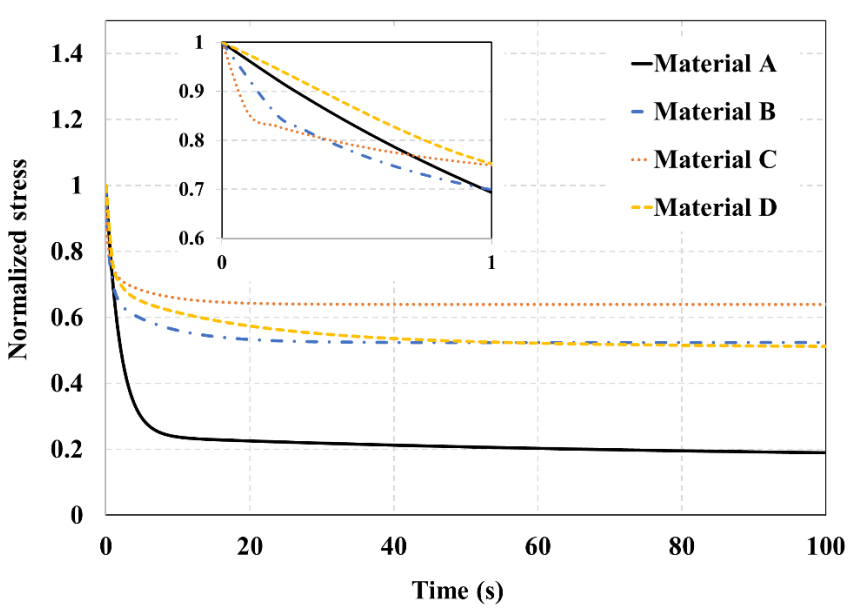

Figure 63 Stress relaxation of different materials. The inset shows the first second of the normalized stress-relaxation curve to highlight the drop in normalized stress at short times.

The criteria of high damping efficiency depend on having a higher rate of the drop (rate of change of normalized stress), especially at short time. This is evident from *Figure 64* which shows the rate of change in normalized stress with time or the rate of the drop with time. The difference in rate of drop across the materials greatly diminishes after 6 seconds. It can also be seen that material A maintains a rate of change for a longer period as opposed to the other materials. Nevertheless, at very short times it can be seen that materials B and C observe higher rates. Moreover, material B maintains a higher rate at short times for a longer period than material C. The higher rate at short times explains the

higher efficiency of material C over material D, and material B over material A. Therefore, the material that can provide the highest damping efficiency is one that experiences a high rate in the drop of its stress relaxation curve especially at short times.

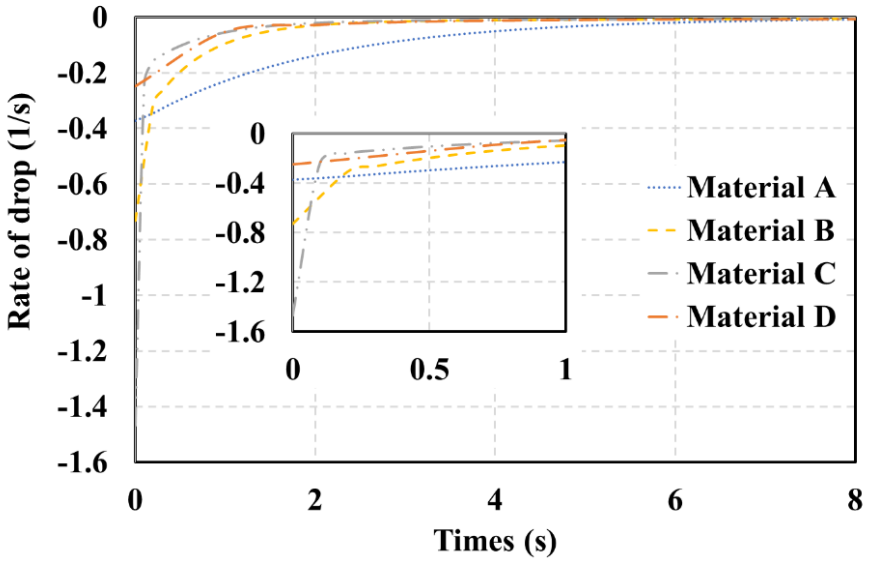

Figure 64 Rate of drop (change in normalized stress with time) vs. time. The inset shows the first second of the rate of drop to highlight the rate of drop in normalized stress at short times.

Based on the parametric studies conducted the response of MIVED can be greatly improved through changing the geometrical parameters of the interlocking system. A reduction in the radius and increase in the angle would help in increasing the strain in the TPU part which leads to higher energy dissipation. Also, the geometrical parameters can be varied depending on their proximity to the connection to optimize the performance. If, for example, higher axial strains are needed then a lower radius can be used for interlocks that are farther away from the connection. The potential of geometrical optimization of MIVED, however, can be truly realized if the device is fully 3D printed. In that case, the limitation of fabricating the rigid phase using conventional methods is no longer there and,

therefore, there is complete freedom in choosing the geometrical parameters of the interlocking system. Also, a choice of a 3D printable material that exhibits a stress relaxation behavior where the slope is high at short times (< 1 second) and has the ability to maintain the change in slope for a longer period.

4.5.2 MIVED-2

Figure 65 shows the force-displacement response of the damper at different amplitudes and 0.5 Hz loading frequency in addition to the device in both pull and push. The rigid phase experienced buckling deformations in both pull and push to generate the force-displacement response as shown in *Figure 65*.b and *Figure 65*.c. The single-angle-all-bolted connection used in the test developed a fixed boundary condition which resulted in mode II of the device. This is caused by the stiffness mismatch between the 3D printed fiberglass reinforced onyx flange and the angle connection. The mismatch is higher in favor of the flange in MIVED-1, whereas it is higher in favor of the connection in this case and, therefore, the flange had to buckle in response to the induced moments. It appears, however, that the moments in push cause an inward rotation of the flanges as opposed to the outward rotation in the pull case. This is attributed to the orientation or direction of the resultant contact force acting on the flanges which is causing a bending moment that acts in opposite directions in pull and push as can be seen in *Figure 65.b* and *Figure 65.c*. The nonlinear force-displacement response of the device is similar to the one observed with MIVED-1. In the 1 mm and 3 mm it appears that there is no difference in the behavior of the device when compared to MIVED-1 without any indication of SR involvement. However, for the 5 mm push the response is more linear in both loading and unloading in

addition to the increased plumpness of the response especially in push. These behaviors are indicative of the SR contribution to the response as they were not observed with TPU only. The late activation of SR indicates that the interlocking method is not the most efficient. Also, a strain amplitude dependence is noticed where the stiffness of the response increases as the amplitude decreases.

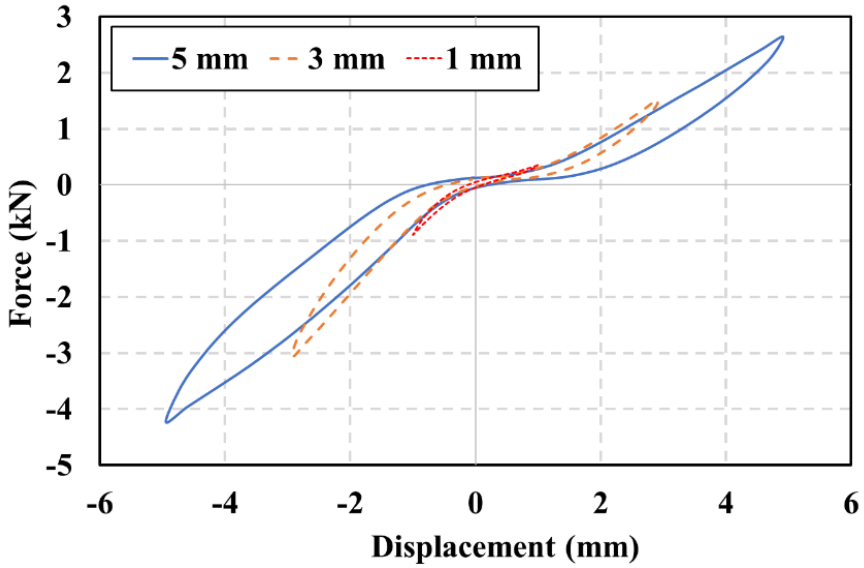

(a)

(b)

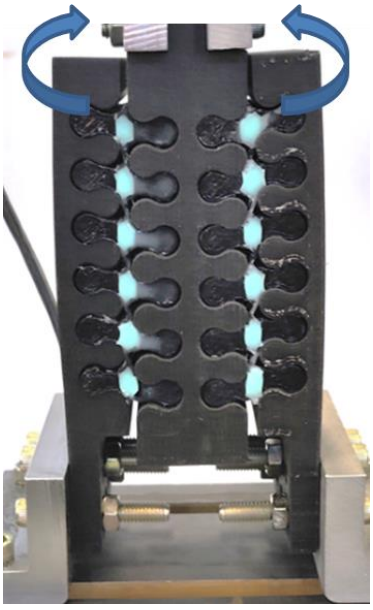

(c)

Figure 65 MIVED-2 (a) force-displacement at 0.5 Hz, 5 mm amplitude (b) pull (c) push

Figure 66.a shows that the response of MIVED-2 is different in the 1 mm amplitude case. This is due to the gaps between the two different phases of the device which is the same behavior observed in MIVED-1. *Figure 66*.b and *Figure 66*.c show that the behavior of MIVED-2 becomes more linear in push as the frequency is increased.

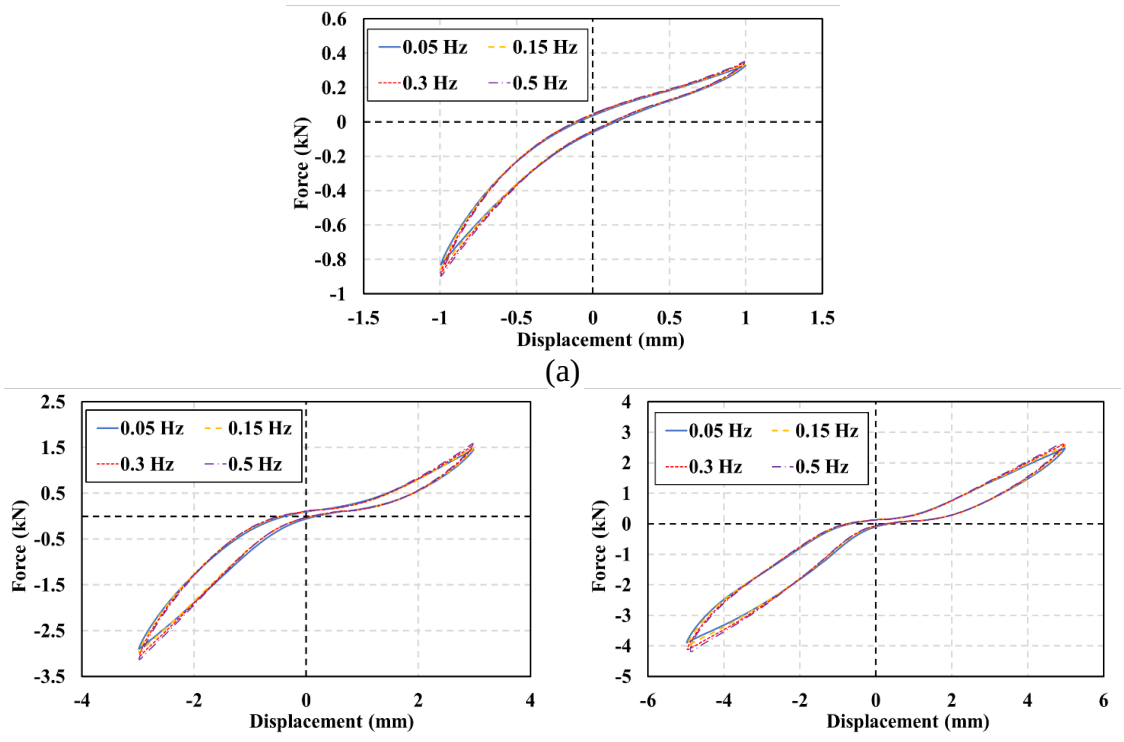

Figure 66. MIVED test results at (a) 1 mm (b) 3 mm (c) 5 mm

In this chapter TPU was used in a mechanically interlocked assembly as a damping device where energy was dissipated through multiple modes of deformation of the TPU part. The developed device has two modes of operation depending on the enforced boundary conditions. Mode I enforced a rigid body rotation of the flanges, whereas mode

II enforced rotation through buckling. Regardless of the mode, the device behaves in two distinct motions in response to the imposed displacements termed pull and push. DIC analysis of the flanges in mode I showed that high lateral displacements are associated with less force and energy dissipation. A FE model was developed to study the effect of the interlocking geometry of the device. It was shown that the efficiency of the device is customizable through changing the geometrical parameters of the interlocking pattern.

The fish-bone diagram in Figure 67 demonstrates the various variables that influence the behavior and performance of MIVEDs. The choice of materials used in the damper and the mechanical properties of those materials plays an important role in both stiffness and damping capacity of the device. These properties are crucial to reach the desired output performance. The processing parameters of the printed part plays a major role in determining the performance of the 3D printed damping material as they control the density of the part [45,69,70]. Finally, the interlocking mechanism and the choice of the geometrical parameters will determine the “bond” strength between the soft and rigid parts of the damper.

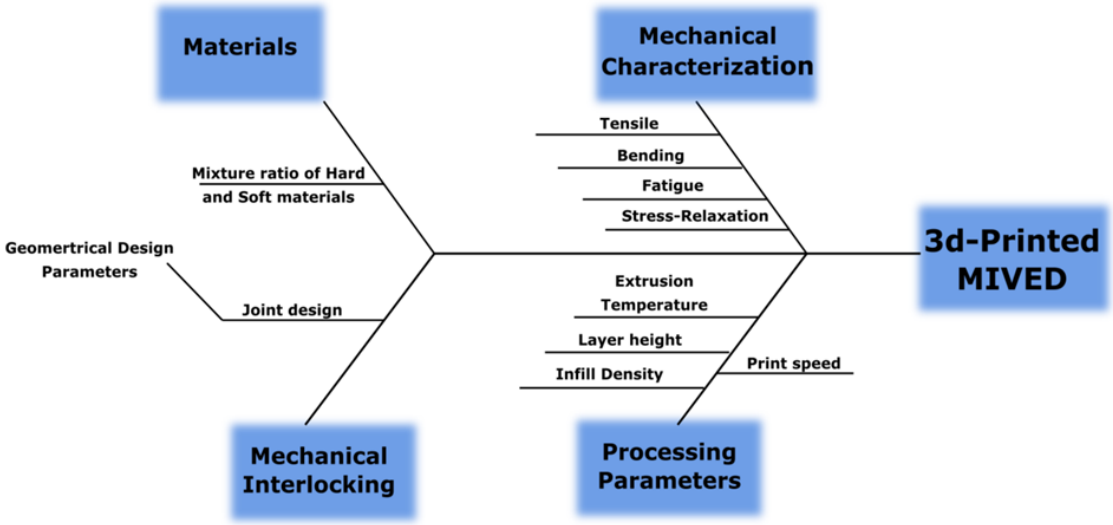

Figure 67. Variables that influence the performance of MIVED

Chapter 5: **Analysis of single-story frame structure using viscoelastic dampers**

To assess the damping performance of the MIVED device, a simplified model was developed and then incorporated into a one-bay single-story 2D steel frame structure. A VED from the literature was also used to compare with the damper developed in this work. The frame was exposed to the 1940 El Centro earthquake with and without damping devices, and the performance of the frame structure was studied in both cases. Frame and device models were developed using SAP2000 [93]. This chapter is only intended on highlighting the energy dissipation capabilities of the damper and, therefore, the other features of the device will not be accounted for.

5.1 Device Modeling

The device is modeled using a kelvin-voigt element which consists of a spring and dashpot in parallel as shown in *Figure 68*. This was implemented in SAP2000 using two LINK elements: a spring and a dashpot in parallel. The stiffness and damping coefficients of the model were calculated using the equations developed for a steady-state response of a viscoelastic solid material [102].

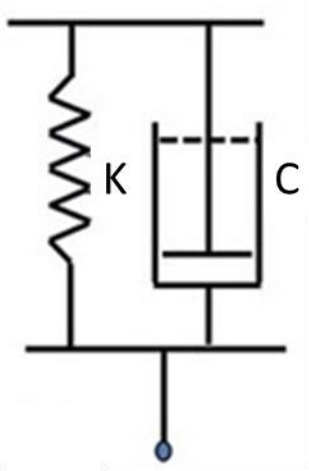

Figure 68 Kelvin-voigt model

The resulting force from the kelvin element is:

$$f = f_s + f_d = ku + c\dot{u} \tag{19}$$

where k and c are the stiffness and damping coefficients, respectively, and u is the measured displacement of the kelvin element and $\dot{u}$ is the rate of change in displacement. The stiffness coefficient was calculated from the averaged peak force values of pull (f_s^+) and push (f_s^-) of the MIVED device:

$$k = \frac{\frac{|f_s^+| + |f_s^-|}{2}}{u_o} \tag{20}$$

Where: u_o is the maximum displacement of the device. The damping coefficient is calculated using the energy dissipated (ED) during one cycle of loading-unloading as follows:

$$c = \frac{ED}{\pi\omega u_o^2} \tag{21}$$

Where: ω is the circular frequency of the imposed load or displacement. The damping force can be calculated using the following formula:

$$f_d = c\omega\sqrt{u_o^2 - u^2} \quad (22)$$

The sign of the damping force is dependent on whether it is loading (+) or unloading (-). Finally, the spring and dashpot forces are summed together and plotted against the displacement to give the response of the simplified model of the device as shown in Figure 69.a. The simplified model of the MIVED device will be referred to hereafter as device 1 because of the introduction of another VED (device 2). This device is a conventional viscoelastic damper based on 3M ISD 110 viscoelastic material, and the expressions necessary to find the stiffness and damping coefficients were identified by Abbas and Kelly [95]. Since device 1 is modeled based on the experimental response of the interlocked damper, there are no expressions that account for the sheared viscoelastic area. This prevented scaling up the response from lab testing to field applications. Therefore, device 2 coefficients were calculated based on an equivalent material volume to device 1 as well as the same loading frequency (0.5 Hz) and a shear strain level of 100%. The stiffness and damping coefficients for device 2 are expressed as follows:

$$K = G'At \quad (23)$$

$$C = G''Aft \quad (24)$$

Where G' and G'' are the storage and loss moduli, respectively, and f, A, and t are the loading frequency, area, and thickness of the viscoelastic materials, respectively. To obtain expressions for the moduli:

$$G' = 16.0 f^{0.51} \gamma^{-0.23} e^{\frac{72.46}{Temp}} \quad (25)$$

$$G'' = 18.5 f^{0.51} \gamma^{-0.20} e^{\frac{73.89}{Temp}} \quad (26)$$

The response of device 2 compared to the experimental and analytical responses of device 1 can be seen in Figure 69.b.

Table 13 Damper coefficients for device 1 and device 2

Device/coefficients	K (N/mm)	C (N.s/mm)
Damper 1	2703.6	78.0
Damper 2	2359.0	868.0

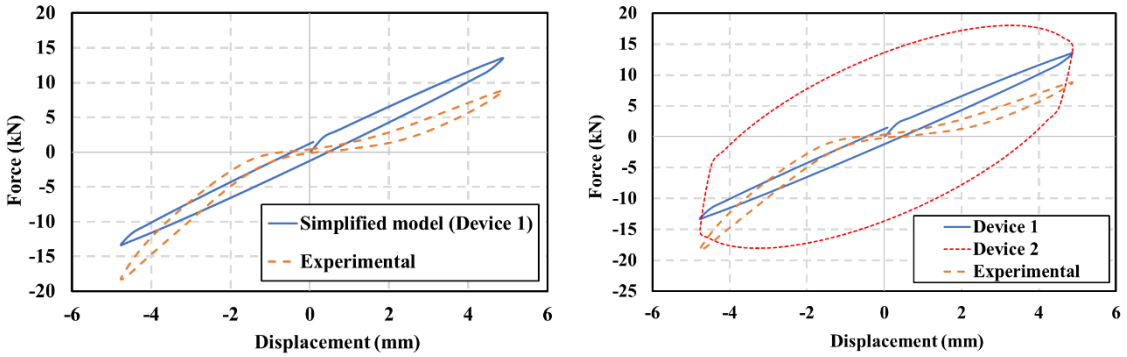

(a) (b)

Figure 69 (a) Simplified model of MIVED (device 1) with experimental response (b) device 2 in comparison to device 1 and experimental responses

This simplified model was chosen because it is very easy to implement and gives a good measure of the energy dissipation capability of the damper. The error in energy dissipation between the simplified model and the experimental response is less than 1%.

However, the simplified model is unable to predict or model the nonlinear behavior of MIVED due to the absence of nonlinear terms in the model. Therefore, the unique feature of MIVED of having different stiffnesses in tension and compression will not be accounted for in the simplified model.

5.2 Single-story frame structure

To test the performance of the damping devices, they were used as part of a braced frame system undergoing strong ground motion. The single-story structural steel system considered in the study is composed of five single-span portal frames equally spaced with the geometry shown in *Figure 70*.a. A 200 mm thick concrete slab is carried by the structural frame system. A single frame in the middle of the structural system, emphasized in *Figure 70*.b and shown in *Figure 70*.c, was modeled with and without damping devices. The cross-sections of the structural members that composes the frame are shown in *Figure 70*.c. The figure also shows the rheological model used to represent the damper and the bracing system. The damper and the bracing are running parallel to each other which means that the stiffness (K) represents both the bracing and the damper stiffnesses. Whereas the damping (C) is only associated with the damping device. This is justified since dampers can typically be installed in parallel to frame bracings as can be seen in *Figure 70*.d [103]. The frame was then subjected to a nonlinear time-history analysis was using the 1940 El Centro, CA earthquake ground acceleration shown in *Figure 70*.e.

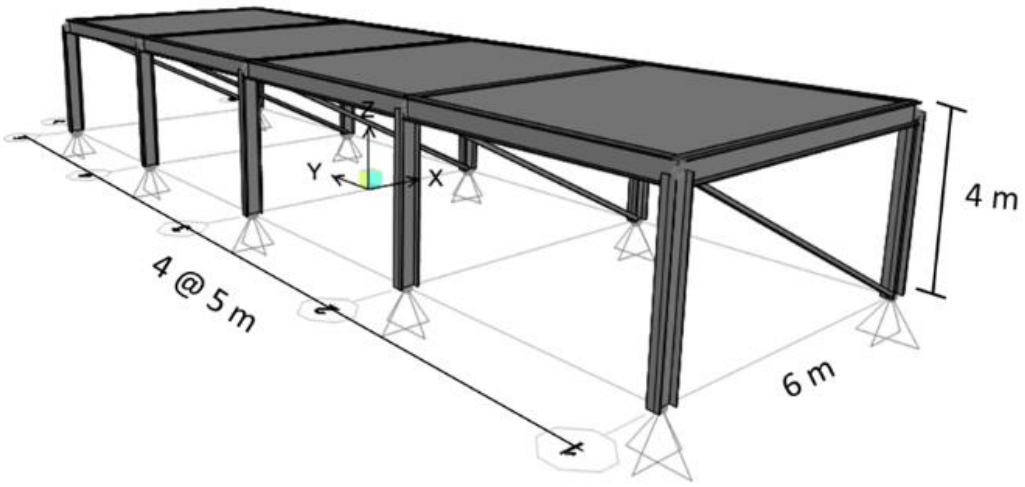
Z
Y
X
4 m
4@5 m
6 m

(a)

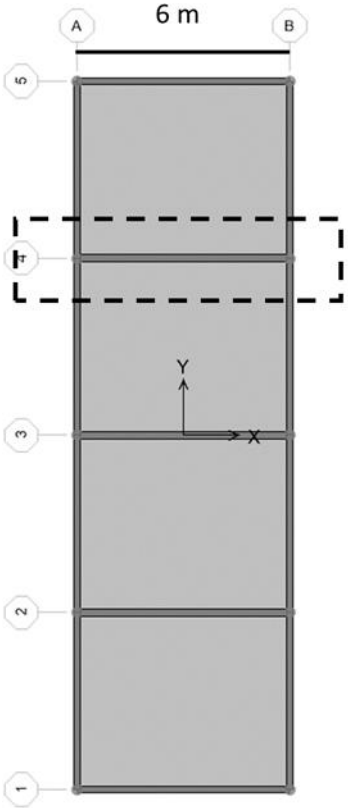
A
B
6 m
5
4
3
2
1
Y
X

(b)

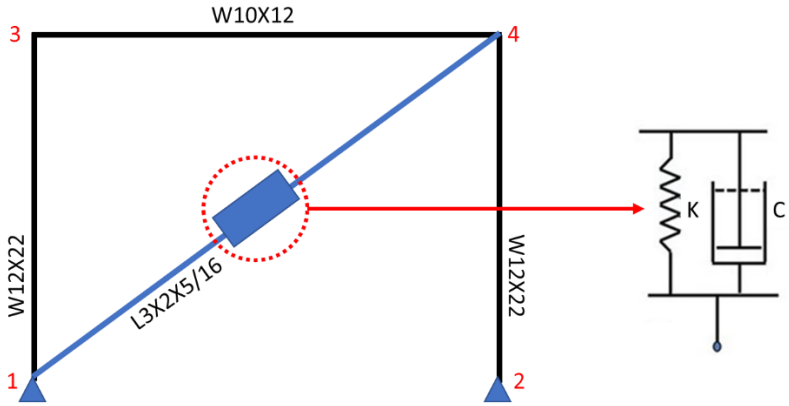
W10X12
3
4
W12X22
L3X2X5/16
W12X22
1
2
K
C

(c)

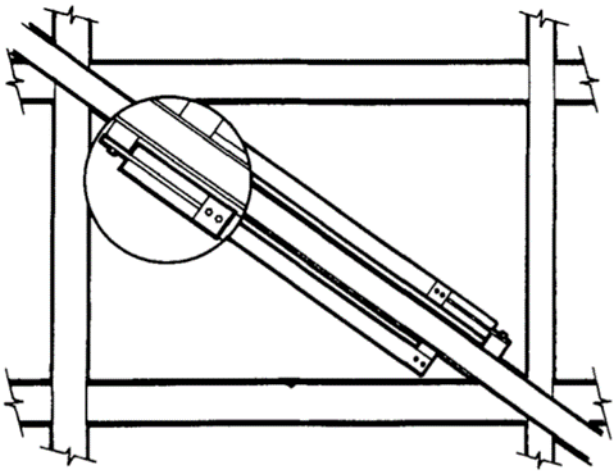

(d)

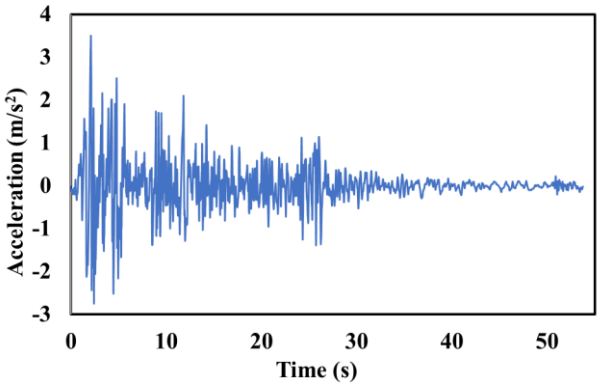

(e)

Figure 70 (a) Geometry of frame structure (b) structural plan (c) 2D FE model and sections (d) Example of VED location on a frame [103] *(e) 1940 El Centro ground acceleration*

The first three modal frequencies and periods were identified and are shown in *Table 14*. It can be seen from the table that the addition of viscoelastic dampers has a minimal effect on the natural characteristics of the frame. This is clear as the change in fundamental period or frequency of the frame is almost negligible in all cases.

Table 14 Modal periods and frequencies

Mode	Period (s)			Frequency (Hz)		
	Without	With device 1	With device 2	Without	With device	With device 2
1	0.185	0.178	0.179	5.39	5.59	5.56
2	0.039	0.042	0.042	25.31	23.37	23.36
3	0.038	0.037	0.037	25.74	26.64	26.64

The displacement and acceleration at joint 4 of the frame, shown in *Figure 71*, were recorded with and without the damping devices. The effect of the damping devices is clear as both displacement and acceleration at the joint were reduced. However, device 2 was able to substantially reduce the amplitude as well as quickly dampen the response

of the frame system when compared to device 1. This is due to the higher damping coefficient of device 2. *Table 15* shows the maximum normalized displacements and accelerations at joint 4. The values were normalized to the maximum displacement and acceleration of the frame without any damping devices. Device 2 was able to suppress accelerations and displacements by 17% and 25%, respectively, more than device 1. Nonetheless, considering that the damping coefficient of device 2 is 10 times higher than device 1, the difference in the effectiveness of the response is not substantial.

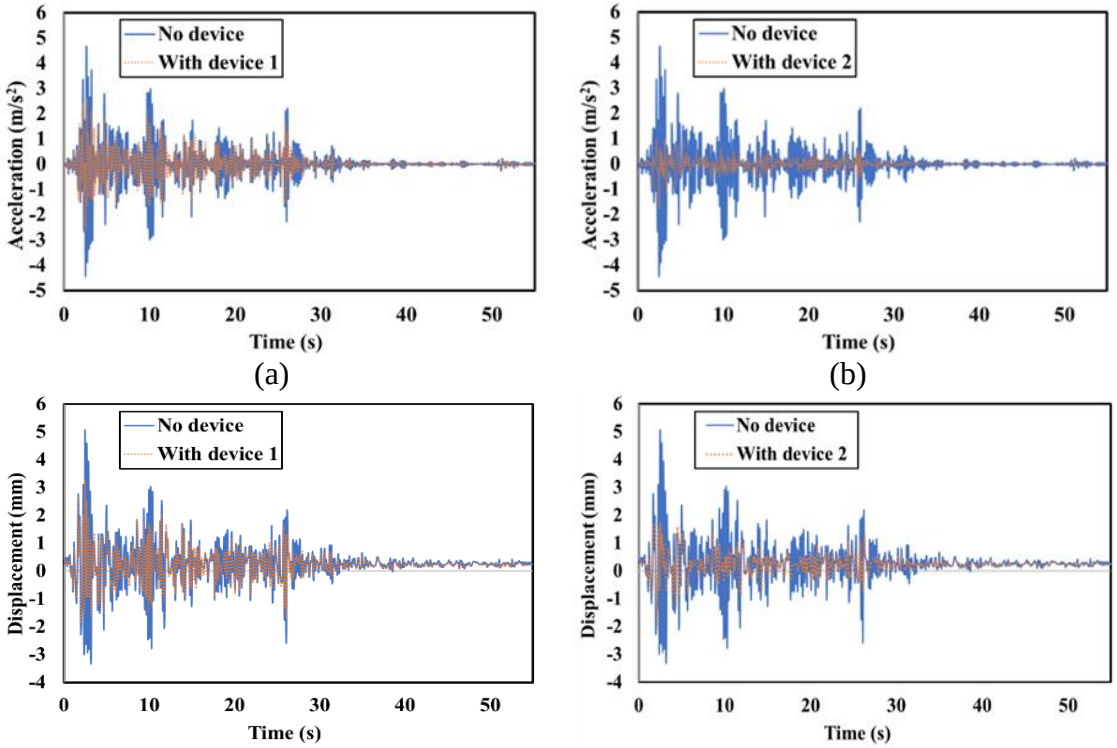

Figure 71 Acceleration and displacement time history responses at joint 4 with and without damping devices (a) acceleration with and without device 1 (b) acceleration with and without device 2 (c) displacement with and without device 1 (d) displacement with and without device 2

Table 15 Maximum normalized accelerations and displacements at joint 4

	$\lvert a_{max}\rvert$(m/s^2)	$\frac{\lvert a_{max}\rvert}{\lvert a_{w/o}\rvert}$%	$\lvert d_{max}\rvert$(mm)	$\frac{\lvert d_{max}\rvert}{\lvert d_{w/o}\rvert}$%
Without devices (w/o)	4.65	100	5.08	100
With device 1	2.57	55	3.28	65
With device 2	1.76	38	2.02	40

Figure 72 compares the base shear force in the frame structure with and without damping devices. The reduction in base shear is directly related to the ability of the device to reduce accelerations. Therefore, device 2 was able to reduce the amount of base shear force that the frame system undergoes during the earthquake loading. Device 1, on the other hand, did not have much of an effect on the base shear force of the frame although device 1 was able to reduce the acceleration. This is because stiffness of the device also contributes to the force. Therefore, the ratio of stiffness to damping coefficients of the device plays an important role in the resulting base shear of the structure.

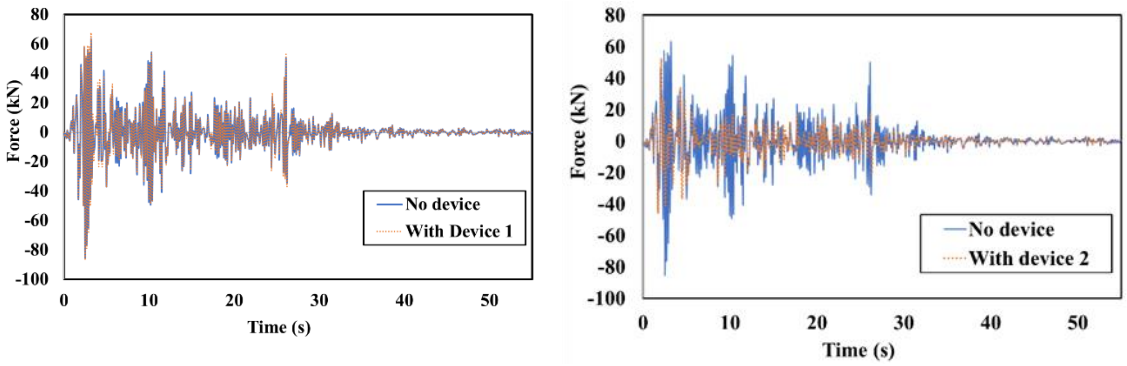

(a) (b)

Figure 72 Base shear force time history response of frame structure (a) frame with and without device 1 (b) frame with and without device 2

Figure 73 shows that tension forces are almost two times higher than compression forces in both devices. Moreover, device 2 was able to produce higher forces in both tension and compression than device 1. Although the stiffness of device 1 is higher than

device 2, the contribution of the damping force is significant and resulted in a higher force for device 2. It is interesting to note that with accurate modeling of MIVED it is possible to obtain comparable tension and compression values due to the different stiffnesses observed by MIVED in opposite loading directions.

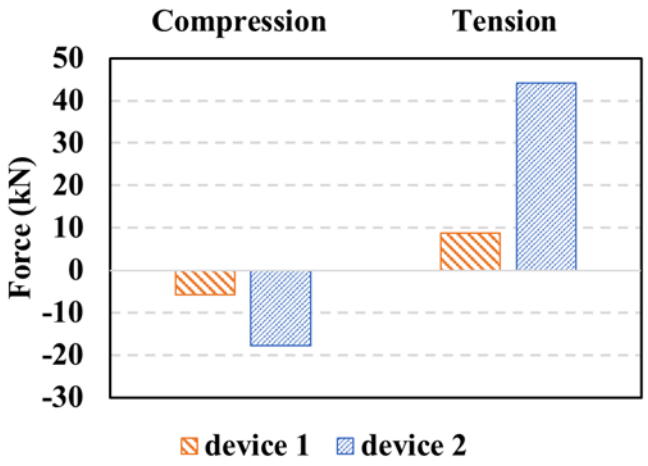

Figure 73 Maximum force in viscoelastic dampers for device 1 and device 2 in compression and tension

In summary, a single-story braced frame structure was numerically developed and tested with and without viscoelastic dampers. This is considered as the first step in representing large scale performance. Two damping devices were used: the MIVED device developed in this work (device 1) and a high-damping device obtained from literature (device 2). Simplified models of the dampers were incorporated within the frame structure using a kelvin-voigt element. The results demonstrated the effectiveness of both viscoelastic dampers in suppressing earthquake-induced loads. Nevertheless, device 2 outperformed device 1 due to the higher damping capacity of the device. It was also observed that both devices did not impact the natural characteristics of the frame due to the relatively low stiffness of the devices when compared to the overall structure. The

performance of device 1 within a structural frame system can be improved to attenuate the displacements and accelerations induced in the frame. This can be done through optimizing the interlocking geometry in a way that maximizes the strain induced in the viscoelastic layer given a specific displacement. Also, the use of a high damping viscoelastic material that is 3D printable will improve the response of the device.

Chapter 6: **Conclusions**

In this dissertation, a 3D printed TPU produced via FDM was mechanically characterized and the effect of loading rate and infill pattern of specimens was examined. The 3D printed TPU was then used in a mechanically interlocked assembly to produce a MIVED device where the energy was dissipated through multiple modes of deformation of the TPU part. A FE model was developed to provide a further understanding of the behavior of the MIVED device and to study the effect of the interlocking geometry. A simplified model of the device was then incorporated into a structural frame system undergoing strong ground motion and the response of the structure was evaluated with and without damping devices. In this chapter, the conclusions of this investigation are presented then followed by the recommendations and suggestions for future work.

6.1 Conclusion

3D printed TPU specimens tested cyclically in uniaxial tension exhibited a nonlinear force-displacement response with inelastic effects. The tests were conducted at different strain rates and using different infill patterns for the TPU specimens. The TPU response can be represented by primary and stable responses which means that it can be modeled using either response depending on the loading scenario without considering inelastic effects. The tests showed that increasing the strain rate causes an increase in strength, modulus, and dissipated energy for the primary response. Whereas the stable response did not show any rate dependence for stress and modulus; however, it did show rate dependence for dissipated energy. It was also found that neither the infill pattern nor the interaction effect between strain rate and infill pattern influences the mechanical

properties of TPU. The density of the printed part is the only factor that contributes to the mechanical properties of the 3D printed TPU. This shows that FDM technology can produce 3D printed TPU parts with isotropic behavior if it is printed with infill percentages approaching 100%. The results of the tested specimens were used to develop a visco-hyperelastic material model. The model was able to capture the behavior of the TPU specimen and it was later validated with experimental tests on a traditional viscoelastic damper made out of 3D printed TPU.

The developed MIVED can operate at two different modes, modes I and II, depending on the bending rigidity of soft and rigid phases in addition to the rigidity of the connection used between the damper and the structure. This combination of bending rigidity between materials and connection basically determines the boundary conditions of the device which governs the mode of operation of the device. Moreover, the force-displacement response of MIVED is not symmetrical and can be divided into two different motions, a pull (tension) and push (compression). The response is stiffer in push as opposed to pull due to the lateral movement of the flanges. In the case of pull the flanges are relatively free to rotate while in push the flanges are restrained as they are pushed against the connection. This forces a change in loading rate by MIVED due to the difference in lateral flange movement between push and pull resulting in a higher response in push.

The stiffness of MIVED-1 (mode I) is dependent on the amplitude in both push and pull where the stiffness increases as the amplitude decreases. On the other hand, the stiffness of the device shows a slight increase within the tested frequency range for the pull and remains the same for the push. It was also shown that MIVED-1 in push is associated

with lower lateral displacements and higher forces when compared to loading in the pull. The FE simulations of MIVED-1 showed that the TPU is pushing the side flanges laterally away from the center due to the development of contact pressure between rigid and soft phases. They also highlighted the different strain states experienced by TPU such as shear, tension, and compression. A parametric study was conducted on both the geometrical parameters and material parameters of MIVED, and the damping efficiency was compared between the different models. The study showed that the highest damping efficiency is associated with geometrical parameters that produce the highest strains in TPU. The material parameters, on the other hand, showed that the highest damping efficiency is associated with the rate of drop in stress for stress relaxation curves especially at short times (0-1 s).

MIVED-2 (mode II) exhibited buckling of the rigid phase as opposed to MIVED-1 (mode I) which displayed a rigid body rotation of the rigid phase. In this mode, the moment acting on the device in pull is in an opposite direction to the moment applied during push due to the direction of the resultant contact force between soft and rigid phases. The device in this mode is frequency dependent as the stiffness of the response increases when the frequency is increased. It is also dependent on amplitude where the stiffness of the force-displacement response increases with decreasing amplitude. The inclusion of silicone rubber contributed to the overall behavior of MIVED-2 at higher levels of strain which indicates that the method of combining the two materials was not the most effective.

The device was numerically tested within a structural frame system to assess to its impact on the frame response under strong ground motions. El Centro earthquake was used

to load a single-story frame structure and the response was evaluated with and without damping devices. The device showed that it is capable of effectively reducing accelerations and displacements. However, the device was not able to attenuate the base shear forces in the frame structure due to earthquake loading.

6.2 Limitations and future work

- MIVED is highly susceptible to failure when subjected to out-of-plane loads due to the absence of chemical bond between rigid and soft phases.
- TPU characterization should include more modes of deformation such as planar shear and biaxial which leads to a better understanding of material behavior in addition to a more reliable material model.
- The inclusion of a damage model such as the Ogden-Roxburgh damage model [41] will provide better predictions of the materials response.
- Further investigation of print processing parameters should be conducted to find out which parameters lead to a higher part density and, therefore, higher TPU mechanical properties.
- Investigation of 3D p2^{r}intable materials with higher damping capacity than TPU.
- Explore different interlocking geometries and designs that will induce higher strains than the geometry used in this dissertation.
- Limitations due to the FDM technology such as interlayer adhesion, object/bed adhesion, complex geometries, and extrusion failure mechanisms.

- MIVED can provide higher damping, impact absorption, and alter the natural frequency through the incorporation of shear thickening fluid (STF) into the matrix of soft or rigid phases of the device. The use of STF as an encapsulated material within another material has been utilized in the literature through sandwich structures or panels [104,105], fluid dampers [106,107], multi-layered cork structures [108], and tubes of carbon fiber reinforced polymer composites [109,110].
- The introduction of structural hierarchy into the interlocking system can lead to improved stiffness and energy dissipation as well as shape integrity [13,78]. It is also possible to produce tunable stiffness and energy absorption properties by incorporating hierarchy [12,82].
- The incorporation of nanomaterials such as carbon nanotubes into the TPU matrix has been proven to improve the mechanical, thermal, electrical, and piezoresistive properties of TPU [60–62].
- Further investigation of MIVED-2 such as flexural characterization of onyx reinforced with fiberglass is necessary to develop a better understanding of mode II of the device.
- Investigate the incorporation of a rigid phase material that can contribute to the energy dissipation process. Cellular structures, for example, with soft and rigid phases have been used to produce simultaneously high specific stiffness and damping [15]. Also, nacre like structures can provide a combination of stiffness, strength, and toughness by employing the same technique of rigid and soft phases [9,10]. Such a device would occupy the

space bounded by the purple rectangle on the material-property chart of loss coefficient and young's modulus.

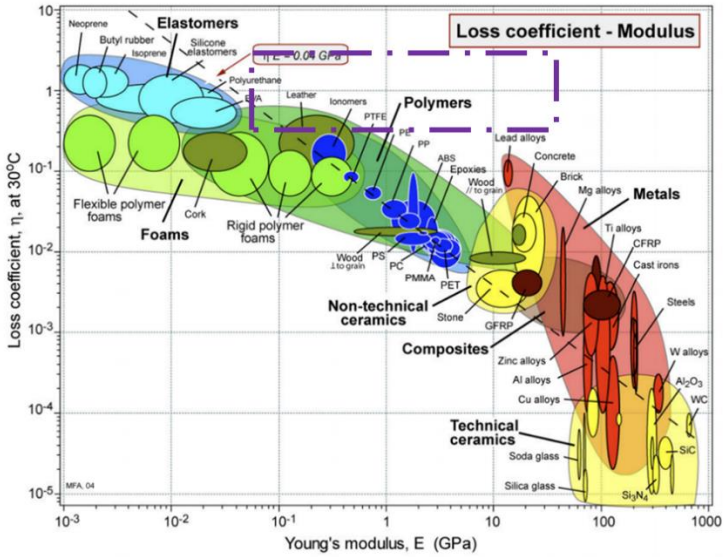

Figure 74 Material-property chart of loss coefficient and young's modulus (Extracted from Ashby 2009 [111]*)*

- An improved analytical model of the MIVED can lead to a better understanding of the damper effect on the response of structural systems. The model should involve different stiffnesses in push and pull directions as well as nonlinear terms for the springs.

Chapter 7: **References**

[1] R. Burdzik, Identification of structure and directional distribution of vibration transferred to car-body from road roughness, J. Vibroengineering. 16 (2014) 324–333. https://www.jvejournals.com/article/14764 (accessed October 31, 2021).

[2] G.C. Conroy, P. Sideris, Exploring energy harvesting and vibration mitigation in tall buildings accounting for wind and seismic loads, Eng. Struct. 247 (2021) 113126. https://doi.org/10.1016/j.engstruct.2021.113126.

[3] Y. Amini, M. Heshmati, P. Fatehi, S.E. Habibi, Energy Harvesting from Vibrations of a Functionally Graded Beam due to Moving Loads and Moving Masses, J. Eng. Mech. 143 (2017) 04017063. https://doi.org/10.1061/(asce)em.1943-7889.0001272.

[4] H. Liang, G. Hao, O.Z. Olszewski, A review on vibration-based piezoelectric energy harvesting from the aspect of compliant mechanisms, Sensors Actuators, A Phys. 331 (2021) 112743. https://doi.org/10.1016/j.sna.2021.112743.

[5] D.R. Pant, M. Montgomery, C. Christopoulos, Full-Scale Testing of a Viscoelastic Coupling Damper for High-Rise Building Applications and Comparative Evaluation of Different Numerical Models, J. Struct. Eng. (United States). 145 (2019). https://doi.org/10.1061/(ASCE)ST.1943-541X.0002246.

[6] Z.D. Xu, Earthquake mitigation study on viscoelastic dampers for reinforced concrete structures, JVC/Journal Vib. Control. 13 (2007) 29–43. https://doi.org/10.1177/1077546306068058.

[7] M.D. Rao, Recent applications of viscoelastic damping for noise control in automobiles and commercial airplanes, J. Sound Vib. 262 (2003) 457–474. https://doi.org/10.1016/S0022-460X(03)00106-8.

[8] X.Q. Zhou, D.Y. Yu, X.Y. Shao, S.Q. Zhang, S. Wang, Research and applications of viscoelastic vibration damping materials: A review, Compos. Struct. 136 (2016) 460–480. https://doi.org/10.1016/J.COMPSTRUCT.2015.10.014.

[9] P. Zhang, M.A. Heyne, A.C. To, Biomimetic staggered composites with highly enhanced energy dissipation: Modeling, 3D printing, and testing, J. Mech. Phys. Solids. 83 (2015) 285–300. https://doi.org/10.1016/j.jmps.2015.06.015.

[10] F. Liu, T. Li, Z. Jia, L. Wang, Combination of stiffness, strength, and toughness in 3D printed interlocking nacre-like composites, Extrem. Mech. Lett. 35 (2020) 100621. https://doi.org/10.1016/j.eml.2019.100621.

[11] S. Liu, A.I. Azad, R. Burgueño, Architected materials for tailorable shear behavior with energy dissipation, Extrem. Mech. Lett. 28 (2019) 1–7. https://doi.org/10.1016/j.eml.2019.01.010.

[12] M. Mirkhalaf, F. Barthelat, Design, 3D printing and testing of architectured materials with bistable interlocks, Extrem. Mech. Lett. 11 (2017) 1–7. https://doi.org/10.1016/j.eml.2016.11.005.

[13] Y. Chen, T. Li, Z. Jia, F. Scarpa, C.W. Yao, L. Wang, 3D printed hierarchical honeycombs with shape integrity under large compressive deformations, Mater.

Des. 137 (2018) 226–234. https://doi.org/10.1016/J.MATDES.2017.10.028.

[14] B. Hussey, P. Nikaeen, M.D. Dixon, M. Akobi, A. Khattab, L. Cheng, Z. Wang, J. Li, T. He, P. Zhang, Light-weight/defect-tolerant topologically self-interlocking polymeric structure by fused deposition modeling, Compos. Part B Eng. 183 (2020) 107700. https://doi.org/10.1016/j.compositesb.2019.107700.

[15] Z. Xu, C.S. Ha, R. Kadam, J. Lindahl, S. Kim, H.F. Wu, V. Kunc, X. Zheng, Additive manufacturing of two-phase lightweight, stiff and high damping carbon fiber reinforced polymer microlattices, Addit. Manuf. 32 (2020) 101106. https://doi.org/10.1016/J.ADDMA.2020.101106.

[16] M.D. Symans, F.A. Charney, A.S. Whittaker, M.C. Constantinou, C.A. Kircher, M.W. Johnson, R.J. McNamara, Energy dissipation systems for seismic applications: Current practice and recent developments, J. Struct. Eng. 134 (2008) 3–21. https://doi.org/10.1061/(ASCE)0733-9445(2008)134:1(3).

[17] E.J. Nielsen, M.-L. Lai, T.T. Soong, J.M. Kelly, <title>Viscoelastic damper overview for seismic and wind applications</title>, in: C.D. Johnson (Ed.), Smart Struct. Mater. 1996 Passiv. Damping Isol., SPIE, 1996: pp. 138–144. https://doi.org/10.1117/12.239081.

[18] L. Chen, L. Sun, Y. Xu, F. Di, Y. Xu, L. Wang, A comparative study of multi-mode cable vibration control using viscous and viscoelastic dampers through field tests on the Sutong Bridge, Eng. Struct. 224 (2020) 111226. https://doi.org/10.1016/j.engstruct.2020.111226.

[19] Z.D. Xu, D.X. Wang, C.F. Shi, Model, tests and application design for viscoelastic dampers, JVC/Journal Vib. Control. 17 (2011) 1359–1370. https://doi.org/10.1177/1077546310373617.

[20] M.D. Rao, Recent applications of viscoelastic damping for noise control in automobiles and commercial airplanes, in: J. Sound Vib., Academic Press, 2003: pp. 457–474. https://doi.org/10.1016/S0022-460X(03)00106-8.

[21] Z. Lu, Z. Wang, Y. Zhou, X. Lu, Nonlinear dissipative devices in structural vibration control: A review, J. Sound Vib. 423 (2018) 18–49. https://doi.org/10.1016/J.JSV.2018.02.052.

[22] Y. Yu, N.G. Naganathan, R. V. Dukkipati, A literature review of automotive vehicle engine mounting systems, Mech. Mach. Theory. 36 (2001) 123–142. https://doi.org/10.1016/S0094-114X(00)00023-9.

[23] B. Silwal, R.J. Michael, O.E. Ozbulut, A superelastic viscous damper for enhanced seismic performance of steel moment frames, Eng. Struct. 105 (2015) 152–164. https://doi.org/10.1016/j.engstruct.2015.10.005.

[24] C.C. Chou, W.H. Tseng, C.H. Huang, S. Tsuang, L.M. Chang, Y.H. Chen, A novel steel lever viscoelastic wall with amplified damper force-friction for wind and seismic resistance, Eng. Struct. 210 (2020). https://doi.org/10.1016/j.engstruct.2020.110362.

[25] Y.E. Ibrahim, J. Marshall, F.A. Charney, A visco-plastic device for seismic

protection of structures, J. Constr. Steel Res. 63 (2007) 1515–1528. https://doi.org/10.1016/j.jcsr.2007.01.007.

[26] M.H. Mehrabi, M. Suhatril, Z. Ibrahim, S.S. Ghodsi, H. Khatibi, Modeling of a viscoelastic damper and its application in structural control, PLoS One. 12 (2017). https://doi.org/10.1371/journal.pone.0176480.

[27] Y. Chen, C. Chen, Q. Ma, H. Jiang, Z. Wan, Study on mechanical properties of high damping viscoelastic dampers, Adv. Struct. Eng. 22 (2019) 2925–2936. https://doi.org/10.1177/1369433219853440.

[28] J. Yoshida, M. Abe, Y. Fujino, Constitutive model of high-damping rubber materials, J. Eng. Mech. 130 (2004) 129–141. https://doi.org/10.1061/(ASCE)0733-9399(2004)130:2(129).

[29] Y. Yuan, S. Wang, P. Tan, H. Zhu, Mechanical performance and shear constitutive model study of a new high-capacity polyurethane elastomeric bearing, Constr. Build. Mater. 232 (2020). https://doi.org/10.1016/j.conbuildmat.2019.117227.

[30] Z.D. Xu, Y.X. Liao, T. Ge, C. Xu, Experimental and Theoretical Study of Viscoelastic Dampers with Different Matrix Rubbers, J. Eng. Mech. 142 (2016) 04016051. https://doi.org/10.1061/(asce)em.1943-7889.0001101.

[31] S.W. Park, Analytical modeling of viscoelastic dampers for structural and vibration control, Int. J. Solids Struct. 38 (2001) 8065–8092. https://doi.org/10.1016/S0020-7683(01)00026-9.

[32] M.P. Singh, T.-S. Chang, Seismic Analysis of Structures with Viscoelastic Dampers, J. Eng. Mech. 135 (2009) 571–580. https://doi.org/10.1061/(ASCE)0733-9399(2009)135:6(571).

[33] T.S. Chang, M.P. Singh, Mechanical model parameters for viscoelastic dampers, J. Eng. Mech. 135 (2009) 581–584. https://doi.org/10.1061/(ASCE)0733-9399(2009)135:6(581).

[34] K.L. Shen, T.T. Soong, Modeling of Viscoelastic Dampers for Structural Applications, J. Eng. Mech. 121 (1995) 694–701. https://doi.org/10.1061/(ASCE)0733-9399(1995)121:6(694).

[35] C.S. Tsai, H.H. Lee, Applications of viscoelastic dampers to high-rise buildings, J. Struct. Eng. (United States). 120 (1994) 3683–3684. https://doi.org/10.1061/(ASCE)0733-9445(1994)120:12(3683).

[36] X.Q. Zhou, D.Y. Yu, X.Y. Shao, S.Q. Zhang, S. Wang, Research and applications of viscoelastic vibration damping materials: A review, Compos. Struct. 136 (2016) 460–480. https://doi.org/10.1016/j.compstruct.2015.10.014.

[37] N. Vaiana, S. Sessa, F. Marmo, L. Rosati, A class of uniaxial phenomenological models for simulating hysteretic phenomena in rate-independent mechanical systems and materials, Nonlinear Dyn. 93 (2018) 1647–1669. https://doi.org/10.1007/s11071-018-4282-2.

[38] M. Ismail, · Fayçal, · I., J. Rodellar, The Hysteresis Bouc-Wen Model, a Survey,

Arch Comput Methods Eng. 16 (2009) 161–188. https://doi.org/10.1007/s11831-009-9031-8.

[39] S. Gong, Y. Zhou, Experimental study and numerical simulation on a new type of viscoelastic damper with strong nonlinear characteristics, Struct. Control Heal. Monit. 24 (2017) e1897. https://doi.org/10.1002/stc.1897.

[40] H.M.C.C. Somarathna, S.N. Raman, D. Mohotti, A.A. Mutalib, K.H. Badri, Hyper-viscoelastic constitutive models for predicting the material behavior of polyurethane under varying strain rates and uniaxial tensile loading, Constr. Build. Mater. 236 (2020) 117417. https://doi.org/10.1016/j.conbuildmat.2019.117417.

[41] R. Tobajas, D. Elduque, E. Ibarz, C. Javierre, A.F. Canteli, L. Gracia, Visco-hyperelastic model with damage for simulating cyclic thermoplastic elastomers behavior applied to an industrial component, Polymers (Basel). 10 (2018). https://doi.org/10.3390/polym10060668.

[42] H. Khajehsaeid, J. Arghavani, R. Naghdabadi, S. Sohrabpour, A visco-hyperelastic constitutive model for rubber-like materials: A rate-dependent relaxation time scheme, Int. J. Eng. Sci. 79 (2014) 44–58. https://doi.org/10.1016/j.ijengsci.2014.03.001.

[43] R. Adams, S.P. Soe, R. Santiago, M. Robinson, B. Hanna, G. McShane, M. Alves, R. Burek, P. Theobald, A novel pathway for efficient characterisation of additively manufactured thermoplastic elastomers, Mater. Des. 180 (2019) 107917. https://doi.org/10.1016/j.matdes.2019.107917.

[44] M. Robinson, S. Soe, R. Johnston, R. Adams, B. Hanna, R. Burek, G. McShane, R. Celeghini, M. Alves, P. Theobald, Mechanical characterisation of additively manufactured elastomeric structures for variable strain rate applications, Addit. Manuf. 27 (2019) 398–407. https://doi.org/10.1016/j.addma.2019.03.022.

[45] F.F. Abayazid, M. Ghajari, Material characterisation of additively manufactured elastomers at different strain rates and build orientations, Addit. Manuf. 33 (2020) 101160. https://doi.org/10.1016/j.addma.2020.101160.

[46] R.L. Taylor, K.S. Pister, G.L. Goudreau, Thermomechanical analysis of viscoelastic solids, Int. J. Numer. Methods Eng. 2 (1970) 45–59. https://doi.org/10.1002/NME.1620020106.

[47] Z.D. Xu, D.X. Wang, C.F. Shi, Model, tests and application design for viscoelastic dampers, JVC/Journal Vib. Control. 17 (2011) 1359–1370. https://doi.org/10.1177/1077546310373617.

[48] S. Gong, Y. Zhou, P. Ge, Seismic analysis for tall and irregular temple buildings: A case study of strong nonlinear viscoelastic dampers, Struct. Des. Tall Spec. Build. 26 (2017) e1352. https://doi.org/10.1002/tal.1352.

[49] J.M. Tchamo, Y. Zhou, An alternative practical design method for structures with viscoelastic dampers, Earthq. Eng. Eng. Vib. 2018 173. 17 (2018) 459–473. https://doi.org/10.1007/S11803-018-0455-8.

[50] Z. Shu, Z. Gan, C. Fang, G. MacRae, H. Dong, Y. Xie, Replaceable Rotational

Viscoelastic Dampers for Improving Structural Damping and Resilience of Steel Frames, Https://Doi.Org/10.1080/13632469.2021.2009058. (2021). https://doi.org/10.1080/13632469.2021.2009058.

[51] D.G. Lignos, C. Molina-Hunt, A.D. Krebs, S.L. Billington, Comparison of Retrofitting Techniques for Existing Steel Moment Resisting Frames, Improv. Seism. Perform. Exist. Build. Other Struct. - Proc. 2009 ATC SEI Conf. Improv. Seism. Perform. Exist. Build. Other Struct. (2009) 988–999. https://doi.org/10.1061/41084(364)90.

[52] Y. Ohtori, R.E. Christenson, B.F. Spencer, S.J. Dyke, Benchmark control problems for seismically excited nonlinear buildings, J. Eng. Mech. 130 (2004) 366–385. https://doi.org/10.1061/(ASCE)0733-9399(2004)130:4(366).

[53] L.W. McKeen, Permeability Properties of Plastics and Elastomers: Fourth Edition, 2017.

[54] R.J. Spontak, N.P. Patel, Thermoplastic elastomers: Fundamentals and applications, Curr. Opin. Colloid Interface Sci. 5 (2000) 333–340. https://doi.org/10.1016/s1359-0294(00)00070-4.

[55] J. Herzberger, J.M. Sirrine, C.B. Williams, Polymer Design for 3D Printing Elastomers: Recent Advances in Structure, Properties, and Printing, Prog. Polym. Sci. 97 (2019) 101144. https://doi.org/10.1016/j.progpolymsci.2019.101144.

[56] E. Oelsch, R. Landgraf, L. Jankowsky, M. Kausch, S. Hoyer, W.-G. Drossel, J.

Ihlemann, Comparative investigation on the mechanical behavior of injection molded and 3D-printed thermoplastic polyurethane, J. Rubber Res. 24 (2021) 249–256. https://doi.org/10.1007/S42464-021-00092-W.

[57] C. Hohimer, J. Christ, N. Aliheidari, C. Mo, A. Ameli, 3D printed thermoplastic polyurethane with isotropic material properties, in: N.C. Goulbourne (Ed.), Behav. Mech. Multifunct. Mater. Compos. 2017, SPIE, 2017: p. 1016511. https://doi.org/10.1117/12.2259810.

[58] T.D. Ngo, A. Kashani, G. Imbalzano, K.T.Q. Nguyen, D. Hui, Additive manufacturing (3D printing): A review of materials, methods, applications and challenges, Compos. Part B Eng. 143 (2018) 172–196. https://doi.org/10.1016/J.COMPOSITESB.2018.02.012.

[59] M. Pagac, D. Schwarz, J. Petru, S. Polzer, 3D printed polyurethane exhibits isotropic elastic behavior despite its anisotropic surface, Rapid Prototyp. J. 26 (2020) 1371–1378. https://doi.org/10.1108/RPJ-02-2019-0027.

[60] R. Sattar, A. Kausar, M. Siddiq, Advances in thermoplastic polyurethane composites reinforced with carbon nanotubes and carbon nanofibers: A review, J. Plast. Film Sheeting. 31 (2015) 186–224. https://doi.org/10.1177/8756087914535126.

[61] J.F. Christ, N. Aliheidari, A. Ameli, P. Pötschke, 3D printed highly elastic strain sensors of multiwalled carbon nanotube/thermoplastic polyurethane nanocomposites, Mater. Des. 131 (2017) 394–401. https://doi.org/10.1016/j.matdes.2017.06.011.

[62] K. Kim, J. Park, J.-H. Suh, M. Kim, Y. Jeong, I. Park, 3D printing of multiaxial force sensors using carbon nanotube (CNT)/thermoplastic polyurethane (TPU) filaments, Sensors Actuators A. 263 (2017) 493–500. https://doi.org/10.1016/j.sna.2017.07.020.

[63] T.N.A.T. Rahim, A.M. Abdullah, H. Md Akil, Recent Developments in Fused Deposition Modeling-Based 3D Printing of Polymers and Their Composites, Polym. Rev. 59 (2019) 589–624. https://doi.org/10.1080/15583724.2019.1597883.

[64] M. Somireddy, A. Czekanski, Anisotropic material behavior of 3D printed composite structures – Material extrusion additive manufacturing, Mater. Des. 195 (2020) 108953. https://doi.org/10.1016/j.matdes.2020.108953.

[65] R. Zou, Y. Xia, S. Liu, P. Hu, W. Hou, Q. Hu, C. Shan, Isotropic and anisotropic elasticity and yielding of 3D printed material, Compos. Part B Eng. 99 (2016) 506–513. https://doi.org/10.1016/j.compositesb.2016.06.009.

[66] D. Popescu, A. Zapciu, C. Amza, F. Baciu, R. Marinescu, FDM process parameters influence over the mechanical properties of polymer specimens: A review, Polym. Test. 69 (2018) 157–166. https://doi.org/10.1016/j.polymertesting.2018.05.020.

[67] B. Akhoundi, A.H. Behravesh, Effect of Filling Pattern on the Tensile and Flexural Mechanical Properties of FDM 3D Printed Products, Exp. Mech. 59 (2019) 883–897. https://doi.org/10.1007/s11340-018-00467-y.

[68] S. Rohde, J. Cantrell, A. Jerez, C. Kroese, D. Damiani, R. Gurnani, L. DiSandro, J.

Anton, A. Young, D. Steinbach, P. Ifju, Experimental Characterization of the Shear Properties of 3D–Printed ABS and Polycarbonate Parts, Exp. Mech. 58 (2018) 871–884. https://doi.org/10.1007/s11340-017-0343-6.

[69] C. Hohimer, J. Christ, N. Aliheidari, C. Mo, A. Ameli, 3D printed thermoplastic polyurethane with isotropic material properties, in: Behav. Mech. Multifunct. Mater. Compos. 2017, 2017: p. 1016511. https://doi.org/10.1117/12.2259810.

[70] S. Chaudhry, M. Al-Dojayli, A. Czekanski, Performance of 3-D Printed Thermoplastic Polyurethane Under Quasi-Static and High-Strain Rate Loading, in: ASME International, 2016. https://doi.org/10.1115/imece2016-67839.

[71] J. Xiao, Y. Gao, The manufacture of 3D printing of medical grade TPU, Prog. Addit. Manuf. 2 (2017) 117–123. https://doi.org/10.1007/s40964-017-0023-1.

[72] L.R. Lopes, A.F. Silva, O.S. Carneiro, Multi-material 3D printing: The relevance of materials affinity on the boundary interface performance, Addit. Manuf. 23 (2018) 45–52. https://doi.org/10.1016/j.addma.2018.06.027.

[73] F. Awaja, M. Gilbert, G. Kelly, B. Fox, P.J. Pigram, Adhesion of polymers, Prog. Polym. Sci. 34 (2009) 948–968. https://doi.org/10.1016/j.progpolymsci.2009.04.007.

[74] F. Tamburrino, S. Graziosi, M. Bordegoni, The influence of slicing parameters on the multi-material adhesion mechanisms of FDM printed parts: an exploratory study, Virtual Phys. Prototyp. 14 (2019) 316–332.

https://doi.org/10.1080/17452759.2019.1607758.

[75] C.G. Harris, N.J.S. Jursik, W.E. Rochefort, T.W. Walker, Additive Manufacturing With Soft TPU – Adhesion Strength in Multimaterial Flexible Joints, Front. Mech. Eng. 5 (2019). https://doi.org/10.3389/fmech.2019.00037.

[76] J. Yin, C. Lu, J. Fu, Y. Huang, Y. Zheng, Interfacial bonding during multi-material fused deposition modeling (FDM) process due to inter-molecular diffusion, Mater. Des. 150 (2018) 104–112. https://doi.org/10.1016/j.matdes.2018.04.029.

[77] T. Siegmund, F. Barthelat, R. Cipra, E. Habtour, J. Riddick, Manufacture and Mechanics of Topologically Interlocked Material Assemblies, Appl. Mech. Rev. 68 (2016). https://doi.org/10.1115/1.4033967.

[78] M.M. Khoshhesab, Y. Li, Mechanical behavior of 3D printed biomimetic Koch fractal contact and interlocking, Extrem. Mech. Lett. 24 (2018) 58–65. https://doi.org/10.1016/j.eml.2018.09.003.

[79] I.A. Malik, M. Mirkhalaf, F. Barthelat, Bio-inspired “jigsaw”-like interlocking sutures: Modeling, optimization, 3D printing and testing, J. Mech. Phys. Solids. 102 (2017) 224–238. https://doi.org/10.1016/j.jmps.2017.03.003.

[80] A. Rezaee Javan, H. Seifi, X. Lin, Y.M. Xie, Mechanical behaviour of composite structures made of topologically interlocking concrete bricks with soft interfaces, Mater. Des. 186 (2020) 108347. https://doi.org/10.1016/j.matdes.2019.108347.

[81] S. Haldar, T. Sain, S. Ghosh, A novel high symmetry interlocking micro-architecture

design for polymer composites with improved mechanical properties, Int. J. Solids Struct. 124 (2017) 161–175. https://doi.org/10.1016/j.ijsolstr.2017.06.030.

[82] M. Imam, J. Meaud, S. Ghosh, T. Sain, Improvement of stiffness and energy absorption by harnessing hierarchical interlocking in brittle polymer blocks, J. Appl. Mech. Trans. ASME. 86 (2019). https://doi.org/10.1115/1.4042567.

[83] R.R. Ma, J.T. Belter, A.M. Dollar, Hybrid Deposition Manufacturing: Design Strategies for Multimaterial Mechanisms Via Three- Dimensional Printing and Material Deposition, J. Mech. Robot. 7 (2015) 1–10. https://doi.org/10.1115/1.4029400.

[84] L. Rossing, R.B.N. Scharff, B. Chömpff, C.C.L. Wang, E.L. Doubrovski, Bonding between silicones and thermoplastics using 3D printed mechanical interlocking, Mater. Des. 186 (2020) 108254. https://doi.org/10.1016/j.matdes.2019.108254.

[85] ASTM D412 - 16 Standard Test Methods for Vulcanized Rubber and Thermoplastic Elastomers—Tension, (n.d.). https://www.astm.org/Standards/D412 (accessed December 15, 2020).

[86] L. Mullins, Softening of Rubber by Deformation, Rubber Chem. Technol. 42 (1969) 339–362. https://doi.org/10.5254/1.3539210.

[87] N. McCormick, J. Lord, Digital image correlation, Mater. Today. 13 (2010) 52–54. https://doi.org/10.1016/S1369-7021(10)70235-2.

[88] J. Zhao, Y. Sang, F. Duan, The state of the art of two-dimensional digital image

correlation computational method, Eng. Reports. 1 (2019). https://doi.org/10.1002/eng2.12038.

[89] S. Moorthy, MODELING AND CHARACTERIZATION OF MECHANICAL PROPERTIES IN LASER POWDER BED FUSION ADDITIVE MANUFACTURED INCONEL 718, 2018.

[90] A. Inc, ABAQUS Version 6.10-1 Analysis User's Manual, Dassault Systèmes Simulia Corp. III (2017) 1–10. http://130.149.89.49:2080/v6.10/pdf_books/ANALYSIS_3.pdf (accessed May 29, 2019).

[91] R. Ogden, Large deformation isotropic elasticity – on the correlation of theory and experiment for incompressible rubberlike solids, Proc. R. Soc. London. A. Math. Phys. Sci. 326 (1972) 565–584. https://doi.org/10.1098/rspa.1972.0026.

[92] R.S. Rivlin, D.W. Saunders, Large elastic deformations of isotropic materials VII. Experiments on the deformation of rubber, Philos. Trans. R. Soc. London. Ser. A, Math. Phys. Sci. 243 (1951) 251–288. https://doi.org/10.1098/rsta.1951.0004.

[93] L. Bartolomé, J. Aurrekoetxea, M.A. Urchegui, W. Tato, The influences of deformation state and experimental conditions on inelastic behaviour of an extruded thermoplastic polyurethane elastomer, (2013). https://doi.org/10.1016/j.matdes.2013.02.055.

[94] A. Rezaee Javan, H. Seifi, X. Lin, Y.M. Xie, Mechanical behaviour of composite

structures made of topologically interlocking concrete bricks with soft interfaces, Mater. Des. 186 (2020). https://doi.org/10.1016/j.matdes.2019.108347.

[95] K. Hong, J.G. Yang, S.K. Lee, Moment–rotation behavior of double angle connections subjected to shear load, Eng. Struct. 24 (2002) 125–132. https://doi.org/10.1016/S0141-0296(01)00014-1.

[96] S. Yan, L. Jiang, K.J.R. Rasmussen, Full-range behaviour of double web angle connections, J. Constr. Steel Res. 166 (2020) 105907. https://doi.org/10.1016/j.jcsr.2019.105907.

[97] Y. Gong, Single-angle all-bolted shear connections, J. Constr. Steel Res. 65 (2009) 1337–1345. https://doi.org/10.1016/j.jcsr.2008.12.002.

[98] Z. Kong, S.E. Kim, Numerical estimation of the initial stiffness and ultimate moment capacity of single-web angle connections, J. Constr. Steel Res. 121 (2016) 282–290. https://doi.org/10.1016/J.JCSR.2016.02.011.

[99] T. Reppel, K. Weinberg, Experimental determination of elastic and rupture properties of printed Ninjaflex, Tech. Mech. 38 (2018) 104–112. https://doi.org/10.24352/UB.OVGU-2018-010.

[100] CSI, SAP2000 Integrated Software for Structural Analysis and Design, Comput. Struct. (n.d.).

[101] CSI, SAP2000. Analysis Reference Manual, CSI Berkeley (CA, USA) Comput. Struct. INC. (2016).

[102] A.K. Chopra, Dynamics of structures : theory and applications to earthquake engineering, 2012.

[103] R. -H Zhang, T.T. Soong, P. Mahmoodi, Seismic response of steel frame structures with added viscoelastic dampers, Earthq. Eng. Struct. Dyn. 18 (1989) 389–396. https://doi.org/10.1002/EQE.4290180307.

[104] M. Jeddi, M. Yazdani, H. Hasan-nezhad, Energy absorption characteristics of aluminum sandwich panels with Shear Thickening Fluid (STF) filled 3D fabric cores under dynamic loading conditions, Thin-Walled Struct. 168 (2021) 108254. https://doi.org/10.1016/J.TWS.2021.108254.

[105] S. Gürgen, M.A. Sofuoğlu, Vibration attenuation of sandwich structures filled with shear thickening fluids, Compos. Part B Eng. 186 (2020). https://doi.org/10.1016/j.compositesb.2020.107831.

[106] K. Lin, A. Zhou, H. Liu, Y. Liu, C. Huang, Shear thickening fluid damper and its application to vibration mitigation of stay cable, Structures. 26 (2020) 214–223. https://doi.org/10.1016/j.istruc.2020.04.018.

[107] M. Wei, K. Lin, H. Liu, Experimental investigation on hysteretic behavior of a shear thickening fluid damper, Struct. Control Heal. Monit. 26 (2019) e2389. https://doi.org/10.1002/STC.2389.

[108] S. Gürgen, M.A. Sofuoğlu, Smart polymer integrated cork composites for enhanced vibration damping properties, Compos. Struct. 258 (2021).

https://doi.org/10.1016/j.compstruct.2020.113200.

[109] J. Lim, S.W. Kim, Enhanced damping characteristics of carbon fiber reinforced polymer–based shear thickening fluid hybrid composite structures, J. Intell. Mater. Syst. Struct. 31 (2020) 2291–2303. https://doi.org/10.1177/1045389X19898769.

[110] S. Gürgen, M.A. Sofuoğlu, Experimental investigation on vibration characteristics of shear thickening fluid filled CFRP tubes, Compos. Struct. 226 (2019) 111236. https://doi.org/10.1016/J.COMPSTRUCT.2019.111236.

[111] M.F. Ashby, The CES EduPack Resource Booklet 2. Material and Process Selection Charts, Granta Des. 2 (2009).